Investigating the Mechanical Behavior and Deformation Mechanisms of Ultrafine-

grained Metal Films Using Ex-situ and In-situ TEM Techniques

by

Ehsan Izadi

A Dissertation Presented in Partial Fulfillment
of the Requirements for the Degree
Doctor of Philosophy

Approved June 2017 by the
Graduate Supervisory Committee:

Jagannathan Rajagopalan, Chair
Pedro Peralta
Nikhilesh Chawla
Kiran Solanki
Jay Oswald

ARIZONA STATE UNIVERSITY

August 2017

ABSTRACT

Nanocrystalline (NC) and Ultrafine-grained (UFG) metal films exhibit a wide range of enhanced mechanical properties compared to their coarse-grained counterparts. These properties, such as very high strength, primarily arise from the change in the underlying deformation mechanisms. Experimental and simulation studies have shown that because of the small grain size, conventional dislocation plasticity is curtailed in these materials and grain boundary mediated mechanisms become more important. Although the deformation behavior and the underlying mechanisms in these materials have been investigated in depth, relatively little attention has been focused on the inhomogeneous nature of their microstructure (particularly originating from the texture of the film) and its influence on their macroscopic response. Furthermore, the rate dependency of mechanical response in NC/UFG metal films with different textures has not been systematically investigated. The objectives of this dissertation are two-fold.

The first objective is to carry out a systematic investigation of the mechanical behavior of NC/UFG thin films with different textures under different loading rates. This includes a novel approach to study the effect of texture-induced plastic anisotropy on mechanical behavior of the films. Efforts are made to correlate the behavior of UFG metal films and the underlying deformation mechanisms. The second objective is to understand the deformation mechanisms of UFG aluminum films using in-situ transmission electron microscopy (TEM) experiments with Automated Crystal Orientation Mapping. This technique enables us to investigate grain rotations in UFG Al films and to monitor the microstructural changes in these films during deformation, thereby revealing detailed information about the deformation mechanisms prevalent in UFG metal films.

ACKNOWLEDGMENTS

In the word of the great Galileo Galilei, "You cannot teach a man anything; you can only help him find it within himself". I was so blessed to have such mentorship in my life from all the people who have empowered me to reach this stage in my career. First and foremost, I would like to acknowledge the sacrifice that my family members have had to make over the years to ensure that I succeed in all my endeavors. Words cannot express how grateful I am for their support and prayers that has been what sustained me thus far.

I would like to extend my sincere gratitude to my advisor, Dr. Jagannathan Rajagopalan, who undoubtfully has been the most influential person in my graduate career for encouraging my research and for allowing me to grow as a research scientist. I would also like to thank my committee members, professor Dr. Pedro Peralta, Dr. Nikhilesh Chawla, Dr. Kiran Solanki and Dr. Jay Oswald for serving as my committee members even at hardship. I also want to thank you for letting my defense be an enjoyable moment, and for your brilliant comments and suggestions, thanks to you.

Lastly, I would like to thank all my friends who have made this journey pleasant and enriched my life through their company and support.

TABLE OF CONTENTS

iii

LIST OF TABLES

LIST OF FIGURES

CHAPTER 1

INTRODUCTION

1.1 Background

Nanocrystalline (NC) and ultrafine-grained (UFG) metals and alloys have been the subject of extensive research in recent years because of their unique properties. They are structurally characterized by a large volume fraction of grain boundaries, which significantly alter their physical, mechanical, and chemical properties in comparison with their conventional coarse-grained (CG) counterparts with the average grain dimension of a micrometer or larger. Several studies have focused on the microstructural evolution and mechanical behavior of these materials. The following sections contain a review of the research most pertinent to this dissertation.

1.1.1 Nanocrystalline and Ultrafine-grained Materials

Nanocrystalline and Ultrafine-grained metals and alloys have a mean grain size less than 100 nm and between 100 nm and 1000 nm, respectively. These class of materials exhibits a wide range of enhanced mechanical properties including high yield strength and wear resistance (Kumar, Van Swygenhoven, and Suresh 2003), which links to the high volume fraction of grain boundaries (Meyers, Mishra, and Benson 2006) in these materials (Figure 1) leading to significant grain boundary strengthening known as Hall-Petch effect (Hall 1951; Petch 1953).

1

NC/UFG materials can be synthesized by top-down (like cryomilling and compaction or severe plastic deformation) or bottom-up (like physical vapor deposition and electrodeposition) processes, which can be used to synthesize bulk (Valiev et al. 2006; Koch 2003) or nanoscale NC/UFG materials (Chen et al. 2009; Kumar et al. 2003), respectively.

The grain boundaries in these materials act as sources and sinks for dislocations and mediate deformation mechanisms like grain boundary sliding. Therefore, the character of these boundaries has been the subject of in-depth research. The grain boundaries in NC/UFG metals were previously considered to be fairly thick amorphous regions (Zhu et al. 1987). However, more recent experiments using high resolution electron microscopy (Kumar et al. 2003) as well as molecular dynamics simulations (H. Van Swygenhoven, Farkas, and Caro 2000) have revealed that the crystalline order is only distorted over a distance of few atomic planes (typically less than 1 nm).
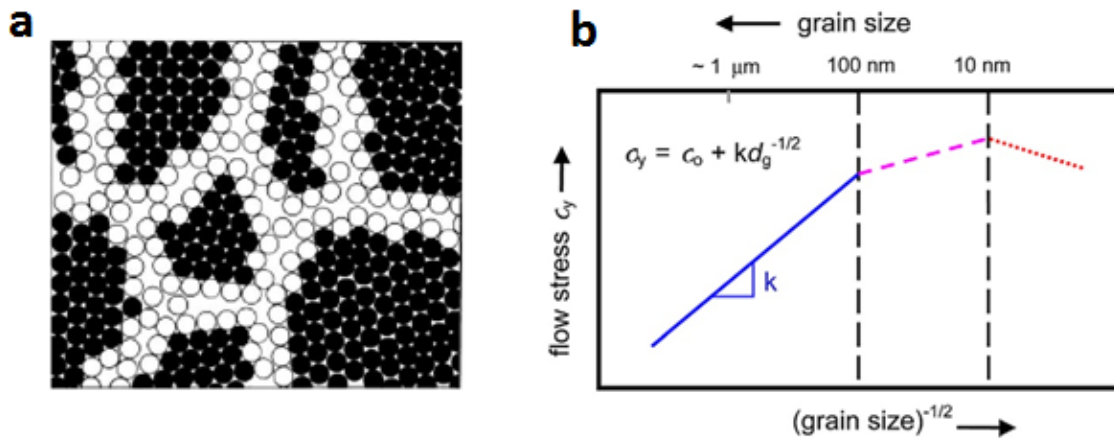
Figure 1: a) Model representing the structure of NC materials. Large fraction of atoms in grain boundaries (white circles) can be seen in NC materials. b) Increase in yield strength with decreasing grain size in NC materials (Kumar et al., 2003).

2

NC/UFG metals have been shown to exhibit substantially higher hardness and yield strength than the coarse grained materials (Sanders, Eastman, and Weertman 1997). However, these materials exhibit low ductility as they show lack of strain hardening through dislocation pileups at grain boundaries. Additionally, these materials show a dearth of intrinsic dislocations, with the majority of dislocations being nucleated and absorbed at grain boundaries during straining (Kumar, Van Swygenhoven, and Suresh 2003). It has also been shown that a break-down of the Hall-Petch effect occurs below a grain sizes of 10 nm where these materials become relatively weaker where phenomena like grain boundary sliding and coble creep start to dominate (Masumura, Hazzledine, and Pande 1998).

1.1.2 Mechanical Behavior of Fine-grained Thin Metal Films

There has been a considerable research carried out on the processing and characterization of UFG and NC metal films revealing that grain refinement is a powerful tool to enhance the mechanical response of the metal films (Kumar, Van Swygenhoven, and Suresh 2003; Meyers, Mishra, and Benson 2006). In addition to a number of appealing mechanical properties like high strength (Meyers, Mishra, and Benson 2006), UFG/NC metals also exhibit certain unusual characteristics as compared to their CG counterparts, like high strain rate sensitivity, plastic strain recovery and early Bauschinger effect (BE), which have been attributed to changes in the underlying deformation mechanisms (Rajagopalan, Rentenberger, Karnthaler, et al. 2010; Schwaiger et al. 2003; Jiang et al. 2006; Wang, Hamza, and Ma 2006; Wang and Ma 2004a; Jonnalagadda et al. 2010; Kim and Estrin 2005). Strain rate sensitivity (SRS) studies of thin metal films have typically

3

focused on mechanical behavior at rates between 10^{-6}/s and 10^{-3}/s (Schwaiger et al. 2003; Wang, Hamza, and Ma 2005; Emery and Povirk 2003a, 2003b), but more recently a wider range of strain rates (Chasiotis et al. 2007; Jiang et al. 2006; Jonnalagadda et al. 2010; Karanjgaokar et al. 2012) have been explored. SRS studies of UFG/NC metals have been mainly directed towards elucidating the effect of mean grain size on their rate dependent mechanical response. These studies have shown that across a wide range of metals SRS increases and activation volume decreases (Schwaiger et al. 2003; Jiang et al. 2006; Wang, Hamza, and Ma 2005; Kim and Estrin 2005) as the grain size becomes finer.

But in addition to the mean grain size, texture is also known to significantly influence the deformation behavior of UFG/NC metal films. Torre et al. have shown that differences in texture lead to variation in the yield stress and ultimate tensile stress of NC Ni foils (Dalla Torre, Van Swygenhoven, and Victoria 2002). Similarly, experiments on nanoscale Al films with similar mean grain size and thickness but different textures have revealed significant differences in flow stress and Bauschinger effect (Rajagopalan, Rentenberger, Karnthaler, et al. 2010; Rajagopalan and Saif 2011). However, the effect of texture on the SRS of metallic films has not been systematically investigated so far.

Plastic anisotropy, which can be induced in polycrystalline UFG/NC films as a result of crystallographic texture, can also affect the hardening behavior and stress distribution in the grains and influence the mechanical behavior of the thin metal films e.g. the extent of inelastic strain recovery. While some studies have considered the effect of Schmid factor variation (Borovikov et al. 2015; Li et al. 2012; Haouaoui, Karaman, and Maier 2006; Li, Lee, and Anderson 2010; Lin Li 2009) on the stress-strain response of both CG and UFG/NC materials, the effect of plastic anisotropy on the deformation of these

4

metal films has received relatively little attention and a systematic study of these effects on UFG metal films has been lacking.

1.1.3 In-situ TEM Investigation of Deformation Behavior of Metal Thin Films

It is well known that the changes in the macroscopic behavior of NC/UFG metals result from the changes in the underlying deformation mechanisms. Therefore, various in-situ experimental techniques have been employed to obtain a detailed understanding of the deformation mechanisms in NC/UFG metal films.

Among these techniques, in-situ synchrotron X-ray diffraction has been used to track the evolution of micro strain and changes in grain size and texture during deformation (Faurie et al. 2006; Helena Van Swygenhoven and Van Petegem 2013). However, it is not possible to directly resolve the microstructure of UFG/NC metals with this technique (Kobler et al. 2013). In-situ bright-field/dark-field transmission electron microscopy (TEM) has provided considerable insight into generation and motion of dislocations and deformation induced grain growth (Rajagopalan, Rentenberger, Karnthaler, et al. 2010; Jin et al. 2004) but these techniques do not yield meaningful statistics about microstructural evolution. In-situ scanning electron microscope (SEM) experiments with automated analysis of electron backscattered diffraction (EBSD) can also be used to analyze the texture and crystallography of grain boundaries (Dingley 2004; Buchheit et al. 2015; Zaefferer 2011). The limited spatial resolution in orientation imaging using SEM-EBSD, however, makes it difficult to investigate microstructural changes in UFG/NC materials (A. d. Darbal et al. 2013; A. D. Darbal et al. 2012).

Alternatively, automated crystal orientation mapping in TEM (ACOM-TEM) using precession electron diffraction, a recently developed technique, can be used to perform crystallographic analyses on UFG/NC metals during in-situ straining (Kobler et al. 2013; Zaefferer 2011; Idrissi et al. 2014; E. Rauch et al. 2010).

In the ACOM-TEM technique, which provides a spatial resolution better than 3 nm, a precessing nanoprobe electron beam is scanned over the specimen to collect spot diffraction patterns with reduced dynamical effects and improved pattern quality. The diffraction patterns are then automatically indexed using a template matching process, following which the orientation maps of the sample are extracted (Figure 2) (A. D. Darbal et al. 2012). ACOM-TEM enables direct acquisition of orientation/phase map over micrometer sized areas while enhancing the ability to identify grains, microtexture and twin and other coincidence site lattice boundaries (A. D. Darbal et al. 2012). This technique is especially helpful in obtaining a comprehensive picture of microstructural evolution in UFG/NC metals, which are known to have an unstable microstructure (Kobler et al. 2013). Precession electron diffraction has also been used to estimate dislocation densities and driving force for twin formation using Nye tensor (Leff, Weinberger, and Taheri 2015; Leff and Taheri 2016). Despite all the tremendous advances in the experimental characterization techniques, some major aspects of the deformation behavior in fine-grained metals have still remained unclear.
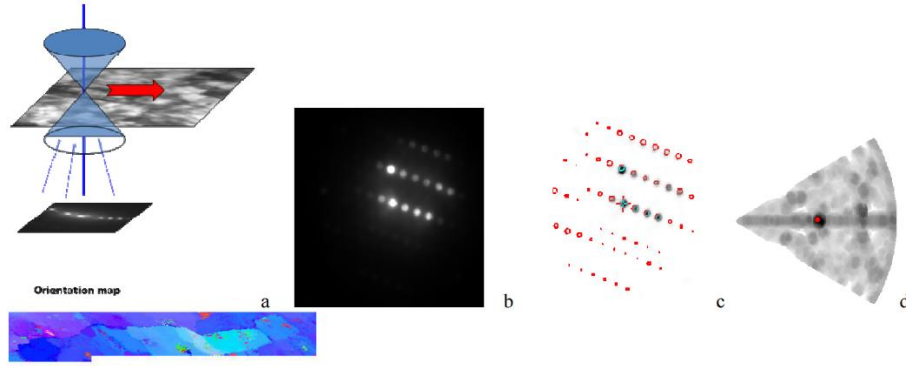
Figure 2: Schematics of Precession Electron Diffration (PED) assisted Orientational and Phase Mapping: (a) beam scanning with DigiSTAR over a user-defined sample area combined with precession (b) experimental spot PED pattern serial recording in computer memory (c) superposition of individual ED template (red dot pattern) which best matches experimental PED pattern (grey dot pattern), and (d) orientation directional map with grey intensity plot of matching index for the experimental spot PED pattern.(Portillo et al. 2010)

1.2 Motivation and Organization of The Dissertation

As outlined in the previous section, extensive studies of the mechanical properties as well as the deformation mechanisms of nanocrystalline and ultrafine-grained metals have been undertaken in recent years. Despite a broad ranging research efforts focusing on effect of texture and loading rate on mechanical behavior of fine-grained metal films, relatively little attention has been focused on how film texture influences the SRS of macroscopic response of these materials. A detailed understanding of this aspect is important because these metallic materials of different textures may be subjected to a wide range of loading rates as being employed in numerous applications including interconnects in semiconductor devices and electrode components in micro-electro-mechanical systems (MEMS) (Chasiotis et al. 2007; Ledermann et al. 2003; Polcawich et al. 2007) etc. Therefore, this dissertation uses a combination of ex-situ experiments and in-situ TEM techniques to study the effect of film texture on strain rate sensitivity of freestanding

7

ultrafine-grained Al films. The organization of this thesis follows naturally from the objectives stated above.

In chapter 2, we outline the fabrication process for the microelectromechanical systems (MEMS) based micro tensile device and describe the overall testing set up used for the experiments.

In chapter 3, we show that ultrafine-grained Al films with different textures show significantly different strain rate sensitivity of mechanical behavior during loading. Furthermore, we show evidences of time-dependent, out of plane grain orientation changes during deformation of these films.

In the next chapter, we propose a new in-situ TEM experimental technique (ACOM-TEM) to quantitatively investigate grain rotations in UFG non-textured Al films.

In chapter 5, we show that the ultrafine grained Al films of different textures also exhibit a markedly different strain rate sensitivity of Bauschinger effect during unloading.

In chapter 6, we investigate the effect of plastic anisotropy on mechanical response of ultrafine-grained bicrystalline Al film through loading and unloading of the film along different loading direction. Furthermore, we show how loading films of identical texture along different loading directions can lead to very dissimilar deformation heterogeneity and a resultant difference in mechanical behavior of the films.

In chapter 7, we report on quantitative investigations of grain rotation in ultrafine-grained bicrystalline Al films, loaded along the direction with higher level of deformation heterogeneity, by carrying out in-situ TEM load-unload experiments with ACOM-TEM technique (introduced in chapter 4). Finally, in chapter 8 we summarize the findings from this study and identify pertinent issues to investigate in the future.

CHAPTER 2

EXPERIMENTAL TOOLS AND METHODS

The uniaxial tensile testing experiments on freestanding metal films were performed in this study using a MEMS based micro tensile device. It is made of single crystal silicon. Unlike traditional material testing set ups, where the test samples are fabricated separately, here the test sample and the test apparatus are co-fabricated. This eliminates the problems associated with gripping and alignment of the thin film samples and ensures uniform, uniaxial tensile deformation. This chapter outlines the operation of this MEMS device and explains its fabrication process.

Before fabrication process begins, the silicon wafer is cleaned thoroughly to get rid of any particles on the surface. Based on the requirement, sometimes the native silicon dioxide layer is removed using wet hydrofluoric acid etching before film deposition. In the next step, aluminum film is sputter deposited to the required thickness on top of the wafer.

Subsequently, the following process flow is adopted for the fabrication of the MEMS device upon sputter deposition of thin film on Si wafer. The schematic of the process flow is shown in Figure 3.

1. Spin coating of photoresist on top and bottom surfaces of wafer.

2. Alignment of the front-side of the wafer with front-side photomask and exposure of wafer to UV light through the mask.

3. Development of alignment marks on the front-side of the wafer.

4. Alignment of back-side mask with the developed alignment marks on the front-side of the wafer.

9

5. Development of all MEMS device features on the top and back-side of the wafer.

6. Reactive ion etching of metal from exposed regions on the front-side of the wafer.

7. Through-thickness, anisotropic, deep reactive ion etching of the wafer from the back-side of the wafer to release the samples from the substrates.

8. Removal of the remnant photoresist from the MEMS devices using an oxygen plasma asher.
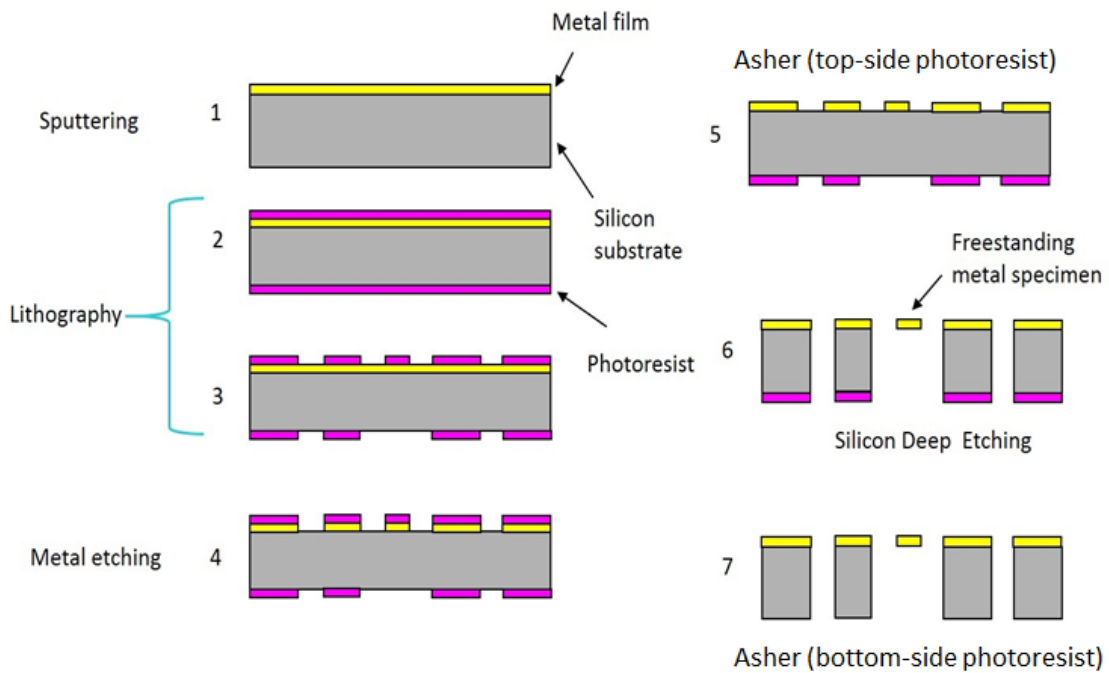
Figure 3: Schematic of the process used for co-fabricating the micro tensile device and the freestanding metal sample.

2.1 Magnetron Sputtering System

A magnetron sputtering system (Orion 5 system manufactured by AJA International) was employed to synthesize all the thin films studied in this dissertation (Figure 4). Sputtering is a form of physical vapor deposition in which inert gas ions are

10

used to knock off atoms from the material target onto a substrate. This makes it an excellent technique to deposit uniform thin films with fine control over the film thickness and composition. The Orion 5 sputtering system contains three confocal magnetron sputtering guns, which can be operated individually or simultaneously. Simultaneous deposition from multiple targets makes the growth of alloys and metallic glass films possible. Each gun is equipped with a pneumatically operated shutter that can be used to stop deposition from that specific gun. The tool possesses two DC and one RF power sources. The DC power sources are used to deposit metals while the RF source can be used to deposit semiconductors and insulators and also to clean substrates by back sputtering using the argon plasma when employing a reverse RF bias. Ultra-high purity argon plasma is used to sputter off atoms from 2" diameter metallic or dielectric targets. A reactive sputtering technique can also be employed to grow dielectric thin films (SiN_x) by introducing a gas like nitrogen in the chamber along with the plasma forming argon. The main sputtering chamber is connected to a load lock through a gate valve. The tool is equipped with load lock that facilitates faster sample pump down and transfer times and two turbo molecular pumps (one for the main chamber and the other for the load-lock) backed up by mechanical pumps to achieve a decent vacuum with base pressures better than 5×10^{-8} Torr. To further improve this, chamber conditioning treatment steps that involve deposition of gettering materials like titanium and aluminum on the chamber walls followed by a bake-out of the chamber using heating strips is regularly employed. The substrate holder is made of Inconel and can be heated up to 800°C by ceramic heating lamps. This enables the annealing of thin films during or after deposition.

Figure 4: Left: Orion 5 Sputter Deposition Tool used to synthesize metallic and amorphous thin films. Right: Magnetron sputtering guns having copper targets. Pictures courtesy AJA International.

2.2 Microfabrication Tools

Multiple microfabrication tools were employed to fabricate the MEMS tensile testing device and to conduct uniaxial tensile experiment on freestanding thin film samples. Photolithography and reactive ion etching techniques were extensively used to fabricate the MEMS device. The major tools are described below.

2.2.1 Photoresist Spinner

Photoresist spinners were used to spin coat AZ 4620 and AZ 3312 photoresists on the front-side and back-side of silicon wafer, respectively. After the photoresist was applied on the wafer using a pipette, the wafer was spun at speeds between 2000-3500 RPM to prepare a uniformly distributed coat of photoresist on its surface. After spin coating, the wafers are subjected to a soft bake process at 100^0C to prepare it for the alignment step. Depending on the spinning parameters, baking condition and the kind of photoresist used, the thickness of the resist layer obtained was between 1-6 µm.

12

2.2.2 EVG 620 Aligner

     After spin coating the wafers with photoresist, the EVG 620 aligner was used to align the chrome mask containing the designated pattern of MEMS device (Figure 5) and the wafer. After aligning the wafer to specific alignment marks on the mask, the tool exposed the wafer to UV light. The exposed photoresist was subsequently developed using AZ 300MIF to reveal the MEMS device patterns on the wafer. The front-side and back-side patterns were mirror images except that the sample area in the back-side pattern was open, as shown in Figure 5. Upon photoresist development, cured photoresist regions acts as the etch mask while the developed regions of the photoresist are etched away in the subsequent processes.
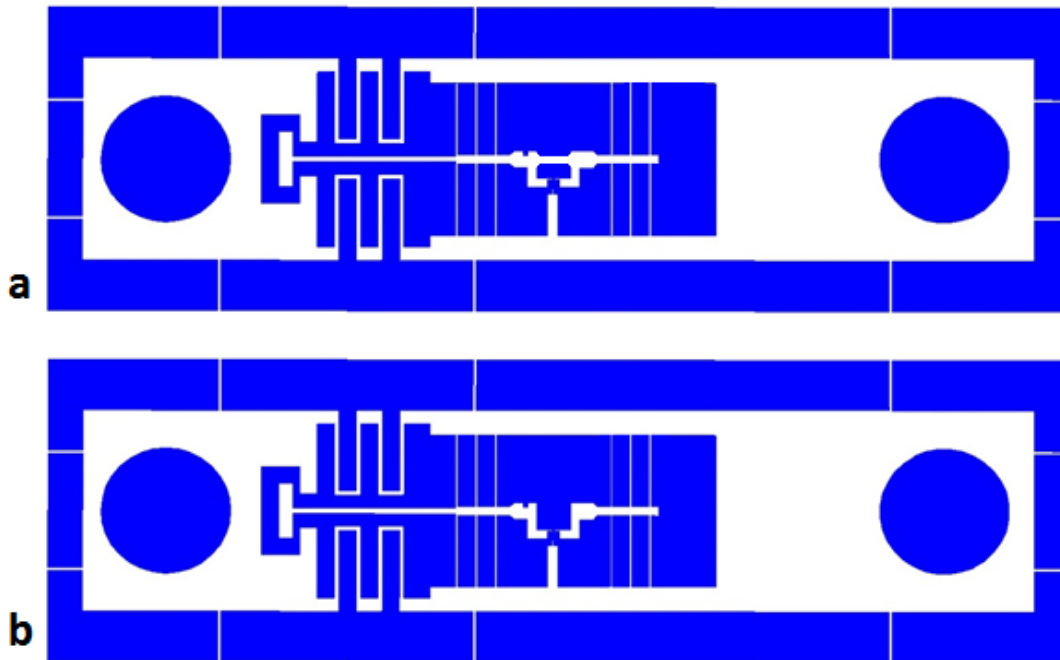
Figure 5: Design of mask used in the EVG 620 aligner to transfer MEMS device pattern onto the wafers. White represents the opaque regions while blue represent transparent regions. a) Front-side pattern. b) Back-side pattern.

2.2.3 Oxford Plasmalab 80+ Reactive Ion Etcher (RIE)

Upon transferring the pattern of the MEMS device onto the wafer, the metallic thin film layer was etched away in specific locations using the RIE (Figure 6). The tool uses plasma of Cl_2 and BCl_3 gases to etch away the metal layer from the font-side of the wafer using a combination of physical and chemical etching. The wafer is placed on the electrode of the tool to accelerate the plasma ions towards the wafer. This causes anisotropic etching of the metal film with the etch rate normal to the wafer surface being greater than the etch rate in the plane of the wafer.
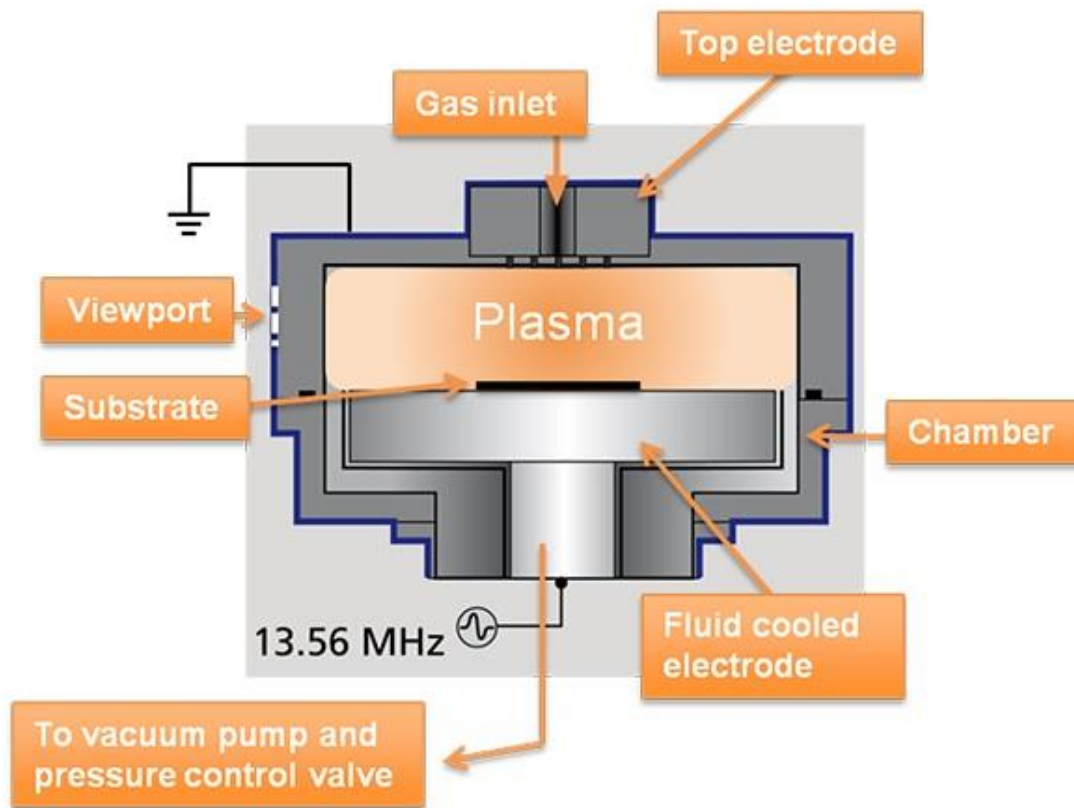
Figure 6: Layout of the RIE chamber. The BCl_3 and Cl_2 gases are used to etch metal films anisotropically. Image courtesy Oxford Instruments.

2.2.4 STS Advanced Silicon Etcher

Fabrication of the MEMS device required a through-etch process from the back-side of the wafer side. Large depths needed to be etched while simultaneously ensuring that the walls of MEMS device beams remained vertical. This was achieved by using an inductively couple plasma etcher employing a two-step "Bosch" process to achieve extremely anisotropic etch features (Figure 7) (Abdolvand and Ayazi 2008).
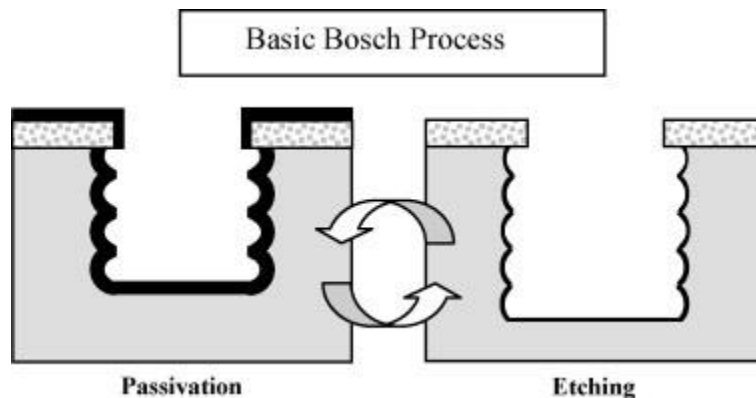
Figure 7: Schematic representation of the two step Bosch process (Abdolvand et. al, 2008).

The first step is the deposition of a thin passivation layer of C_4F_8, which serves the purpose of protecting the side walls of the MEMS device. Following this step, a SF_6 based plasma is used to etch away silicon in specific locations of the wafer (developed regions of the photoresist). In this step, the electrode on which the wafer is placed accelerates the SF_6 ions towards it. As a result, a physical sputtering of atoms of the wafer takes place and the passivation layer of C_4F_8, along with Si atoms are sputtered off very effectively in the plane of the wafer surface since the plasma ions are accelerated in a direction normal to the wafer surface. In contrast, the passivation layer on features that are normal to plane of the wafer do not get sputtered off by the plasma and are thus able to protect the vertical walls. Subsequently, chemical etching by the fluorine ions take place and the features in the plane

of the wafer that are not protected by the Teflon coating, get etched away more easily than the side walls, protected by the passivation layer. The tool continuously switches between the etching and passivation steps till the wafer is etched all the way through its thickness, thus, completely releasing the fabricated MEMS device out of the wafer. The fabrication of the MEMS devices was ultimately completed upon the subsequent step of remnant photoresist removal using an oxygen plasma asher.

2.3 MEMS Tensile Testing Stage

Two types of MEMS based tensile testing stages with slightly different designs is used to conduct uniaxial tensile tests on freestanding thin films. Design I is designated to conduct in-situ TEM, quasi-static tensile experiments (Figure 8) whereas design II is prepared to carry out ex-situ tensile experiments with different strain rates (Figure 9).

The straining is achieved by pulling the devices apart using pins that pass through the holes on each end. The pins are actuated by stages driven motors or a piezoelectric actuator. The freestanding thin film is connected to the MEMS devices by a number of silicon beams. On one end of the beam, connecting the film to the device is a "T-bone" with a specific gap, which ensures that the sample does not accidentally get strained before an experiment. As the MEMS device is stretched from one end, the U-beams get deformed leading to T-bone gap closure. Therefore, the sample gets engaged and starts getting strained.
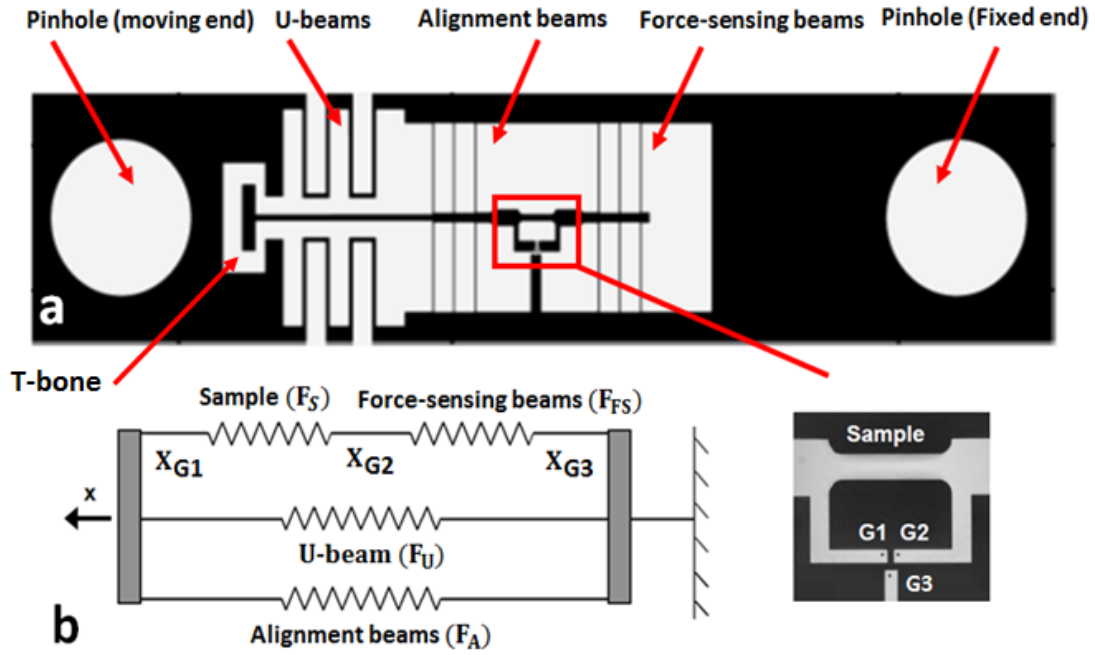
Figure 8: a) MEMS device for performing tensile experiments on freestanding metal film samples. The nominal strain on the sample is obtained by tracking the displacement of gauges G1 and G2. b) Equivalent mechanical model of the MEMS device. The U-beams and Alignment beams are in parallel with the sample and hence their displacement (x) is the same.
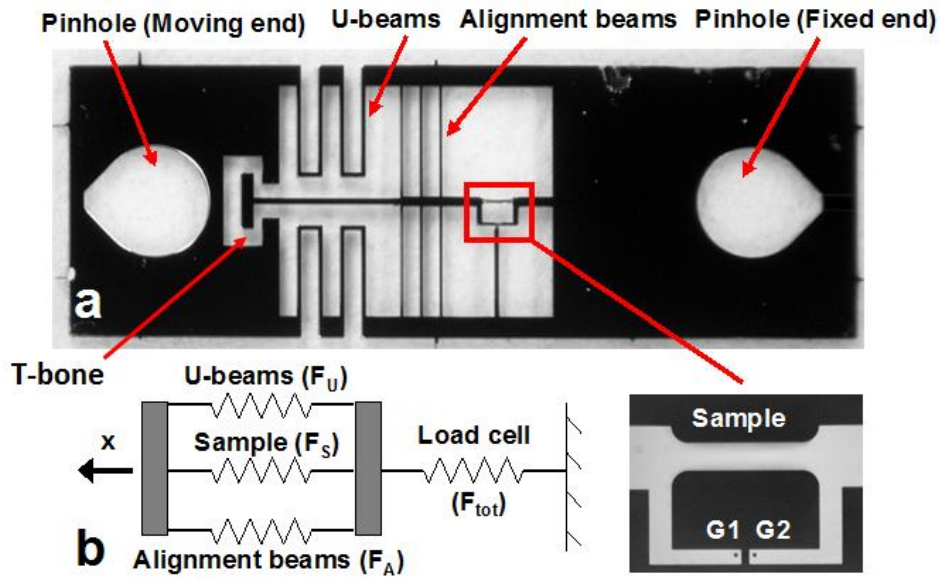
Figure 9: a) MEMS device for performing constant strain rate experiments on freestanding metal film samples. The nominal strain on the sample is obtained by tracking the displacement of gauges G1 and G2. b) Equivalent mechanical model of the MEMS device. The U-beams and Alignment beams are in parallel with the sample and hence their displacement (x) is the same. The load cell is arranged in series with the MEMS device.

17

The devices are equipped with a set of front beams, which eliminate any misalignment during the loading process in addition to protect the sample from damage from air pressure gradients during loading and unloading from vacuum chambers of TEM.

The devices have a number of features that give them the unique capability to measure macroscopic stress and strain acting on the thin films while carrying out ex-situ and in-situ TEM experiments. Three gauges are designed into the device of design I to measure the macroscopic stress and strain acting on the sample (Figure 8). A CMOS camera (Thor Labs) is used to acquire images of the gauges during the experiments. A custom MATLAB^{TM} program, which tracks prescribed features across a series of images using cross-correlation techniques, is used to measure the displacement of the gauges and thus the sample strain and stress.

The strain sensing gauges G1 and G2 are attached on opposite ends of the sample. Thus, the change in relative displacement between G1 and G2 gives a measure of the elongation on the sample. The back beams on this device are designed to measure the stress acting on the sample. The sample and the back beams can be viewed as springs in series (Figure 8b). As a result, the force acting on the back beams equals the force acting on the sample. The relative displacement between G2, connected to the back beams, and stationary gauge G3 is used to measure the deflection on the back beams. This deflection multiplied by the stiffness of the back beams, which is calibrated using a needle of standard stiffness, gives us the force acting on the sample. Due to the small footprint of the device, it can be used to carry out in-situ TEM experiments. This device was developed in Prof Taher Saif's group at UIUC (Han and Saif 2006; Haque and Saif 2002). Additionally, MEMS devices of design II are fabricated with a minor modification where the back beams

are removed leading to a constrain on one end of the sample to be connected directly to the fixed end of the MEMS device. This enables easier control over the rate of loading on the sample and leads to carry out more precise constant strain rate tensile experiments. However, this design lacks the possibility of obtaining the information of the force acting on the sample using the gauges. To address this issue, a load cell, arranged in series with the MEMS device, measures the total force (F_{tot}) on the device (Figure 9b). As evident from the equivalent mechanical model of the device, $F_{tot} = F_S + F_U + F_A$, where F_S is the force on the sample and F_U and F_A are the force on the U-beams and the Alignment beams, respectively. The combined stiffness (K) of the U-beams and Alignment beams is measured in a separate experiment after the sample fractures. K multiplied by the displacement (x) gives $F_U + F_A$, from which F_S and thus the stress on the sample is obtained.

2.4 Experimental Setup

The in-situ TEM straining experiments are carried out in JEOL ARM200F TEM. A Gatan single tilt straining holder is used to strain the MEMS devices of design I (Figure 10). Displacement pulses of about 100-150 nm are applied to the sample in each step followed by capturing images and diffraction patterns at areas of interest. However, the ex-situ constant strain rate experiments are carried out under an optical microscope (Thor Labs) where the MEMS devices of design II are mounted on a stage with two pins (Figure 11). The MEMS device is precisely stretched with predefined loading rates using a piezoelectric actuator (Physik Instrumente) located at one end of the experimental setup, while a miniature s-beam load cell (Futek) is located on the other end.
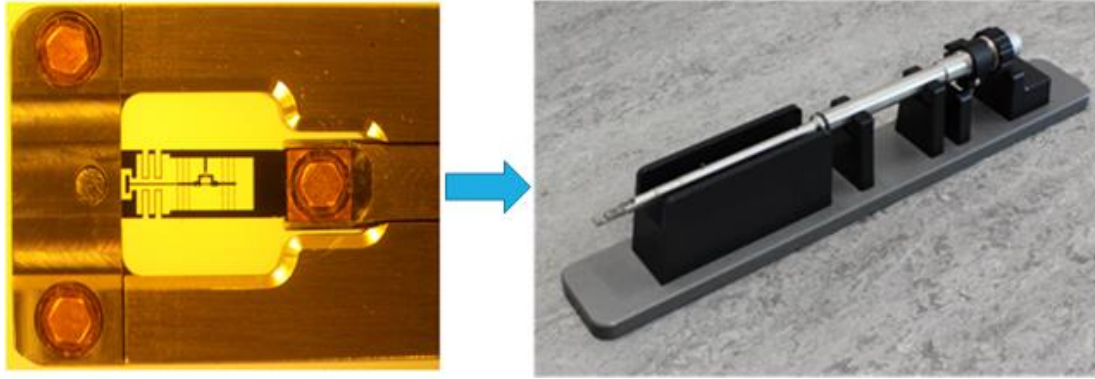
Figure 10: TEM single tilt straining holder. Pictures courtesy of Gatan Inc.
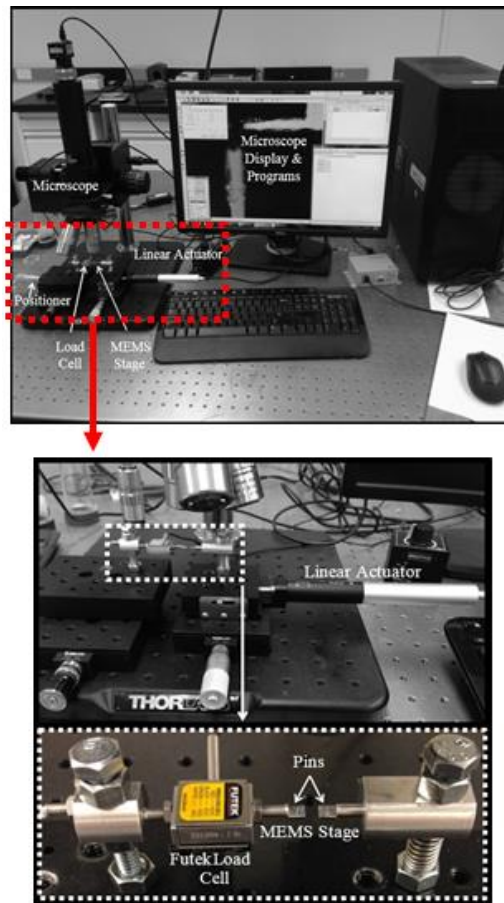
Figure 11: The experimental setup for ex-situ constant strain rate experiments.

CHAPTER 3

TEXTURE DEPENDENT STRAIN RATE SENSITIVITY OF ULTRAFINE-GRAINED ALUMINUM FILMS

3.1 Introduction

In this chapter, we investigated the stress-strain response of ultrafine-grained aluminum (Al) films with similar thickness and mean grain size but very different textures through monotonic loading experiments at strain rates ranging from $\sim 10^{-5}$ to 10^{-2} per second.

3.2 Materials and Experimental Procedure

A bicrystalline Al film (labeled as textured film) and a non-textured Al film were synthesized by carefully controlling the deposition conditions. To obtain the textured film, the native silicon dioxide layer on a Si (001) wafer was removed through hydrofluoric acid etching and the wafer was immediately transferred to the sputtering chamber to avoid regrowth of the oxide layer. Al was then deposited on the bare silicon wafer using DC magnetron sputtering, which resulted in heteroepitaxial growth with the following relationship: Al(110)//Si(001), Al[001]//Si[1$\bar{1}$0] and Al(110)//Si(001), Al[001]//Si[110] (Niwa and Kato 1991). Thus, this film consists of just two grain families with (110) out-of-plane texture which are rotated 90° in plane with respect to each other. The non-textured film was obtained using a similar process except that it was sputter deposited on Si (001) wafers with the native silicon dioxide layer intact. The oxide layer disrupts the epitaxial

growth of Al, leading to a film with random orientation of grains. Both the textured film and non-textured film was deposited to a thickness of ~240 nm at 5.5 nm/min. The chamber base pressure during deposition of the textured and non-textured film was 8×10^{-8} Torr and 3×10^{-7} Torr, respectively.

The microstructure of the films was examined through transmission electron microscopy (TEM) and x-ray diffraction (XRD). Based on plan-view TEM images the textured Al film had a mean grain size of 275 nm and the non-textured film had a mean grain size of 285 nm (Figure 12). The images also indicated a columnar grain structure with one grain traversing the thickness of the film. Dog-bone shaped freestanding samples were then co-fabricated with MEMS device of design II (Figure 9a) using microfabrication techniques to carry out constant strain rate experiments as all described in chapter 2. Following the same calculation methodology explained in the same section, the stress on the sample was measured using a micro load cell, which accordingly led to calculate the flow stress of the films.

In all the experiments, loading was along the [001] direction of the Al[001]//Si[110] grain family for the textured film and along an arbitrary direction for the non-textured film. To calculate the uncertainty in stress measurements, a range of loads were applied on the load cell and the fluctuations in force were recorded over time for each load. Based on the load cell fluctuations, the uncertainty in the calculated stress was less than 10 MPa for all the samples. Similarly, for a prescribed displacement, images of the gauges were recorded over a period of time and analyzed. Based on the analysis, the error in strain measurement was found to be less than 0.003%. There was also an ~10 nm variation in the thickness of both the textured and non-textured film across the wafer. Both the load cell fluctuations

and the variation in the film thickness were taken into account for calculating the error in the flow stress of the films.
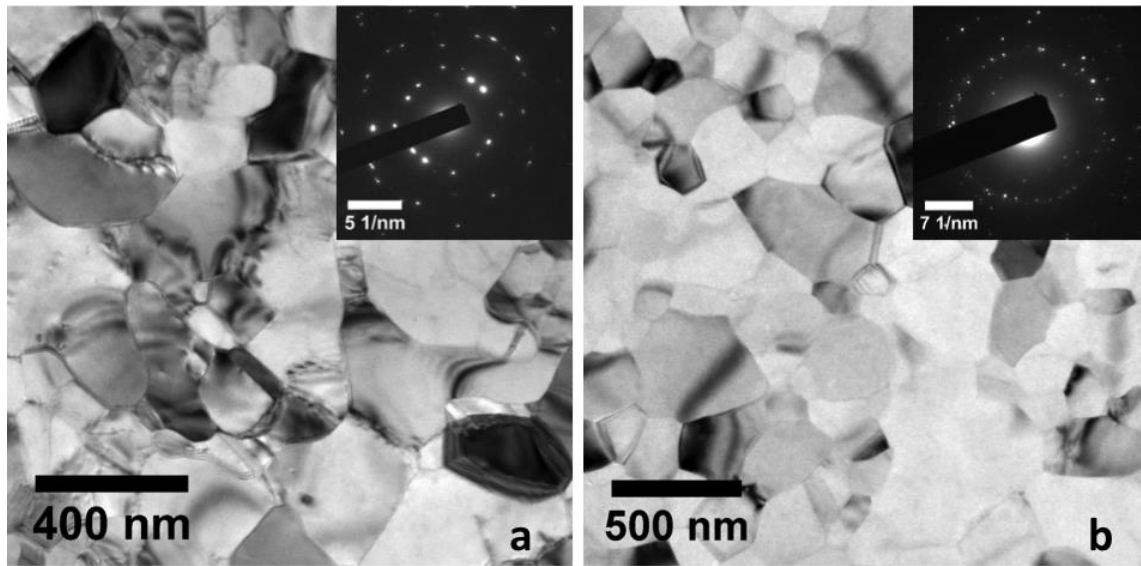
Figure 12: (a) Bright-field TEM image of the textured Al film with a mean grain size of 275 nm. Selected area diffraction (SAD) of the film showing an (110) out-of-plane texture with two in-plane variants rotated 900 with respect to each other (inset). (b) Bright-field TEM image of the non-textured Al film with a mean grain size of 285 nm. Selected area diffraction (SAD) of the film showing the lack of texture (inset).

The Al films were under compressive stress in the as-deposited state and hence the freestanding samples buckled when they were released from the Si substrate. Because the stress for buckling along the length is very low (0.1 MPa) (Rajagopalan and Saif 2011), the samples are almost macroscopically stress-free before loading. In addition, to eliminate possible variation in mechanical behavior that can arise from sample size effects, we ensured that all the samples from both the textured and non-textured film had identical dimensions (effective gauge length 375 μm, width 75 μm). Thus, by ensuring uniformity in the fabrication process, mean grain size, and sample dimensions, we were able to isolate the effect of texture on the strain-rate dependent behavior of the Al films.

3.3 Results and Discussion

Figure 13 shows the stress-strain response of the textured and non-textured film at different strain rates. The corresponding durations of the experiments varied from less than 2 seconds at the fastest rate to more than 2000 seconds at the slowest rate. As evident from Figure 13a, the stress-strain response of the textured film did not vary significantly with strain rate. At all rates, an initial linear response was followed by a gradual elastic-plastic transition (microplastic regime) that is typical of UFG and NC metals. To quantify the strain rate effect, we calculated the stress at 0.9% strain ($\sigma_{0.9\%}$) at different rates and used it as a measure of flow stress. $\sigma_{0.9\%}$ was chosen as a measure of flow stress because macroscopic plasticity had set in the samples before 0.9% strain and there was little subsequent strain hardening. Another consideration was that the samples failed around 1% strain at the highest strain rate. For the textured film flow stress increased from 302 MPa to 342 MPa (14% increase) as the strain rate increased from 6.9×10^{-6}/s to 5.3×10^{-3}/s.

In contrast, the non-textured film (Figure 13b) showed considerable difference in stress-strain response over a similar range of strain rates. Flow stress ($\sigma_{0.9\%}$) increased from 243 MPa to 473 MPa as the strain rate was increased from 6.8×10^{-6}/s to 6.7×10^{-3}/s. In addition, during the elastic-plastic transition the stress-strain slope was significantly higher at the higher strain rates. However, once macroscopic plasticity set in little hardening was observed, irrespective of the strain rate. Thus, while the flow stress was sensitive to the strain rate, the rate of strain hardening was not. To quantitatively compare the stress-strain response of the textured and non-textured film, we calculated the strain rate sensitivity (SRS) exponent ($m = d\log(\sigma)/d\log(\dot{\varepsilon})$) for both the films (Figure 13c). m for the non-

textured film was 0.103, more than six times higher compared to the textured film with m= 0.017.
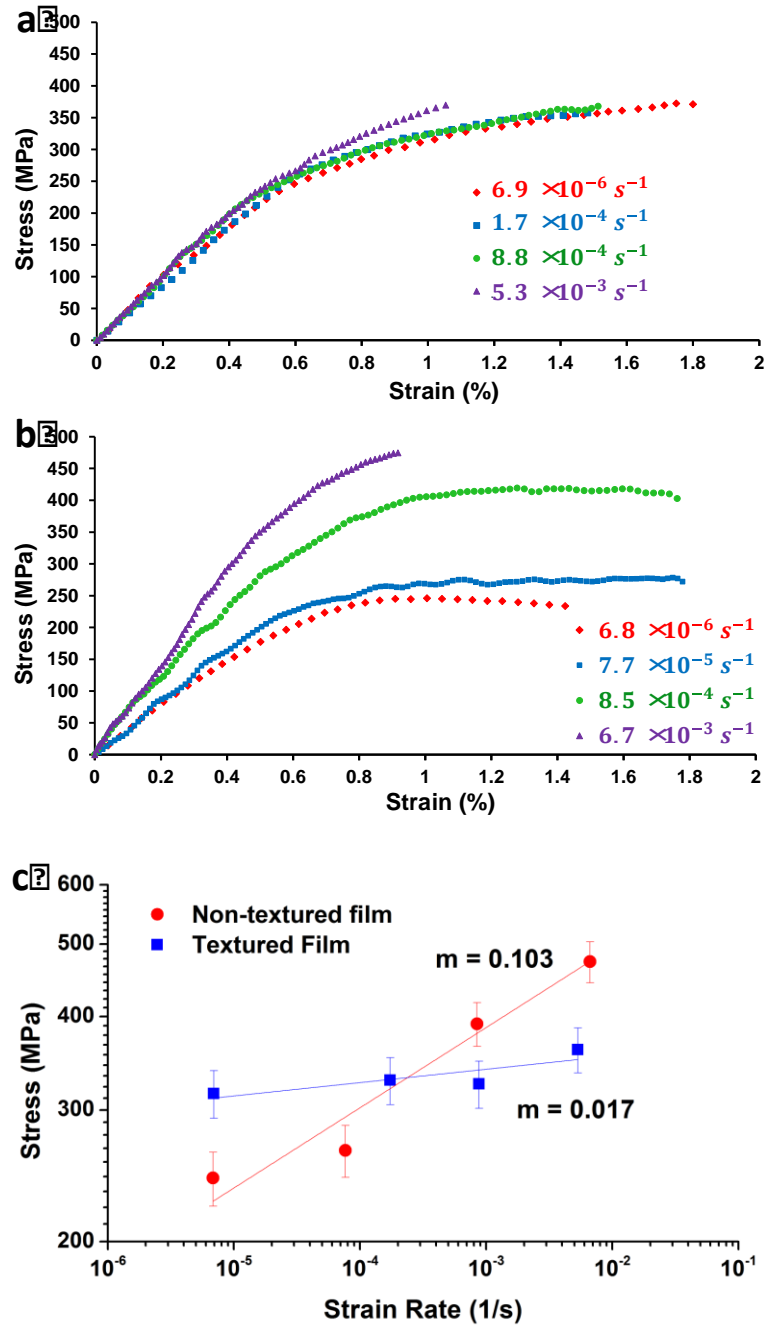
Figure 13: (a) Stress-strain response of the textured film at different strain rates. (b) Stress-strain response of the non-textured film at different strain rates. (c) Log-log plot of flow stress versus strain rate for the textured and non-textured film. The error bars indicate the bounds of uncertainty in flow stress arising from both film thickness variation and fluctuations in the load cell measurements.

Previous studies show that NC and UFG face-centered cubic (FCC) metals exhibit strain rate sensitivities that are an order of magnitude larger than coarse-grained FCC metals, which usually have m of 0.001 to 0.005 (Wang and Ma 2004b; Mohanty et al. 2014; Maier et al. 2011). UFG Al, for example, has been shown to exhibit m values ranging from 0.02 to 0.2 (Mohebbi et al. 2014; May, Höppel, and Göken 2005; Böhner et al. 2011; Read et al. 2001; Wheeler et al. 2013) at strain rates comparable to those used in this study. Similarly in NC Al films that undergo discontinuous grain growth, m values ranging from 0.035 to 0.14 have been reported (Gianola, Warner, et al. 2006).
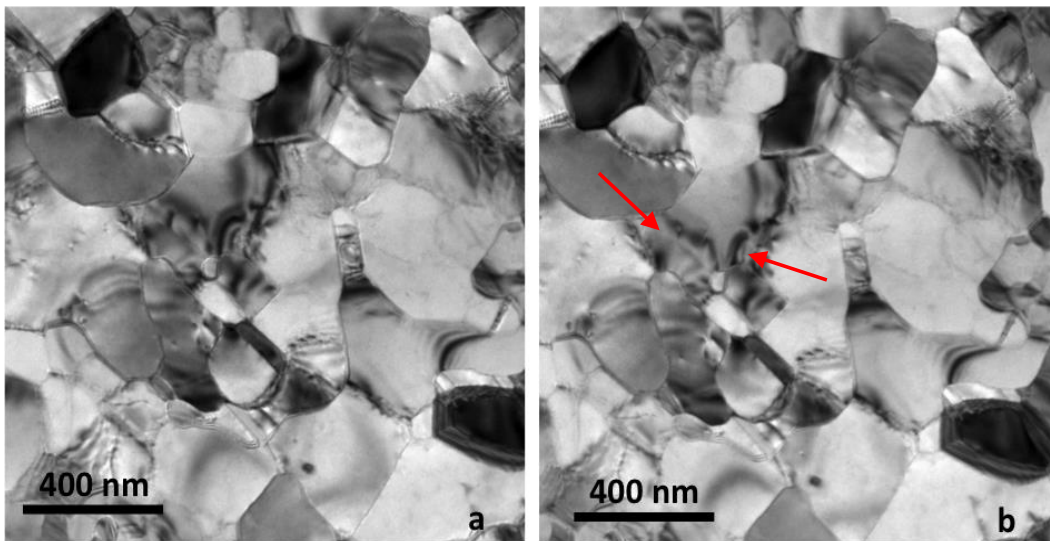
Figure 14: Bright field TEM images of the 240 nm thick textured film before (a) and after (b) the application of a straining pulse. There was little change in grain contrast and no motion of bend contours. The arrows point to locations of dislocation activity.
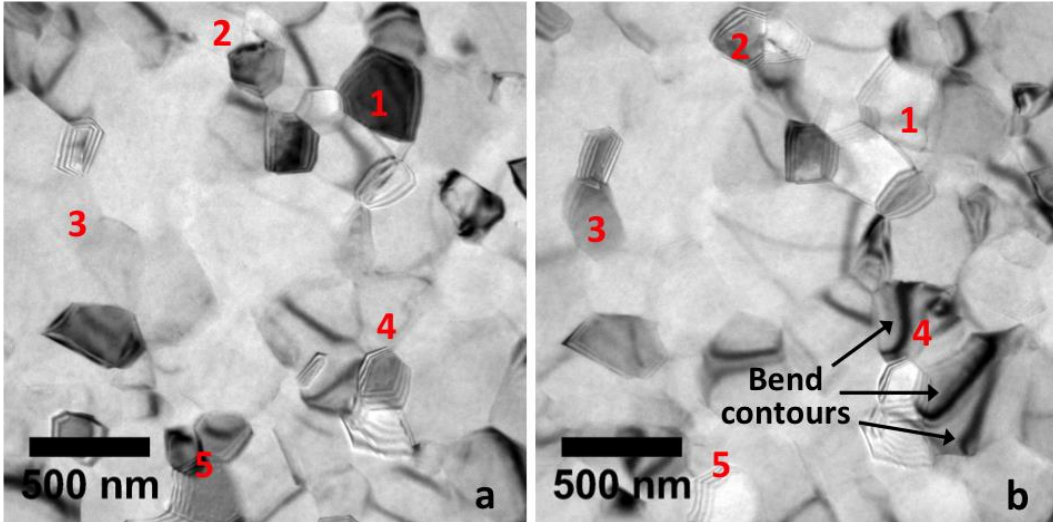
Figure 15: (a) Bright field TEM image of a non-textured film at 1.19% strain. (b) Image of the same area at 1.3% strain. The numbers in red identify a sampling of grains that showed a drastic change in contrast (indicative of orientation change). Arrows point to new bend contours that resulted from the strain increment.

Typically, m values progressively increase as the grain size is reduced from the microcrystalline to the NC regime (Schwaiger et al. 2003; Dalla Torre et al. 2005; Wang, Hamza, and Ma 2006; Dao et al. 2007). This grain size dependence has been attributed to the changes in deformation mechanisms that accommodate plasticity (Dao et al. 2007). In coarse-grained metals, the rate-controlling process is the cutting of forest dislocations, which results in a low SRS. In contrast, for NC and UFG metals a primary rate-limiting process is the interaction between dislocations and grain boundaries, which serve as obstacles to dislocation motion (H. Van Swygenhoven, Derlet, and Frøseth 2006). Hence, as the density of grain boundaries increases with decreasing grain size, the rate-dependence of deformation behavior becomes more pronounced.

Our results show that UFG metal films with different textures can have considerable differences in SRS, even when their mean grain size and thickness are nearly identical. This suggests that texture plays an equally important role as grain size in determining the rate sensitivity and deformation mechanisms of UFG metal films.

To obtain insight into the deformation mechanisms that are active in the textured and non-textured films, we performed quasi-static in-situ straining experiments on these films in a JEOL 2010F TEM. The experiments were performed under a low intensity, 200 kV electron beam to minimize beam-induced artifacts during in-situ TEM deformation (Sarkar, Rentenberger, and Rajagopalan 2015). When the textured film began to deform plastically there was notable dislocation activity, and a few grains showed changes in contrast (indicative of out-of-plane grain rotation) when the strain was increased. However, there were no time-dependent changes in grain contrast or motion of bend contours when the strain was held constant (Figure 14). It is worth noting that previous in-situ TEM studies of such textured Al films have shown similar results (Rajagopalan, Rentenberger, Peter Karnthaler, et al. 2010; Sarkar, Rentenberger, and Rajagopalan 2015).

The behavior of the non-textured film, in contrast, was qualitatively different, with a larger fraction of grains showing instantaneous changes in contrast when strain was increased (Figure 15). More importantly, the grains also underwent gradual changes in contrast over time, often accompanied by motion of bend contours, even when the strain was held constant. Since the grain orientations were continuously changing and most grains were away from the Bragg condition it was difficult to observe dislocation activities in the non-textured film. Nevertheless, the time-dependent grain orientation changes suggest that diffusive relaxation processes could be active in addition to dislocation plasticity.

The strain rate experiments in conjunction with the qualitative in-situ TEM experiments point to the following picture of deformation in the textured and non-textured film. In the textured (bicrystalline) film, the initial deformation is relatively homogeneous because elastic modulus for the two sets of grains along their loading directions (<100> and <110>) is quite similar (63.7 GPa and 72.5 GPa, respectively). Thus, the elastic strain mismatch between the grains is small and since they have the same out-of-plane orientation little or no grain rotation is required to maintain strain compatibility.

After the initial elastic regime, the film undergoes microplastic deformation as relatively larger grains yield first and are followed by progressively smaller grains. However, both sets of grains have sufficient slip systems to accommodate the imposed deformation and all the active slip systems in both sets of grains have the same Schmid factor (s = 0.408). In effect, plastic anisotropy is nearly eliminated and hence the plastic strain mismatch between the grains is quite small. This again reduces the need for grain rotation to accommodate the deformation.

In contrast, deformation of the non-textured film is considerably more heterogeneous. Because the grains are randomly oriented, there is more variation in elastic modulus (63.7-76 GPa) and hence higher elastic strain mismatch between the grains. More importantly, the maximum Schmid factor (s) of the grains varies from 0.27 to 0.5. Therefore, plastic anisotropy (s_{max}/s_{min}) in the non-textured film is significantly more pronounced compared to the textured film. As a result, the plastic strain mismatch between adjoining grains is substantially higher, and the grains need to bend or rotate with respect to each other to maintain strain compatibility.

If the applied strain rate is low, the grains can relax the stress arising from elastic/plastic incompatibility through diffusive processes. But at higher strain rates such relaxation is not possible and thus the macroscopic stress-strain response becomes highly rate sensitive. Note that even though the experiments are performed at room temperature, the homologous temperature ($T/T_{Melting}$) for Al exceeds 0.3. And since the thin film samples have a large surface to volume ratio, surface diffusion, which has lower activation energy compared to bulk diffusion, can be significant and lead to stress relaxation. In this context, it is also worth noting that at lower strain rates the non-textured film exhibits lower flow stress than the textured film, whereas the opposite is true at higher strain rates. One possible explanation for this trend is that at lower rates the non-textured film accommodates the deformation through both dislocation plasticity and diffusive processes, which leads to lower stresses compared to the textured film. At higher rates, both the films are likely to accommodate the deformation primarily through dislocation plasticity. And since the grains in the textured film have a relatively high average Schmid factor (s = 0.408), the flow stress of the textured film is lower compared to the non-textured film.

3.4 Conclusions

Overall, the primary finding from our experiments is that the deformation behavior of UFG aluminum films is highly dependent on their texture. The texture-induced changes in deformation mechanisms can introduce substantial changes in strain rate sensitivity, even in films that have nearly identical mean grain sizes and thickness. Thus, it is important

to consider both the effect of texture as well as grain size in inferring the deformation mechanisms of UFG metals from strain rate sensitivity measurements.

CHAPTER 4

GRAIN ROTATIONS IN ULTRAFINE-GRAINED ALUMINUM FILMS STUDIED USING IN-SITU TEM STRAINING WITH AUTOMATED CRYSTAL ORIENTATION MAPPING

4.1 Introduction

The primary objective of the study in this chapter is to understand the deformation mechanisms in UFG Al films that have a random orientation of grains (no preferred texture). The study was motivated by the experiments, outlined in the previous chapter, which showed that non-textured UFG Al films have an unusually large SRS, possibly caused by time dependent grain rotations (Izadi and Rajagopalan 2016).

Here, we used in-situ tensile straining with ACOM-TEM to monitor the changes in grain orientations during load-unload experiments on non-textured UFG Al films and to obtain quantitative information about the magnitude and nature of such rotations.

4.2 Materials and Experimental Procedure

A 200 nm thick non-textured Al film was deposited on 200-µm thick, 100 mm diameter, (001)-oriented silicon (Si) wafers using DC magnetron sputtering with a methodology described in chapter 3 resulted in a film with random orientation of grains. A statistical analysis of bright field images of the Al film, obtained using a JEOL 2010F TEM, revealed a mean grain size of 180 nm (Figure 16a). Twin boundaries (primarily Σ3) comprised about 10% of the total grain boundary length in the as-deposited film. A similar

fraction of twin boundaries has been previously reports on vapor deposited UFG Al films. (F. Mompiou et al. 2013)

A MEMS device of a design I was co-fabricated with a freestanding sample of the film (Figure 8a), identical to the device shown in chapter 2. The macroscopic stress and strain on these films was measured using the methodology explained in that chapter, with the same level of uncertainty in the measurements.
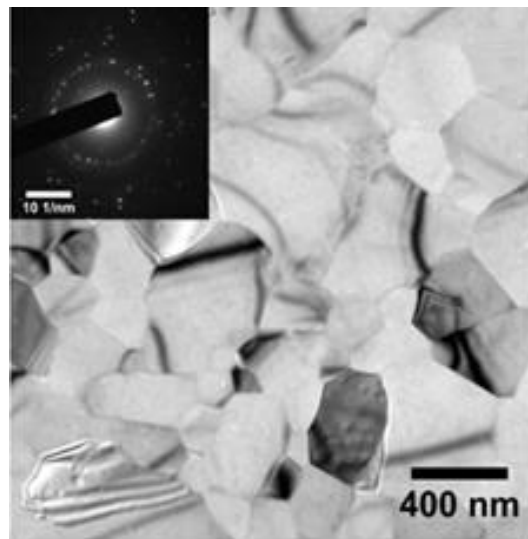
Figure 16: Bright-field TEM image of a 200 nm thick, non-textured aluminum film with a mean grain size of 180 nm. Selected area diffraction (SAD) of the film showing the lack of texture (inset).

The mechanical behavior of the thin film specimen was investigated through in-situ TEM tensile load-unload experiment. The averaged strain rate in the experiment was less than 10^{-5}/s, resulting in quasi-static loading and unloading.

For the in-situ TEM tensile experiment, the MEMS device was mounted on a displacement controlled single tilt straining holder described in section 2.4 (Figure 10b) and loaded on to a JOEL ARM200F TEM equipped with the Nanomegas ASTAR system

for ACOM data acquisition. Strain pulses (typically corresponding to <0.1% strain) were applied to the sample and the stress-strain data was recorded after allowing the film to relax for two minutes. The displacement applied on the MEMS device was kept constant when ACOM-TEM data was acquired. The data was collected from the same $3 \ \mu m \times 3 \ \mu m$ area at three strain levels during loading and two strain levels during unloading with a step size of 10 nm. It is relevant to note that the number of grains (325) in the scanning area is sufficiently large to provide meaningful statistics but is still small compared to the total number of grains in the sample (~800,000). Thus, electron beam-induced relaxation (Sarkar, Rentenberger, and Rajagopalan 2015) in the scanning area is unlikely to change the overall stress-strain response.

Before scanning, a probe with ~1 nm diameter was generated using spot size 4 and 10 µm C2 aperture. The spot diffraction patterns were then obtained using a beam precession angle of 0.4°, and a camera length of 120 mm. Finally, the indexing of the acquired ACOM-TEM data was performed by matching the spot diffraction patterns with a bank of templates for aluminum using the ASTAR software package to generate the crystal orientation maps. Note that the template matching process considers both the location and relative intensities of the diffraction spots and results in an angular resolution of ~0.3° (E. F. Rauch and Véron 2014).

The ACOM maps provided information of the Euler angles, cross correlation index and reliability index for the scanned points. After all the orientation maps were aligned with respect to each other, the analyses were done only on grains with a reliability index greater than 15 (Figure 17), as suggested in (E. F. Rauch and Véron 2014). Based on this criterion, 31 of the 325 grains of the non-textured film in the scanning area were found to

be unreliably index and their data was discarded. In addition, 44 grains had a large spread in the point-to-point orientation (standard deviation > 0.1°) and were also not considered for analysis. For the remaining 250 grains, mean grain orientations were calculated by averaging the orientations of the all the points within a grain. This mean grain orientation was used for all further analysis.
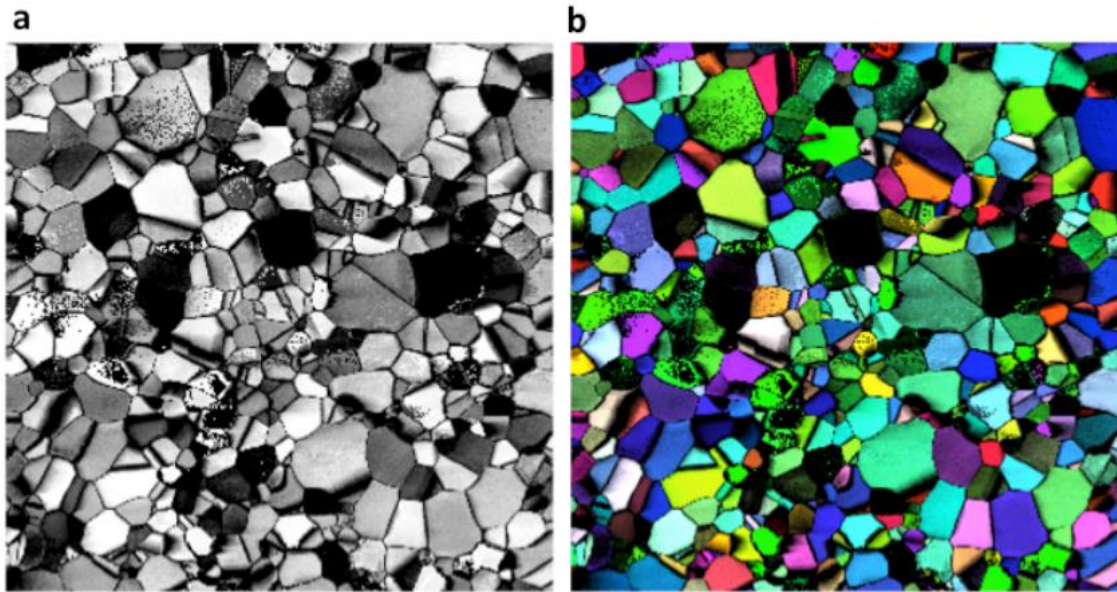
Figure 17: a) Reliability map for indexing in the scanned area with a reliability index cutoff of 15. Black indicates a reliability index of 15 or less. White indicates a reliability index of 66 or greater. b) Reliability map overlaid on the out-of-plane orientation map.

4.3 Results and Discussion

Figure 18a shows the stress-strain response of the 200 nm non-textured films during the in-situ TEM experiment. As indicated on the stress-strain curve, the orientation maps were obtained at 0.7%, 1.3% and 1.9% strain during loading (from here on referred to as 0.7% L, 1.3% L and 1.9% L), and at 1.7% and 1.6% strain during unloading (from here on referred to as 1.7% UL and 1.6% UL) of the non-textured film. At all these scan points, it

took between 15-30 minutes to switch the TEM from imaging to scanning mode and another 30 minutes to subsequently perform the scan. This led to significant time-dependent stress relaxation at each of the scanning points during loading. Nevertheless, we tried to minimize electron-beam induced relaxation by using a 200 kV beam with low intensity, as suggested in (Sarkar, Rentenberger, and Rajagopalan 2015). We also note that since the scan is performed point-by-point and the probe size is very small (1 nm diameter), the area illuminated at any instant is negligible compared to either the average grain size (180 nm) or the dimensions of the sample (75 μm wide, 375 μm long). Therefore, we expect that beam-induced artifacts are minimal.

Using the mean orientation of each grain at different loading and unloading points, a systematic analysis was done to investigate their orientation changes. To quantify the grain rotations, we first calculated the rotation matrix required to transform the crystal coordinate axes ([100], [010] and [001] directions) of each grain from its current configuration to its reference configuration (at 0.7%L). Then, we converted this coordinate axes transformation for each grain i, into a rotation (θ_i) about an arbitrary axis (Euler rotation theorem) as schematically depicted in Figure 19. We denote θ_i as the total rotation of each grain. We further decomposed this rotation into two rotations – first, about the out of plane normal to the film (parallel to electron beam direction), followed by a rotation about an arbitrary direction in the plane of the film, as shown in Figure 19. We designate the grain rotation about the film normal (ψ_i) as in plane rotation and the subsequent rotation (φ_i) as the out of plane rotation.
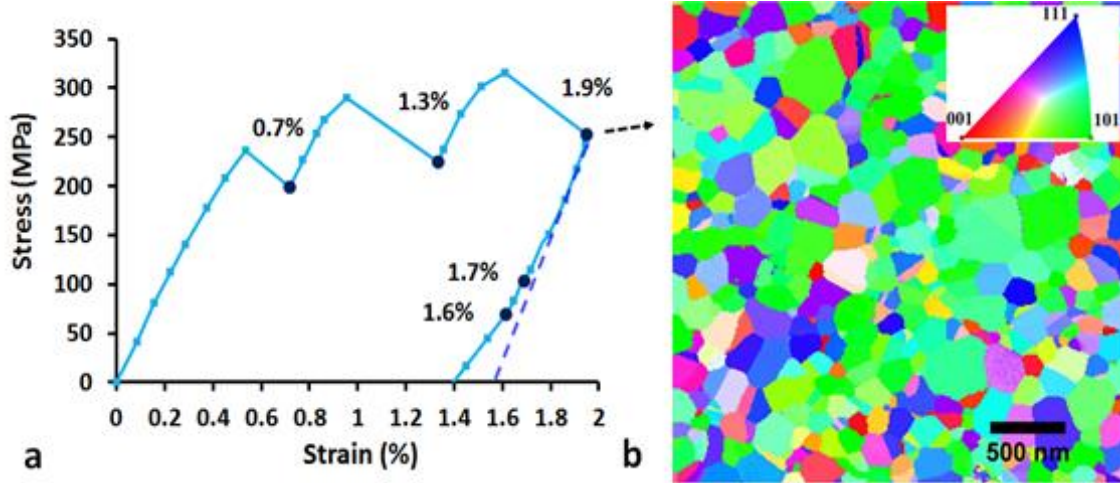
Figure 18: a) Stress-strain response of the 200 nm non-textured Al film during in-situ ACOM-TEM experiment. The orientation maps were acquired at three points during loading (0.7%, 1.3% and 1.9% strain) and two points during unloading (1.7% and 1.6% strain). b) An ACOM- map showing the color-coded out of plane orientation of the grains in the scanning area.
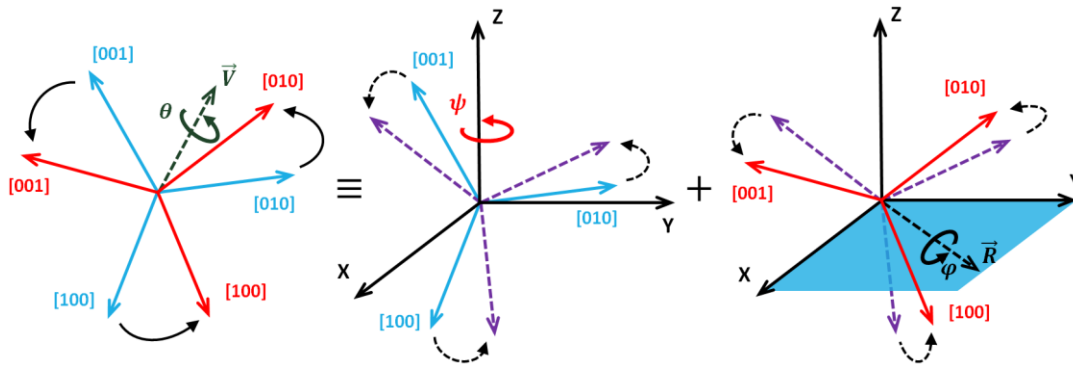
Figure 19: Schematic of the analysis of grain rotations from the ACOM-TEM data. The red axes represent the reference crystallographic axes of a grain. The blue axes represent the crystallographic axes of the grain in the deformed state where it has undergone rotation. A rotation θ about the direction $\vec{V}$ transforms the axes in the deformed configuration to the reference configuration. This axes transformation can also be accomplished by two rotations – an in plane rotation ψ about Z-axis (normal to the film) followed by an out of plane rotation φ about $\vec{R}$, which lies in the X-Y plane.

To ensure that a rigid body rotation of the film did not cause the grain orientation changes, the following steps were taken. The grain orientation maps were acquired from an area close to the midpoint (width-wise) of the film and away from the sample ends so that the deformation was uniaxial. Furthermore, the reference scan was taken after a sufficiently large strain (0.7%L and 0.4%L) had been imposed to ensure that the initial

37

buckling in the film was completely removed. For the same reason, the scans during unloading were also taken well before the film was fully unloaded. It should be noted that, during both loading and unloading, roughly 20-40% of the grains exhibited no change in their local orientation, which confirms that there was no global rotation/tilt of the film.

Figure 20 provides a histogram of grain orientation changes that occurred during loading and unloading. As evident from the figure, the number of grains experiencing rotations increased from 144 to 193 as strain was increased from 1.3% to 1.9% during loading. In addition, the magnitude of rotation (θ) of the grains also increased. While the average θ_{avg}^{all} (including grains that did not undergo any rotation) was about 0.8° when the strain was increased from 0.7% to 1.3%, it increased to 1.2° when the strain was increased to 1.9%.

When the sample was unloaded to 1.7% strain the average θ did not change (1.2°). But surprisingly, it increased again to 1.4° when the sample was further unloaded to 1.6% strain. Figure 21 shows the in plane and out of plane rotations of the grains at 1.9% strain during loading of the non-textured film. The average in plane rotation (1.3°) was slightly higher compared to the out of plane rotation (1.1°). However, the fraction of grains undergoing in plane and out of plane rotations was roughly similar.

In addition to grain rotations, the in-situ ACOM-TEM experiment also revealed some unusual phenomena. Several grains showed an increase/decrease in size during loading, which is consistent with previous studies on deformation induced grain growth in UFG and NC metals (Gianola, Van Petegem, et al. 2006; Kobler et al. 2013). However, unlike previous reports, we observed changes in grain size even during unloading, when the applied stress had been considerably reduced. Figure 22 and Figure 23 provide, two

38

different examples of this phenomenon. Figure 22 shows a grain that reduced in size while loading, continued to shrink during unloading and was completely annihilated. Figure 23, in contrast, shows a grain that exhibited reversible growth. The size of this grain increased during loading (from ~9300 nm2 to ~12400 nm2) but shrunk (to 6700 nm2) when the sample was unloaded. We also observed detwinning during both loading and unloading in some grains, as shown in Figure 24.
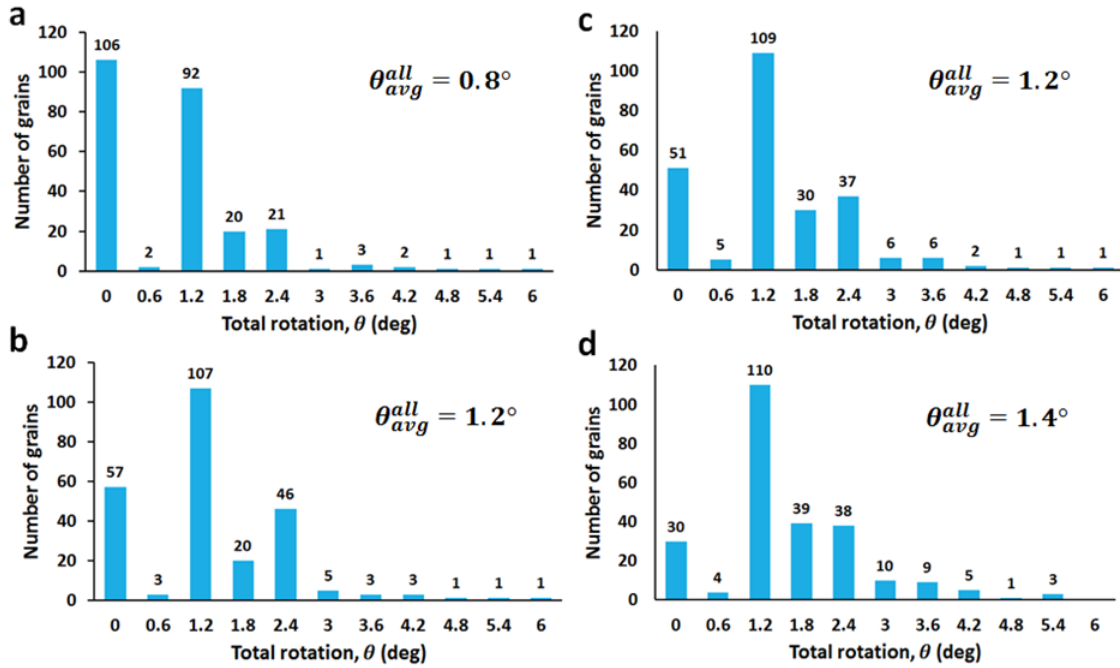
Figure 20: Histogram of the total rotation induced in approximately 250 grains during loading of the non-textured film from a) 0.7% strain to 1.3% strain and b) 0.7% strain to 1.9% strain. Histogram of grain rotations at the two unloading points, c) 1.7% strain and d) 1.6% strain. Note that the grain rotations for the unloading points are also calculated with respect to reference configuration at 0.7% strain during loading.
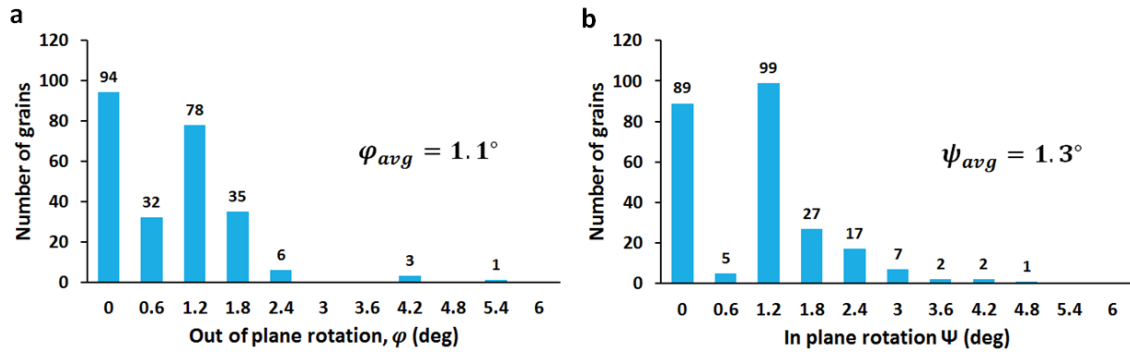
Figure 21: a) Histogram of out of plane grain rotations during loading of the non-textured film from 0.7% strain to 1.9% strain. b) Histogram of in plane grain rotations during loading from 0.7% strain to 1.9% strain.
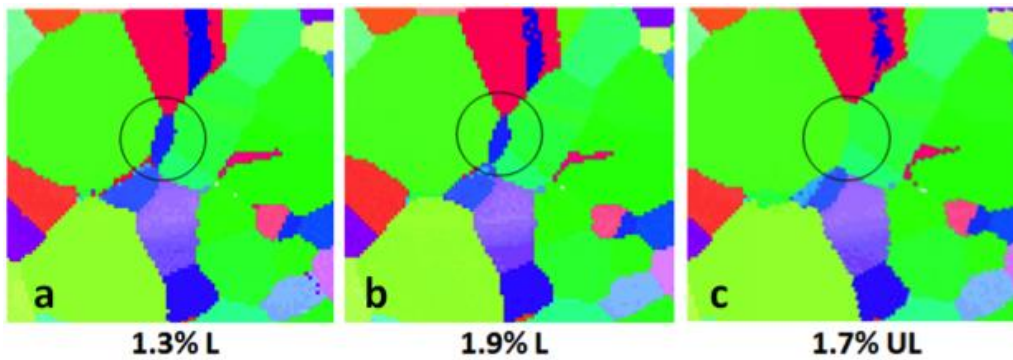
Figure 22: Progressive reduction in size and complete annihilation of a grain (marked by the black circle) during loading and unloading of the non-textured film.
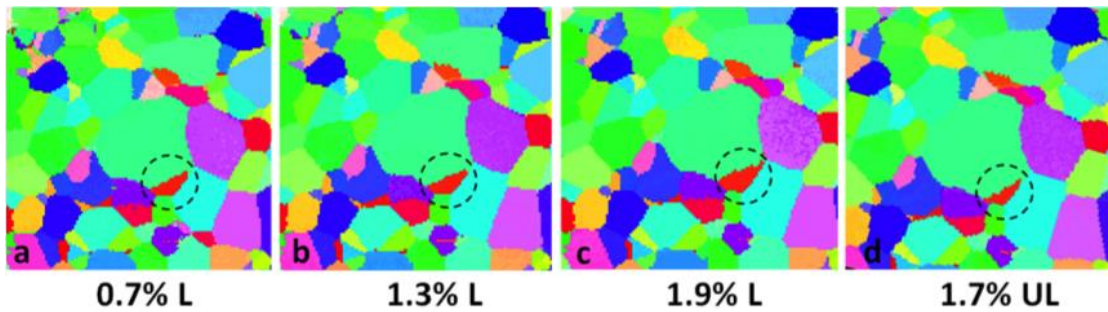
Figure 23: Reversible change in size of a grain (marked by the black dashed circle) during loading and unloading of the non-textured film. The size of the grain increased during loading but reduced as the sample was unloaded.

40
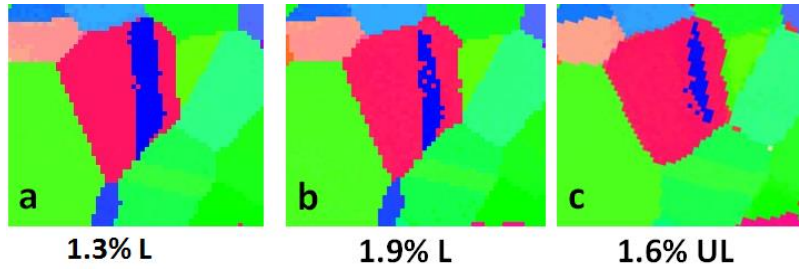
Figure 24: Detwinning in a grain during loading and unloading of the non-textured film.

The experiments on non-textured UFG Al films reveal high strain rate sensitivity, and a large Bauschinger effect during quasi-static load-unload experiments. The ACOM-TEM measurements provide evidence of extensive grain rotations during loading. Unexpectedly, significant microstructural changes (grain rotation, grain annihilation, detwinning) also occur during unloading. These observations point to a highly heterogeneous deformation and a continuous redistribution of stresses in the film, as we discuss below.

Since the film has no preferred texture, loading occurs along a random crystallographic direction for each grain. Thus, depending on the orientation of the grain with respect to the loading axis, the elastic modulus can vary from 63.7 GPa ([100] direction) to 76 GPa ([111] direction). This would result in elastic strain mismatch between the grains, even before the grains have begun to deform plastically. More importantly, when the grains start to deform plastically, the variation in the maximum Schmid factor of the grains, which ranges from 0.27 to 0.5 for uniaxial loading, leads to considerable difference in the resolved shear stress required to activate slip. In addition, the critical resolved shear stress required to activate slip is likely to be higher for relatively smaller grains compared to larger grains.

The combination of these factors (variation in grain size and Schmid factor) will result in considerable stress difference and plastic strain mismatch between plastically soft (large size and high Schmid factor) and hard grains (small size and low Schmid factor) as the strain is increased. Therefore, neighboring grains need to bend or rotate with respect to each other to maintain strain compatibility. The back stresses resulting from the inhomogeneous stress distribution would also lead to reverse yielding in the plastically soft grains during unloading, which would manifest as inelastic strain recovery (Bauschinger effect). Previous studies on UFG aluminum films have, indeed, revealed substantial back flow (reverse dislocation motion) during cyclic loading-unloading experiments (Frédéric Mompiou et al. 2012). The reverse motion of dislocations was shown to occur either due to back stresses arising from grain boundary pile-ups or because the dislocations were not fully inserted into the grain boundaries during loading.

The results from ACOM-TEM experiment are consistent with the above description of the deformation behavior. As shown in Figure 20, both the number of grains that undergo orientation changes and the magnitudes of their rotation increase with strain during loading. Note that grain rotations could be accommodated by a combination of elastic and plastic deformation. The plastic deformation associated with grain rotation is likely to be mediated by dislocations in UFG metals, as shown in previous studies (F. Mompiou and Legros 2015). The presence of several grains with large misorientation gradients, which require geometrically necessary dislocations, in our sample also points to the same conclusion.

Notably, during unloading of the non-textured film the average grain rotation did not change initially (θ_{avg}^{all}= 1.5°) and then increases to 1.4°, which can be understood as follows. During the initial stages of unloading, the stresses in all the grains reduce and the

42

rotations induced by elastic incompatibility between the grains are reversed. Upon further unloading, however, plastically soft grains undergo reverse yielding because of stress reversal, which manifests as the macroscopic Bauschinger effect. This reverse yielding leads to a reduction of back stresses in these soft grains and redistributes the stresses in their neighborhood, which necessitates further rotation of the surrounding grains to maintain compatibility. As a result, θ_{avg}^{all} again increases.

To verify if this is true, we analyzed the rotations of the grains during unloading with respect to the end of loading (1.9% strain). But because the rotation axis is not constant at different loading and unloading points even for the same grain, it is not appropriate to directly measure the difference in θ. However, such a comparison is more meaningful for in plane rotations (ψ) because they are always defined with respect to the film normal. Therefore, we decomposed the rotations into in plane and out of plane components and analyzed the in plane rotations as follows. If a grain rotated in the same direction about the film normal during both loading and unloading, we classify those rotations as forward rotations. If the sense of rotation during unloading was opposite to that of loading, we denote them as reverse rotations. Finally, if a grain showed no rotation during loading but had non-zero rotation during unloading, we classify those as uncorrelated rotations. The relative in plane rotations (ψ_{rel}) of the grains based on this classification scheme are plotted in Figure 25.

The results show that the proportion of grains that exhibit relative in plane rotation (with respect to end of loading) increased as the sample was unloaded further. Specifically, the number of grains that underwent reverse rotations increased from 54 to 60 as the strain was decreased from 1.7% to 1.6%. More importantly, the number of grains that undergo

uncorrelated rotations increased even more (from 32 to 51). Such uncorrelated grain rotations, as argued earlier, are consistent with redistribution of stresses triggered by reverse yielding of plastically soft grains. Surprisingly, the number of grains that exhibit forward rotations also increased (from 11 to 20) with unloading. The forward rotations suggest that the local stress state remains similar for these grains during both loading and unloading, even though the macroscopic stress is substantially different.

The presence of grain rotations during unloading is also consistent with the qualitative observations of the evolving microstructure. As shown in Figure 22, Figure 23 and Figure 24 there is evidence of both reversible and irreversible migration of grain/twin boundaries. It has been shown that these grain boundary migrations are primarily driven by the local stress state (Rupert et al. 2009) and have been attributed to shear-coupled grain boundary motion (Rajabzadeh et al. 2013). Therefore, a reverse migration of a grain boundary during unloading (Figure 23) likely reflects a reversal in the local stress state. In contrast, the continued migration of a grain/twin boundary (Figure 22 and Figure 24) would suggest that the local stress state remains similar to that during loading. While previous studies have reported grain rotation and growth in UFG and NC metals during loading (Kobler et al. 2013; F. Mompiou and Legros 2015), our observations strongly imply that both grain orientations and the microstructure continue to evolve during unloading.

Finally, we would like to note that the fraction of grains observed to undergo rotations in our non-textured UFG aluminum film is significantly larger compared to previous reports on UFG aluminum films (Idrissi et al. 2014; F. Mompiou and Legros 2015) , even though the applied strain is substantially lower in our case (2% compared to 6-7% in (Idrissi et al. 2014) and (F. Mompiou and Legros 2015).
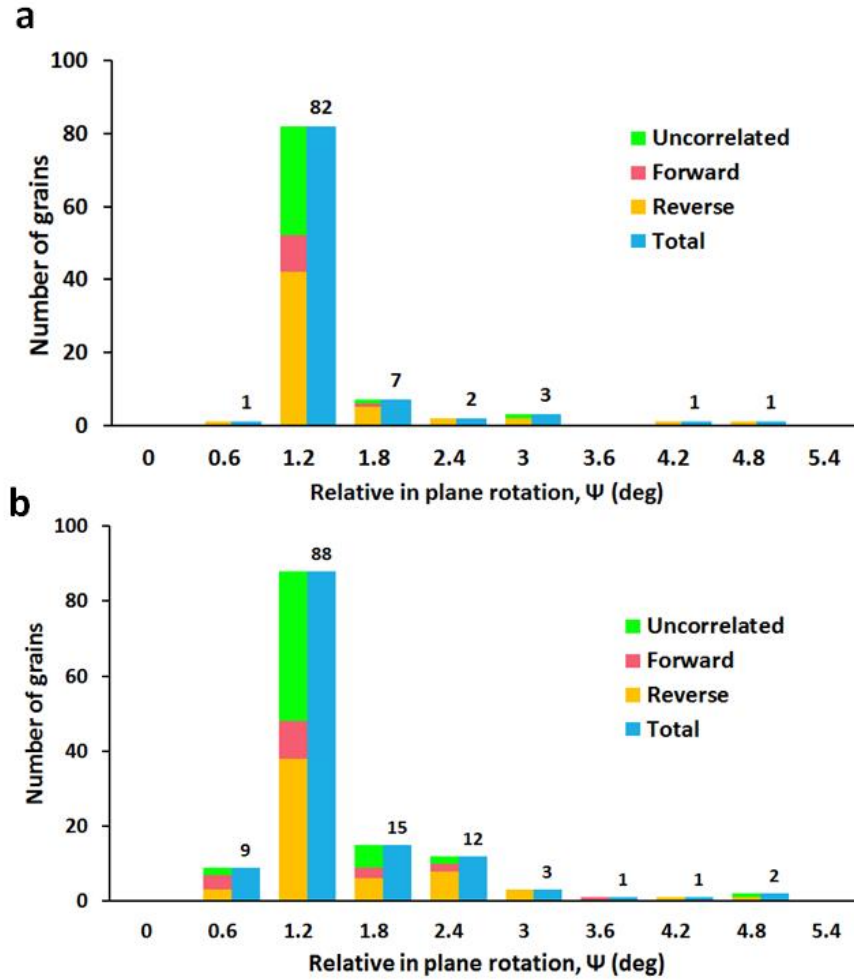
Figure 25: Histogram of grains that exhibited in plane rotations during unloading of the non-textured film with respect to the end of loading. The classifications are based on the scheme explained in the text. (a) corresponds to 1.7% strain during unloading whereas (b) corresponds to 1.6% strain during unloading.

This disparity is most likely caused by differences in the texture of the films that were investigated. The films in both (Idrissi et al. 2014) and (F. Mompiou and Legros 2015) had a strong (111) texture, whereas our film had no preferred texture. A (111) texture is likely to make the deformation more homogeneous for two reasons. The (111) plane is transversely isotropic (same Young's modulus in all directions) and therefore elastic strain mismatch between grains is minimized. The (111) texture also leads to a significantly

narrower range of maximum Schmid factors (0.408 to 0.471) for the grains compared to a non-textured film (0.27 to 0.5), which drastically reduces the heterogeneity in stress distribution induced by plastic anisotropy. As a result, there is much less need for grain rotation in a bicrystalline and (111) textured film to maintain strain compatibility.

4.4 Conclusions

The deformation behavior of a non-textured and bicrystalline UFG aluminum film was studied using quasi-static ex-situ and in-situ ACOM-TEM load-unload experiments. An analysis of the ACOM data reveals extensive grain orientation changes during deformation. During loading of the non-textured film, the number of grains that undergo rotations increases with strain, and at 1.9% strain more than 75% of the grains experience rotations greater than 0.3°. These pervasive grain rotations, which are time-dependent (Izadi and Rajagopalan 2016), can explain the high strain rate sensitivity of non-textured Al films.

During unloading, >52% of the grains experienced in-plane rotations as the sample strain was decreased from 1.9% to 1.6%. Among these grains, about 46% underwent reverse rotations. The rest exhibited uncorrelated rotations (39%) or forward rotations (15%), which is consistent with redistribution of stresses triggered by reverse yielding of plastically soft grains. Overall, the microstructural observations point to a spatially inhomogeneous stress distribution in the film that constantly evolves during both loading and unloading. From a broader perspective, the results demonstrate how the combination of in-situ straining and ACOM-TEM can provide a quantitative description of the microstructural evolution in UFG metals during deformation.

CHAPTER 5

STRAIN RATE DEPENDENCE OF CYCLIC DEFORMATION RESPONSE IN ULTRAFINE-GRAINED AL FILMS WITH DIFFERENT TEXTURES

5.1 Introduction

In previous chapters, we showed that ultrafine-grained Al films with similar mean grain size and thickness but with very dissimilar textures show significantly different mechanical behavior, arising from the differences in their microstructural heterogeneity that induces time-dependent grain rotations during deformation of these films. Furthermore, quantitative investigation of such rotations in the non-textured Al film pointed to the presence of grain rotations during unloading that was accompanied by deviation from linear unloading behavior (Bauschinger effect). The time-dependent nature of these rotations that could essentially influence the unloading behavior of the films motivated the study of SRS of the mechanical response of UFG Al films during unloading. Therefore, we investigated the strain rate dependent, cyclic deformation response of freestanding UFG aluminum films with highly dissimilar texture through cyclic load-unload experiments at different strain rates.

5.2 Materials and Experimental Procedure

The (110) textured bicrystalline Al film (labeled as textured film) and the non-textured Al film were synthesized by carefully controlling the deposition conditions during DC Magnetron sputtering following the methodology explained in chapter 3. The textured film and non-textured film were deposited to a thickness of ~180 nm and ~175 nm at 5.5

nm/min, respectively. The chamber base pressure during deposition of the textured and non-textured film was 9×10^{-8} Torr and 1×10^{-7} Torr, respectively.
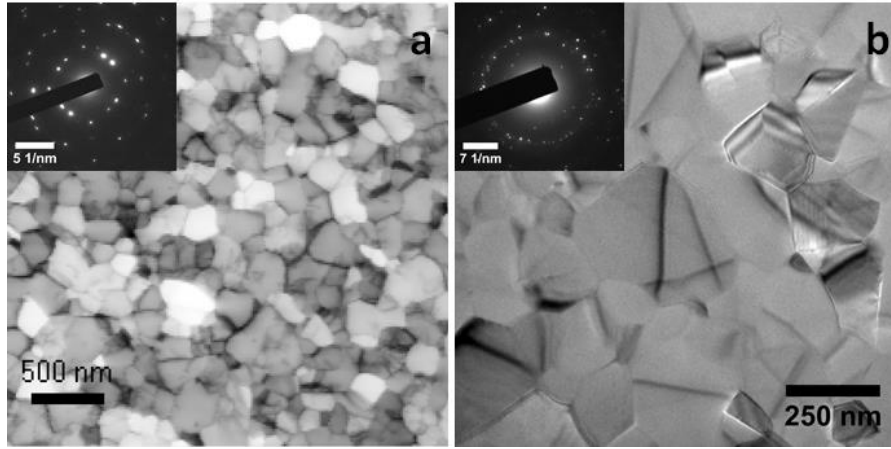
Figure 26: (a) Bright-field TEM image of a 180 nm thick, bicrystalline aluminum film with a mean grain size of 220 nm. Selected area diffraction (SAD) of the film showing an (110) out-of-plane texture with two in-plane variants rotated 90° with respect to each other (inset). (b) Bright-field TEM image of a 175 nm thick, non-textured aluminum film with a mean grain size of 180 nm. Selected area diffraction (SAD) of the film showing the lack of texture (inset).
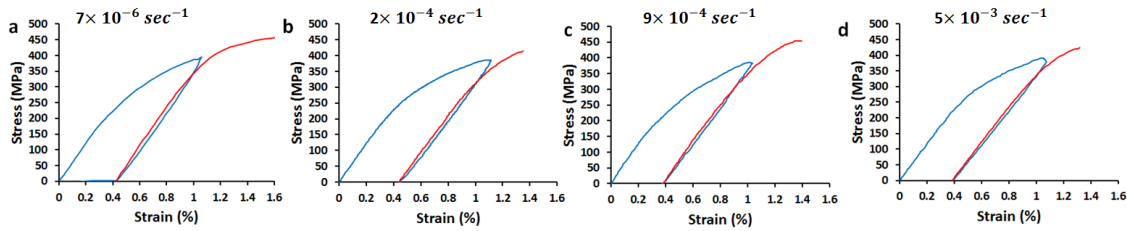
Figure 27: Stress-strain response of the 180 nm thick bicrystalline Al film at different strain rates. (a) 7×10^{-6} s^{-1}. (b) 2×10^{-4} s^{-1}. (c) 9×10^{-4} s^{-1}. (d) 5×10^{-3} s^{-1}.
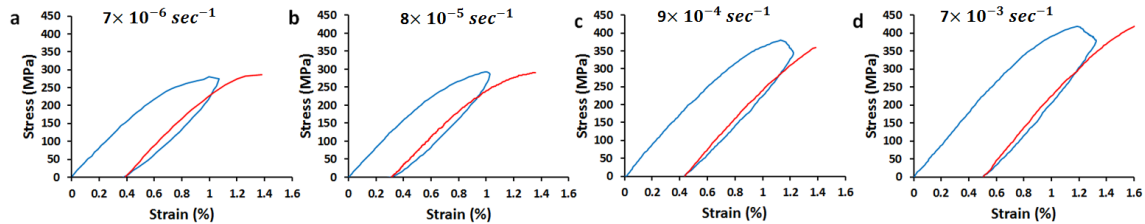
Figure 28: Stress-strain response of the 175 nm thick non-textured Al film at different strain rates. (a) 7×10^{-6} s^{-1}. (b) 8×10^{-5} s^{-1}. (c) 9×10^{-4} s^{-1}. (d) 7×10^{-3} s^{-1}.
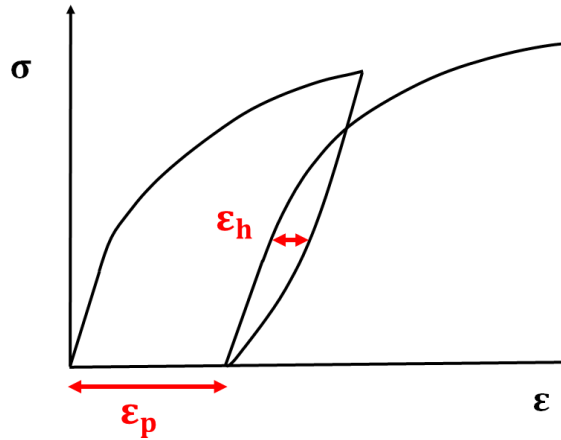
Figure 29: Schematic of stress-strain response of the Al films during cyclic load-unload experiments. ε_h and ε_P represents the hysteresis strain and plastic strain, respectively.

The microstructure of the films was examined through transmission electron microscopy (TEM). Based on plan-view TEM images the textured Al film had a mean grain size of 220 nm and the non-textured film had a mean grain size of 180 nm (Figure 26). The images also indicated a columnar grain structure with one grain traversing the thickness of the film. Freestanding Al samples co-fabricated with MEMS devices (Figure 8) of design I (described in chapter 2) were employed to carry out the experiments. The methodology described in section 2.3 was used to track the sample deformation during the experiments.

In all the experiments, loading was along the [001] direction of the Al[001]//Si[110] grain family for the textured film and along an arbitrary direction for the non-textured film. To eliminate possible variation in mechanical behavior that can arise from sample size effects, we ensured that all the samples from both sets of films had identical dimensions (effective gauge length 375 μm, width 75 μm). At least 2 samples were tested for each experimental condition to ensure repeatability.

49

5.3 Results and Discussion

Figure 27 and Figure 28 show the cyclic stress-strain response of the textured and non-textured film at different strain rates. As evident from Figure 27, the stress-strain response of the textured film during the first loading was very similar over the entire range of strain rates. For instance, the stress at 0.8% strain was within 5 MPa, which is smaller than the uncertainty in stress measurement, for all the strain rates. However, the unloading and reloading behavior of the textured film showed some variation with strain rate. At the lowest strain rate, the unloading response was more nonlinear (indicative of early Bauschinger effect) and this resulted in a greater hysteresis in the stress-strain response. The stress-strain hysteresis, however, decreased with increasing strain rate with the hysteresis strain (ε_h as shown in Figure 29) decreasing from 0.04% at the lowest strain rate to 0.027% at the highest strain rate.

The non-textured film, in contrast, showed considerable difference in stress-strain response over a similar range of strain rates (Figure 28). The stress at 0.8% strain during the first loading increased from 256 MPa to 338 MPa as the strain rate was increased from 5.6×10^{-6}/s to 7.1×10^{-3}/s. In addition, there was significant relaxation as the samples were unloaded, especially at the higher strain rates. The film also exhibited softening at the lowest strain rate, which was particularly evident during the second loading. The unloading and reloading response of the non-textured film was also strongly dependent on the strain rate. At the lowest strain rate, there was a noticeable Bauschinger effect, which led to a fairly large hysteresis strain ($\varepsilon_h = 0.085\%$). Note that this value is more than twice that of the textured film ($\varepsilon_h = 0.04\%$) at a comparable strain rate. Nevertheless, the hysteresis

strain diminished as the strain rate was increased, reducing to 0.054% at the highest strain rate.

Previous studies have shown that the strain rate sensitivity progressively increases as the grain size is reduced from the microcrystalline to the NC regime, due to the changes in deformation mechanisms that accommodate plasticity (Schwaiger et al. 2003; Dalla Torre et al. 2005; Wang, Hamza, and Ma 2006; Dao et al. 2007). In our previous work (Izadi and Rajagopalan 2016), we have shown that differences in film texture can lead to widely different strain rate sensitivity of flow stress in UFG metal films, even when their mean grain size and thickness are nearly identical. The results shown in Figure 27 and Figure 28 indicate that the strain rate dependence of the cyclic deformation response, particularly the stress-strain hysteresis, is also strongly dependent on the film texture.

To understand these results, we first consider the behavior of the non-textured film. As shown in Figure 28, the film exhibits a distinct early Bauschinger effect (reverse yielding during unloading), especially at the lower strain rates. Both in-situ TEM studies and simulations have shown that this reverse yielding is caused by a highly inhomogeneous stress distribution, which, in turn, results from a heterogeneous microstructure. Recently, we have shown that non-textured Al films undergo pervasive grain rotations during loading and their reverse yielding during unloading is accompanied by significant reverse grain rotations (Izadi, Darbal, et al. 2017; Izadi et al. 2016). Moreover, these grain rotations, which lead to stress relaxation, are time dependent (Izadi and Rajagopalan 2016) and partly accommodated by diffusive processes. Therefore, when the strain rate is increased, the grain rotations are suppressed, resulting in higher stresses during loading. Likewise, the

51

absence of reverse grain rotations during unloading reduces the Bauschinger effect and leads to a smaller hysteresis strain.

Nevertheless, even at the highest strain rate there is a notable Bauschinger effect and stress-strain hysteresis in the non-textured film, which suggests that plasticity mechanisms that are characterized by much shorter time scales (e.g., dislocation glide) are still active. It is also worth noting that the hysteresis in the non-textured film at the highest strain rate exceeds the hysteresis in the textured film at the lowest strain rate, which clearly indicates that microstructural heterogeneity is a key factor in the stress-strain hysteresis observed in the UFG aluminum films investigated here.

Compared to the non-textured film, the mechanics of deformation are substantially different in the textured film. Since this film has a bicrystalline texture and is loaded along the [001] direction of the Al[001]//Si[110] grain family, both grain families have sufficient slip systems to accommodate the imposed deformation and all active slip systems in both families have the same Schmid factor ($s = 0.408$). In effect, plastic anisotropy is nearly eliminated. Combined with the low elastic anisotropy of Al, this leads to a much more homogeneous deformation, which results in markedly smaller early Bauschinger effect and hysteresis strain. In addition, because of the relatively high Schmid factor, dislocation plasticity is favored in both grain families, which makes the deformation behavior nearly rate-independent, at least in the strain rate regime probed in this study.

5.4 Conclusions

To summarize, our experiments reveal that the strain rate sensitivity of cyclic deformation behavior of UFG aluminum films is strongly dependent on their texture.

Changes in texture can lead to plastic deformation mechanisms that have substantially different strain rate sensitivities, which, in turn, can result in highly dissimilar macroscopic properties including flow stress, early Bauschinger effect and stress-strain hysteresis.

CHAPTER 6

EFFECT OF PLASTIC ANISOTROPY ON THE DEFORMATION BEHAVIOR OF BICRYSTALLINE ALUMINUM FILMS – EXPERIMENTS AND MODELING

6.1 Introduction

In the previous chapter, we established the substantial influence microstructural heterogeneity exerts on the mechanical response of the films with dissimilar textures during both loading and unloading; non-textured Al film with a more heterogeneous microstructure than the bicrystalline film showed significantly higher strain rate sensitivity of flow stress and early Bauschinger effect during deformation.

Nonetheless, we could also make the bicrystalline film deform more heterogeneously by loading it along different loading directions, which essentially changes the effect of plastic anisotropy on the deformation.

Here, we investigated the effect of texture-induced plastic anisotropy on the strain rate sensitivity and early Bauschinger effect of two UFG aluminum films with identical bicrystalline texture (two grain variants). The films were uniaxially loaded along two different directions with respect to the main crystallographic axes of the bicrystalline texture, such that the heterogeneity in the plastic behavior of the two grain variants due to plastic anisotropy was notably different.

6.2 Materials and Experimental Procedure

Two sets aluminum films (240 nm and 180 nm thick) were deposited on Si (100) wafers using DC magnetron sputtering with bicrystalline texture following the methodology explained in chapter 3. The deposition was performed under a base pressure of $\sim 10^{-7}$ Torr with ~5.5 nm/min deposition rate. The Al films grew in a heteroepitaxial manner with the following orientation relationship: Al(110)//Si(001), Al[001]//Si[1$\bar{1}$0] and Al(110)//Si(001), Al[001]//Si[110] (Niwa and Kato 1991), leading to two grain families with (110) out-of-plane texture that are rotated 90° in-plane with respect to each other. The microstructures of the films were examined through bright-field transmission electron microscopy (TEM) and ACOM-TEM techniques (chapter 5). Figure 30 shows bright-field TEM images of the two Al films, indicating a columnar grain structure.
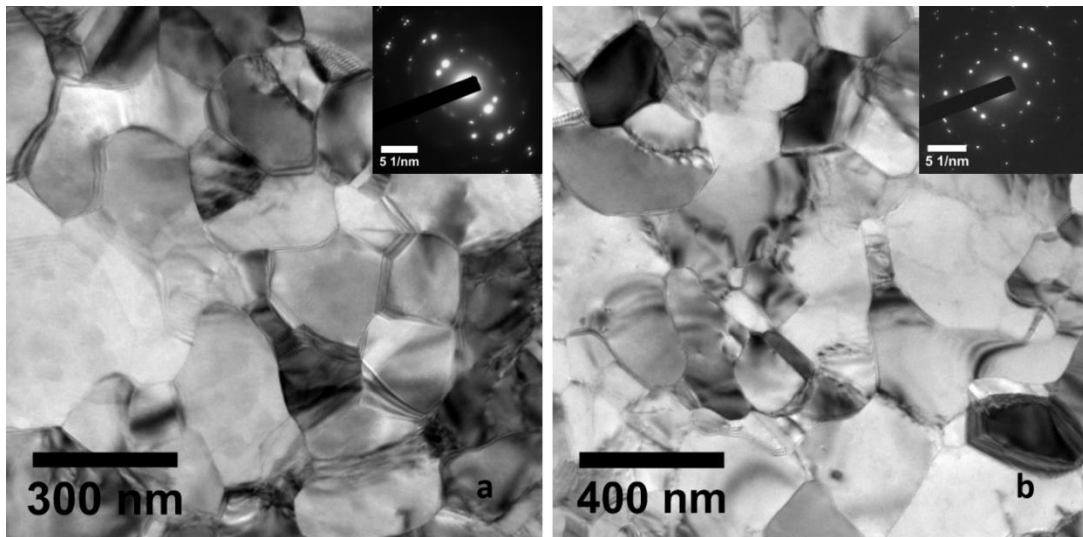
Figure 30: (a) Bright-field TEM image of a 180 nm thick, bicrystalline aluminum film with a mean grain size of 228 nm. (b) Bright-field TEM image of a 240 nm thick, bicrystalline aluminum film with a mean grain size of 275 nm. The selected area diffraction (SAD) patterns for both films (insets in (a) and (b)) show the (110) out of plane texture. The two in-plane variants that can be obtained by a 90° rotation with respect to each other about the out-of-plane direction.
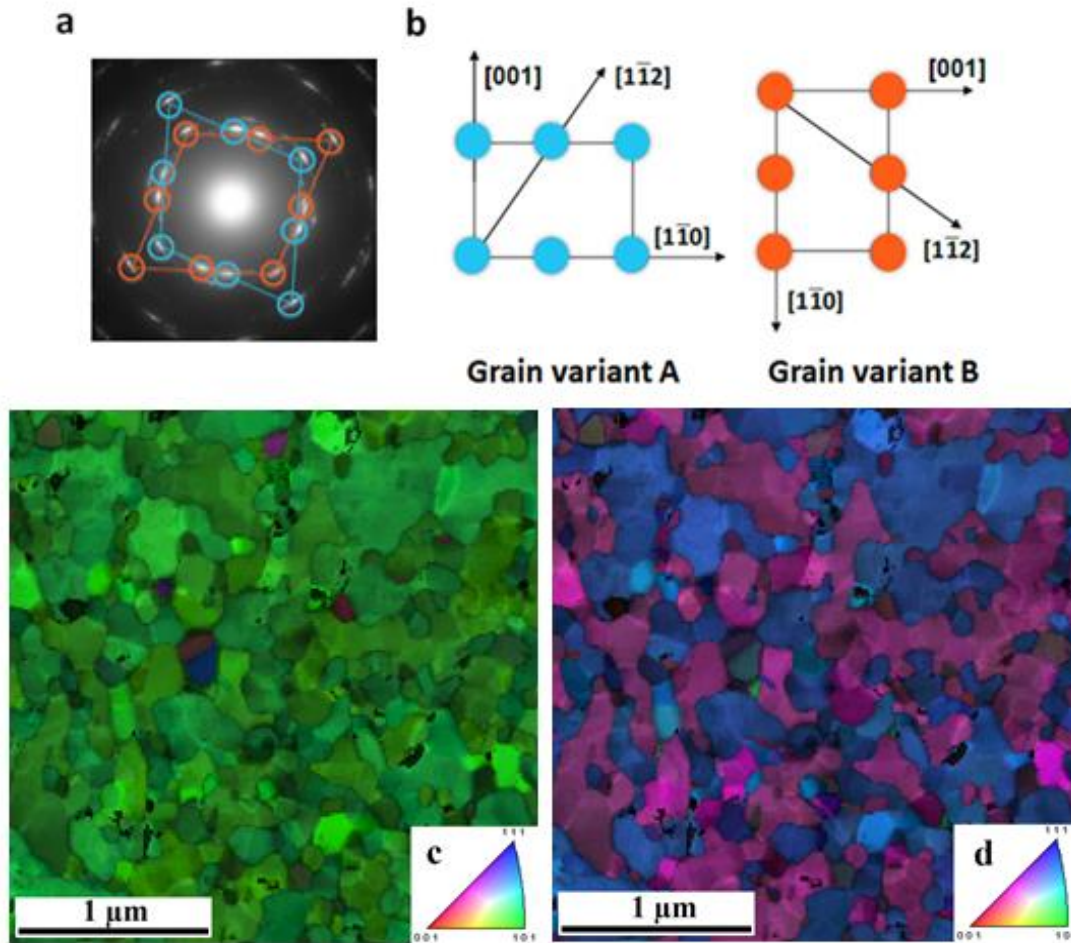
Figure 31: a) Diffraction pattern of the bicrystalline film, showing the spots (blue and red circles) from the two-grain variants. b) Schematic representation of the two variants and their corresponding crystal directions. c) Inverse pole figure map from one of the films with colors showing crystal orientations perpendicular to the film (color key for crystal directions is shown in the standard triangle legend). d) Inverse pole figure map of the same area as (c), but with colors corresponding to crystal axes parallel to the horizontal direction. The colors in (c) clearly show the strong (110) out-of-plane texture.

The 180 nm thick film had a mean grain size of 228 nm, whereas the 240 nm thick film had a mean grain size of 275 nm. Selected area diffraction (SAD) patterns taken along the [110]-zone axis (Figure 31a) showed that only two grain variants, which can be obtained by a $90°$ rotation with respect to each other in-plane, were present in the films. A schematic representation of these variants is shown in Figure 31b. The (110) out-of-

plane texture and the bicrystalline microstructure of the films were also confirmed by ACOM-TEM measurements (Figure 31c and Figure 31d). After the films were deposited, dog-bone shaped freestanding samples were co-fabricated with a MEMS device using microfabrication techniques outlined in chapter 2, to carry out both cyclic load-unload experiments as well as monotonic loading experiments with constant strain rates. For conducting these experiments and measuring the stress-strain response of the films, MEMS devices of design I (Figure 8) and II (Figure 9) were employed following the methodology described in chapter 2.

The MEMS devices were fabricated along two different orientations as illustrated in Figure 32 to allow loading of the samples along the $[001]$ and $[1\bar{1}2]$ directions of the grain variant A in the bicrystalline films. From here on, these directions are referred to as $[001]_{G\_A}$ and $[1\bar{1}2]_{G\_A}$, respectively. The $[001]$ and $[1\bar{1}2]$ directions of the grain variant A coincide with the $[\bar{1}10]$ and $[1\bar{1}1]$ directions, respectively, of the grain variant B. When the loading is along $[001]_{G\_A}$, there are eight active slip systems in grain variant A and four active slip systems in grain variant B. The Schmid factor (*s*) of all the active slip systems, in both the grain variants, is identical ($s = 0.408$); hence, this loading direction minimizes heterogeneity due to plastic anisotropy. In contrast, for loading along $[1\bar{1}2]_{G\_A}$, two slip systems, $\{111\}$ $[0\bar{1}1]$ and $\{1\bar{1}1\}$ $[\bar{1}\bar{1}0]$, of grain variant A have $s = 0.408$, whereas the maximum Schmid factor in grain variant B is only 0.272, leading to large heterogeneity due to plastic anisotropy. Since this study is intended to isolate the effect of plastic anisotropy on the deformation behavior of UFG Al films it is necessary to minimize other factors that could alter the mechanical response. Therefore, in addition to the mean grain

size, the specimen width (75 µm) and length (375 µm) were kept constant for all experiments.
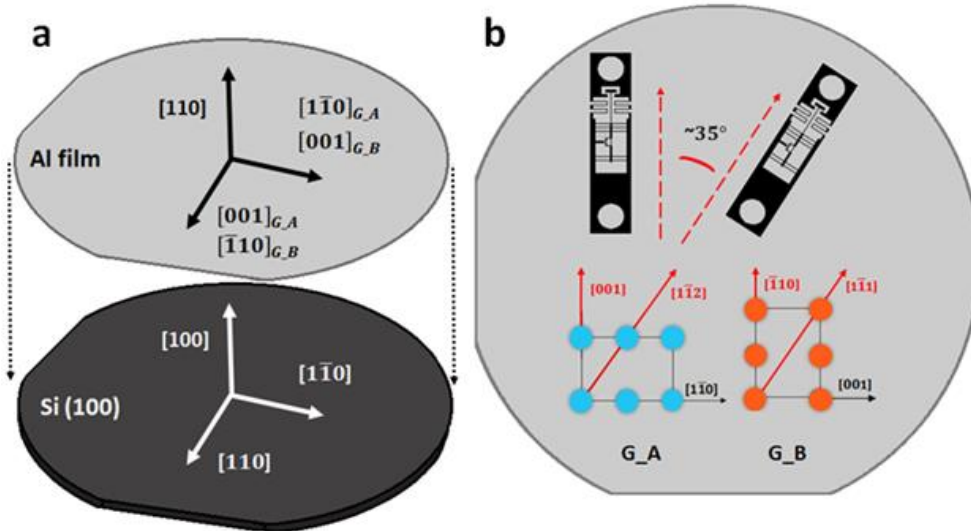
Figure 32: a) Schematic showing the epitaxial relationship between the Si substrate and the Al film. b) Orientation of the devices for loading the film along the two different directions ($[001]_{G\_A}$ and $[1\bar{1}2]_{G\_A}$).

To ensure the repeatability of the observations, at least two specimens were tested for each experimental condition. The mechanical behavior of the bicrystalline Al films was investigated through monotonic and cyclic load-unload tensile experiments along $[001]_{G\_A}$ and $[1\bar{1}2]_{G\_A}$ loading directions. The monotonic loading experiments were conducted on the 240 nm thick aluminum film at strain rates ranging from ~7×10^{-6} s^{-1} to 7×10^{-3} s^{-1}. The details of the procedure adopted for the strain rate experiments (Izadi and Rajagopalan 2016) can be found in chapter 3. We chose the stress at 0.8% strain ($\sigma_{0.8\%}$) as a measure of flow stress to quantitatively compare the response at different rates. The flow stress at 0.8% strain was chosen because macroscopic plasticity had set in before 0.8% strain and the samples failed around 1% strain at higher strain rates. The cyclic load-unload experiments

were conducted on the 180 nm thick Al film at a strain rate of $\sim 10^{-5}$ s^{-1}. The specimens were subjected to two deformation cycles before they fractured during the third loading.
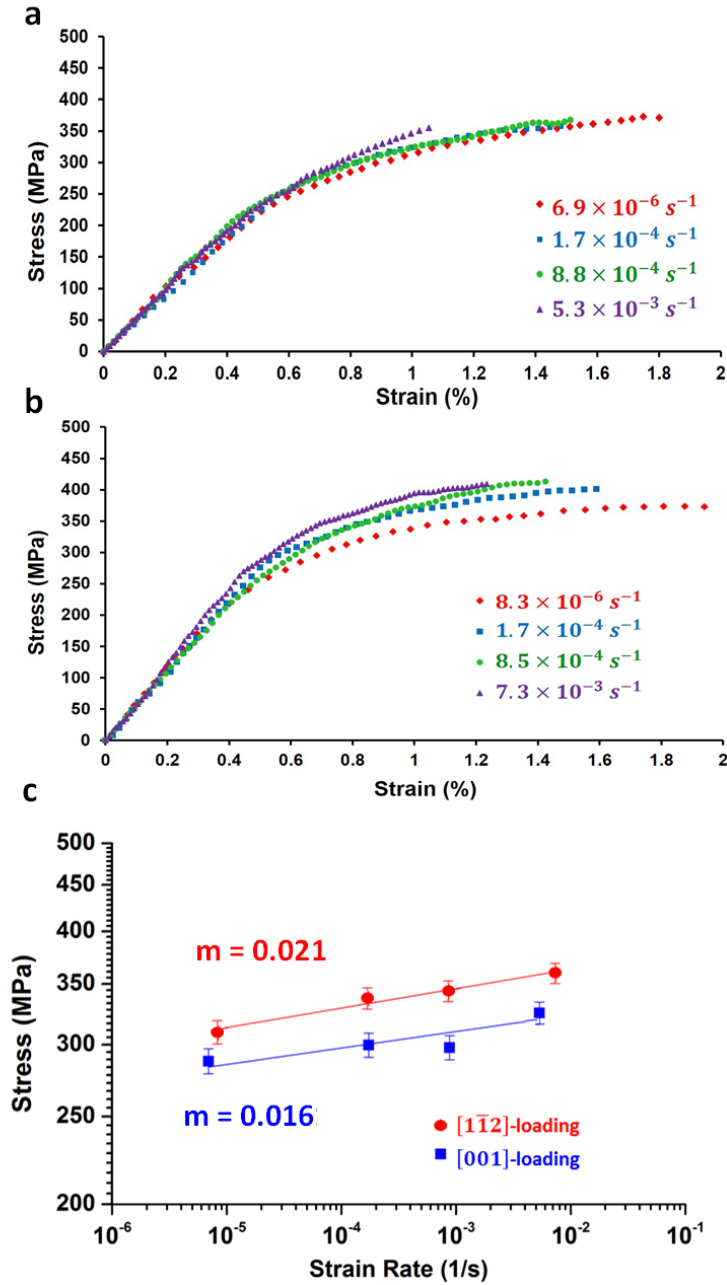
Figure 33: (a) Stress-strain response of the Al 240 nm film for $[001]_{G\_A}$ loading at different strain rates. (b) Stress-strain response of the Al 240 nm film for $[1\bar{1}2]_{G\_A}$ loading at different strain rates. (c) Log-log plot of flow stress versus strain rate for the two loading directions. The error bars indicate the bounds of uncertainty in flow stress arising from both film thickness variation and load cell fluctuations.
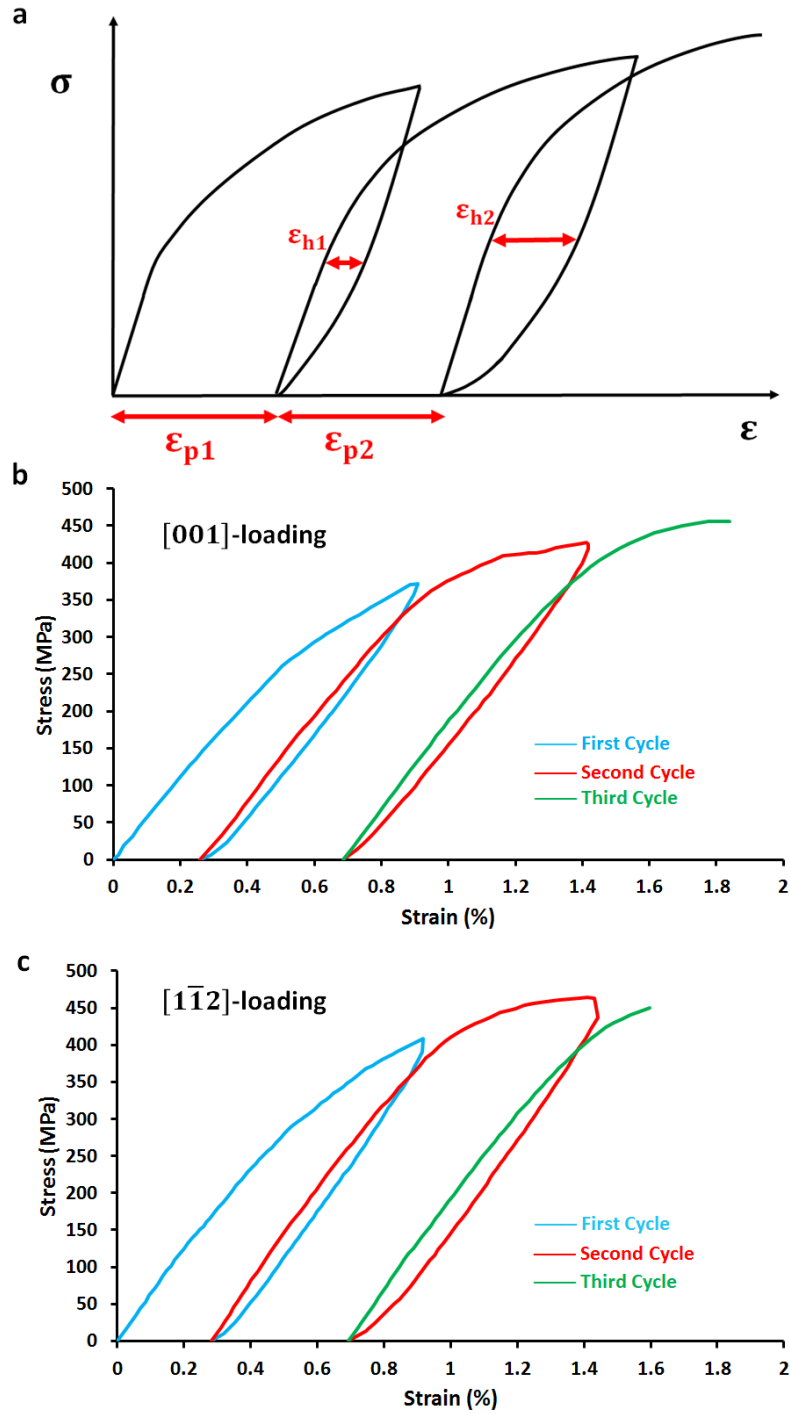
Figure 34: (a) Schematic of stress-strain response of the bicrystalline Al films during cyclic load-unload experiments. (b) Stress-strain response of the 180 nm thick Al film for loading along the $[001]_{G\_A}$ direction. (c) Stress-strain response of the same film for loading along the $[1\bar{1}2]_{G\_A}$ direction.

60
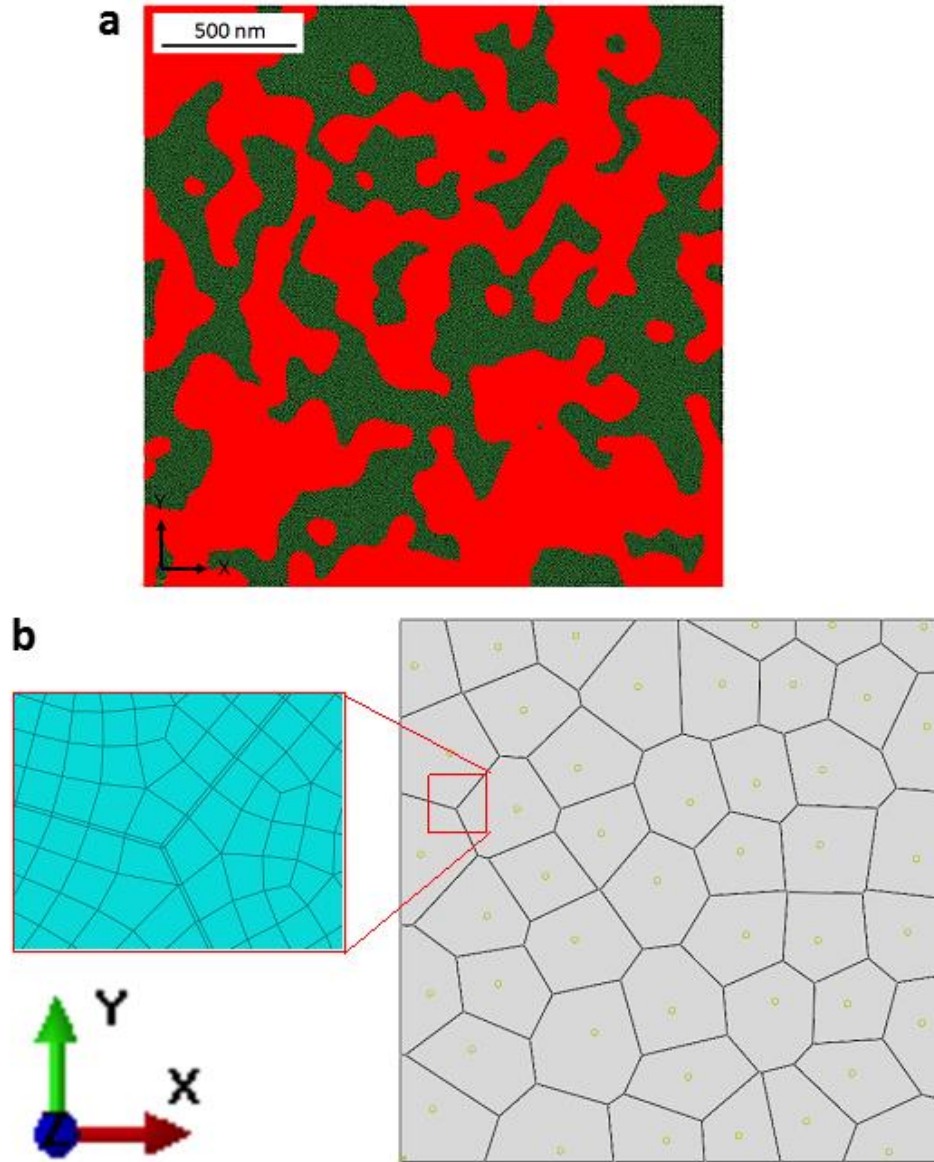
Figure 35: Plan views of the meshes used for the microstructurally explicit simulation (a) geometry obtained from ACOM-TEM data and AvizoFire™. The red region is grain variant A. (b) geometry obtained from a Voronoi tessellation including detail of the grain boundary region.

61

6.3 Results and Discussion

6.3.1 Experiments

Figure 33 shows the stress-strain response of the 240 nm Al film, loaded along $[001]_{G\_A}$ and $[1\bar{1}2]_{G\_A}$, respectively, at different strain rates. The data show an initial linear elastic region for both loading directions, where the curves at different strain rates are nearly identical. It is noted that the initial stress-strain slope for both the loading directions is less than the bulk Young's modulus of Al (E = 69 GPa) for reasons explained in (Izadi and Rajagopalan 2016).

As evident from Figure 33a the stress-strain curves of the 240 nm thick bicrystalline film loaded along $[001]_{G\_A}$ showed very little variation across different strain rates. All the curves showed a gradual elastic-plastic transition (microplastic regime) following the initial linear response and $\sigma_{0.8\%}$ increased only by 7% as the strain rate increased from $6.9\times10^{-6}\,\text{s}^{-1}$ to $5.3\times10^{-3}\,\text{s}^{-1}$. In contrast, when loaded along $[1\bar{1}2]_{G\_A}$ the same film exhibited a more perceptible strain rate effect (Figure 33b). Flow stress ($\sigma_{0.8\%}$) increased by 15% over a similar strain rate range. As a result, the strain rate sensitivity exponent ($m = dlog(\sigma)/dlog(\dot{\varepsilon})$) was ~24% lower for loading along $[001]_{G\_A}$ (m=0.016) compared to $[1\bar{1}2]_{G\_A}$ (m=0.021), as shown in Figure 33c. In addition, the stress required to induce macroscopic plasticity was higher for loading along $[1\bar{1}2]_{G\_A}$ compared to $[001]_{G\_A}$. Thus, for a given strain and strain rate, the stress was higher for loading along $[1\bar{1}2]_{G\_A}$ compared to $[001]_{G\_A}$.

The cyclic load-unload experiments along $[1\bar{1}2]_{G\_A}$ and $[001]_{G\_A}$ directions of the 180 nm thick film also revealed two notable differences in behavior (Figure 34). First, the deviation from elastic behavior during unloading was larger for the $[1\bar{1}2]_{G\_A}$ loading direction, leading to a larger hysteresis (ε_h, see Figure 34a) in the stress-strain response. While the normalized hysteresis strain ($\varepsilon_h/\varepsilon_p$) for $[1\bar{1}2]_{G\_A}$ loading was only slightly higher compared to $[001]_{G\_A}$ loading for the first cycle (Table 1), $\varepsilon_h/\varepsilon_p$ decreased significantly for $[001]_{G\_A}$ loading during the second cycle. As a result, $\varepsilon_h/\varepsilon_p$ for $[1\bar{1}2]_{G\_A}$ loading was more than 30% higher compared to $[001]_{G\_A}$ loading during the second cycle (Table 1).

Table 1: Hysteresis strain during the cyclic deformation of the 180 nm thick Al film along the two directions.

	$\varepsilon_{h1}(\%)$	$\varepsilon_{h2}\ (\%)$	$\dfrac{\varepsilon_{h1}}{\varepsilon_{p1}}$	$\dfrac{\varepsilon_{h2}}{\varepsilon_{p2}}$
$[001]_{G\_A}$ loading	0.0503	0.0616	0.1941	0.1441
$[1\bar{1}2]_{G\_A}$ loading	0.0559	0.0791	0.1977	0.1926

Second, the stress for a given strain was lower for the $[001]_{G\_A}$ loading direction compared to the $[1\bar{1}2]_{G\_A}$ loading direction during the first cycle (Figure 34b and Figure 34c). However, the residual hardening was higher for the $[001]_{G\_A}$ loading direction, which diminished the stress difference in the subsequent cycles. For instance, $\sigma_{0.8\%}$ was ~350 MPa for $[001]_{G\_A}$ loading during the first cycle, whereas it was ~380 MPa for $[1\bar{1}2]_{G\_A}$

loading, a difference of 30 MPa. By the third cycle, the difference in $\sigma_{0.8\%}$ reduced to 15

MPa (415 MPa for $[001]_{G\_A}$ loading, 430 MPa for $[1\bar{1}2]_{G\_A}$ loading).

For the sake of completeness, we include simulations of the deformation response

of the films using three-dimensional finite elements with a microstructurally explicit model

that includes a grain boundary region, along with crystal plasticity and anisotropic

elasticity. The simulations were performed by our collaborators, Prof. Pedro Peralta and

Saul Opie, and a manuscript combining the experimental and simulation results presented

in this chapter has been submitted for publication (Izadi, Opie, et al. 2017).
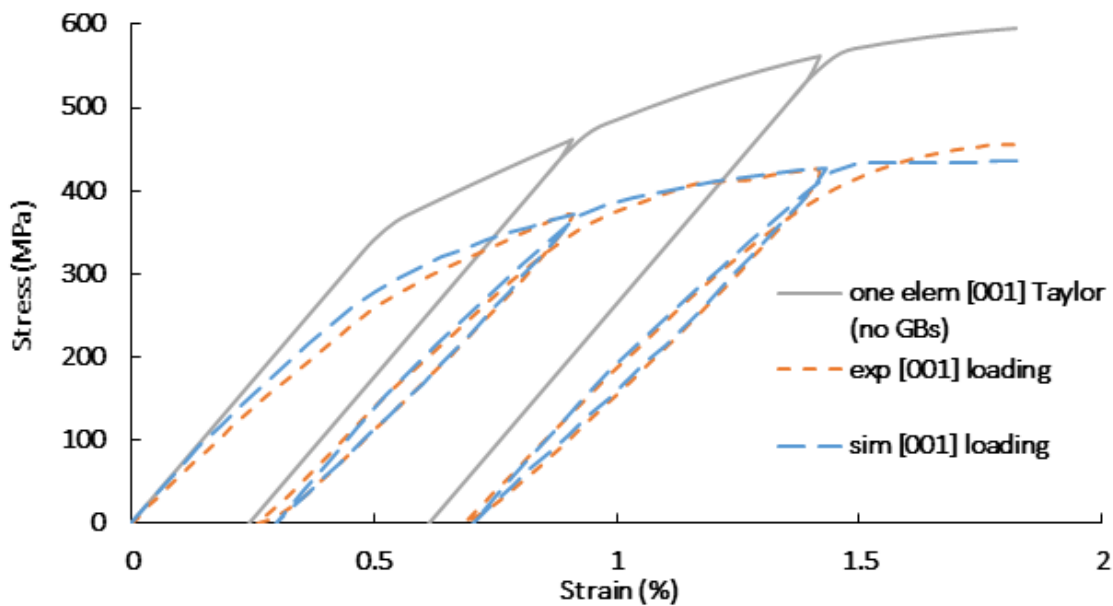
Figure 36: Comparison between experimental stress - strain curves and predictions (σ_{yy} vs ε_{yy}) from the Taylor and microstructurally explicit models for quasi-static cyclic loading along $[001]_{G\_A}$.

6.3.2 Simulations

6.3.2.1 Crystal plasticity model

The simple analysis based on the Schmid factor offered above assumes that the state of stress inside each variant is approximately uniaxial, which is likely to be a reasonable assumption for strains within the elastic regime, given the low elastic anisotropy of pure Al (Simmons and Wang 1971). However, within the plastic regime, plastic strain tensors produced by dislocation slip can change due to the effect of crystal orientation on slip geometry, potentially leading to different levels of interaction between the two grain variants for the two loading directions used. Therefore, several simulations were performed, first with a homogenized model based on polycrystalline plasticity via the Taylor model and then with microstructurally explicit models using the well-known strain hardening formulation described by Asaro in (Asaro 1983), and a non-linear kinematic hardening rule with linear dynamic recovery for each slip system, similar to that shown in (Goh, McDowell, and Neu 2006). Note that the crystal plasticity kinematics in this formulation allows for crystal rotation with plastic deformation (e.g., (Marin 2006)). Furthermore, the microstructurally explicit models were also augmented to account explicitly for the presence of a grain boundary region with higher plastic compliance compared to the bulk, i.e., a composite model, as described in (Mishnaevsky and Levashov 2015) and references therein. An elastic-perfectly plastic model was chosen for the grain boundary phase to keep the model as simple as possible. The simulations allowed us to quantify the states of stress and strain within each variant and the grain boundary region for both loading directions. Furthermore, the simulations helped us understand the

connections between plastic anisotropy and both local and global behavior during monotonic tensile experiments as well as cyclic load-unload experiments.

The calibration of material parameters for the simulation followed a sequential procedure where the simplest models were used first and then additional physics was incorporated if constraints from experimental results could not be met. In that regard, models were first calibrated to match the experimental data obtained from the quasi-static cycling loading experiments along the $[001]_{G\_A}$ direction. Key parameters from the experiments that were chosen to match with the simulations include the flow stresses before each unloading, the unloading slopes, the residual strains at zero load after each unloading and the loading-unloading hysteresis. A Taylor model with just crystal plasticity and kinematic hardening was first used to get initial values of the material parameters. Then microstructurally explicitly models were used, first without grain boundary regions and then with grain boundary phase added as needed. Those parameters were then used to predict the behavior for monotonic loading along $[001]_{G\_A}$ and $[1\bar{1}2]_{G\_A}$ and the simulation results were compared with the corresponding experimental data for validation. The microstructurally explicit simulations were then used to obtain volume averages of the stresses and strains within each variant, as well as global stress-strain curves for each loading orientation. Finally, shortcomings and potential ways to improve the model, as revealed by the loading-unloading behavior along $[1\bar{1}2]_{G\_A}$ direction, are discussed. The procedure to build the finite element models is described next.

66
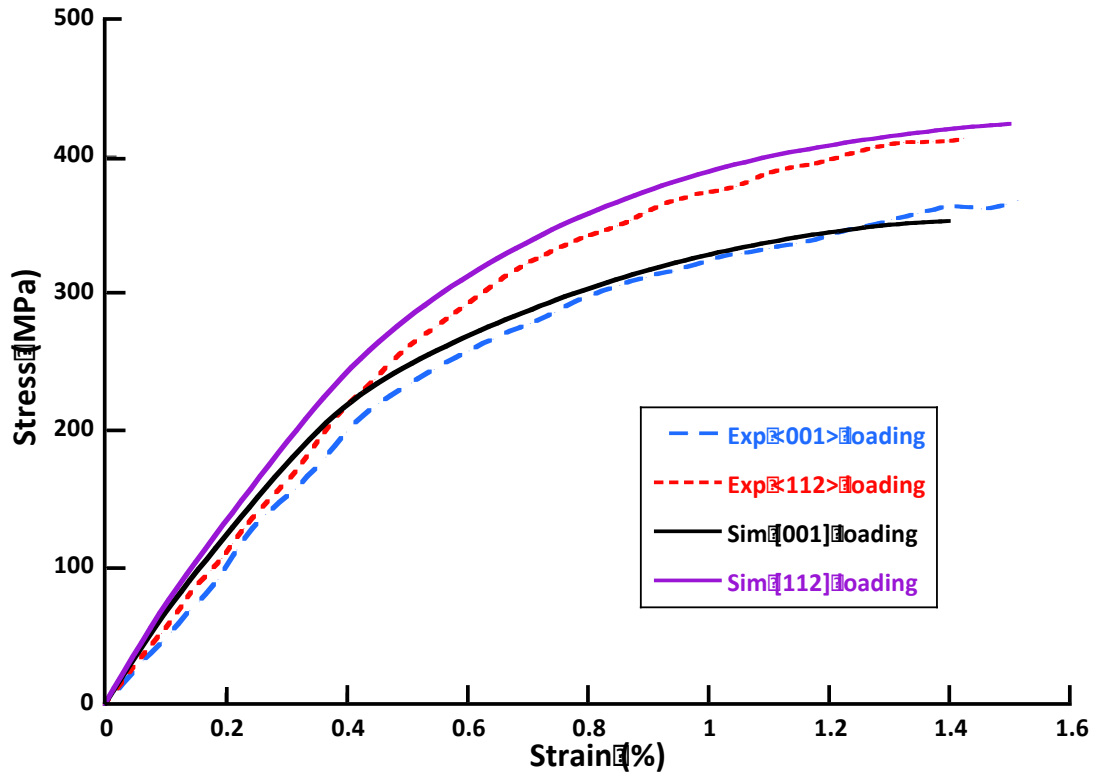
Figure 37: Comparison between experimental stress - strain curves under monotonic loading and predictions (σ_{yy} vs ε_{yy}) from the microstructurally explicit model for the two loading directions. The experimental data for $[001]_{G\_A}$ loading was obtained at a strain rate of 8.8×10^{-4} s^{-1}, and at 8.5×10^{-4} s^{-1} for $[1\bar{1}2]_{G\_A}$ loading.

6.3.2.2 Finite element models

All models were based on a 2000 nm x 2000 nm x 100 nm body, leading to a 20 to 1 aspect ratio (length to thickness and also width to thickness), that should produce the plane stress conditions along the thickness and plane strain conditions along the width that are expected in the actual samples. The mesh for the Taylor model consisted of 100 nm hexahedral elements. The microstructurally explicit model was created using either geometry obtained from the ACOM-TEM data or by using Voronoi tessellations with the same average grain size and grain orientations as that determined from ACOM-TEM data.

67

The tessellations were generated using the add-on tool for ABAQUS^{TM} described in (Stéphane and Stéphane 2011), while variants were assigned by hand following results from ACOM-TEM measurements.

The meshing process based on the ACOM-TEM data started from an inverse pole figure map similar to that shown in Figure 31d, which was used to recreate a three-dimensional columnar microstructure by extruding this geometry along the 100 nm (thickness) direction, with regions corresponding to each variant segmented and interpolated using AvizoFire^{TM} software. Then, a fine tetrahedral mesh was used to discretize the 3-D geometry and reproduce the smooth boundaries between the grains. The resulting mesh had ~585k elements, which was considered fine enough to ensure convergence of the numerical simulation. The procedure to create meshes from the Voronoi tessellation was similar, except that hexahedral elements were used for grain interiors. When the grain boundary phase was included, hexahedral elements were used for the boundary as well, except at triple junctions, where wedge elements were utilized. The thickness of the grain boundary layer was kept at about 1/200 of the grain diameter and this resulted in volume fractions of 50.93% for variant A, 47.94% for variant B and 1.13% for the grain boundary region. Examples of resulting models are shown in Figure 35.

All models were constrained to replicate pure tension, i.e., one face was constrained to stop motion along the loading direction (Y axis), and then either one node on that face was fully constrained, or a face normal to the X (or Z) axis was constrained to stop X (or Z) movement. The latter constraints were used due to the former introducing some minor twisting in the microstructurally explicit model due to anisotropy on the two variants. All out of plane constraints were such that the conditions of plane stress perpendicular to the

thickness of the films were maintained. All models were loaded along the Y direction, via an applied displacement on the face opposite to the one being constrained, at a strain rate of 10^{-3} s^{-1}, e.g., a ramp displacement up to a maximum value of 40 nm over 20 seconds, to a final total strain of about 2%, although most simulations were performed to lower total strains (~ 1.5%), while keeping the same strain rate. Appropriate histories based on the experiments were used for the quasi-static cyclic simulations. All models were analyzed with the implicit ABAQUS^{TM}/Standard solver using a user defined material subroutine (UMAT).

6.3.2.3 Crystal plasticity results

Material parameters were varied for both the Taylor and microstructurally explicit simulations. Equations (1) – (5) below, describe the basic flow rule and hardening laws implemented in the UMAT used here.

$$\dot{\gamma}^{\alpha} = \dot{\gamma}_0 \left| \frac{\tau_r^{\alpha} - \chi^{\alpha}}{\tau_c^{\alpha}} \right|^{\frac{1}{m}} sign(\tau_r^{\alpha} - \chi^{\alpha}) \tag{1}$$

$$\dot{\tau}_c^{\alpha} = \sum_{\beta=1}^{N} h_{\alpha\beta} |\dot{\gamma}^{\beta}| \tag{2}$$

$$h_{\alpha\alpha} = h(\gamma) = h_0 \operatorname{sech}\left(\frac{h_0 \gamma}{\tau_s - \tau_0}\right), \quad h_{\alpha\beta} = qh(\gamma) \, \alpha \neq \beta \tag{3}$$

$$\gamma = \sum_{\alpha=1}^{N} \int |\dot{\gamma}^{\alpha}| dt \tag{4}$$

$$\dot{\chi}^{\alpha} = k_1 \dot{\gamma}^{\alpha} - k_2 \chi^{\alpha} |\dot{\gamma}^{\alpha}| \tag{5}$$

where $\dot{\gamma}^{(\alpha)}$ is the plastic shear strain rate in slip system α, $\dot{\gamma}_0$ is a reference shear strain rate, t_r^a is the resolved shear stress for slip system α, c^a is the backstress on slip system α, t_c^a is the current critical resolved shear stress needed to produce dislocation motion in the slip system α (flow shear strength), m is the strain rate sensitivity, $\dot{\tau}_c^{\alpha}$ is the hardening rate for the shear strength in the slip system α, $h_{\alpha\beta}$ is the hardening matrix, h_0 is the initial hardening rate, t_0 is the initial shear yield strength, t_s is the stage I shear strength (Asaro 1983), q is the latent hardening ratio, $\dot{\chi}^{\alpha}$ is the rate of change of the backstress on slip system α, and k_1 and k_2 are constants.

The power-law used in equation (1) for the plastic shear strain rate is a very commonly used form (Asaro 1983) that tends to work fairly well, whereas equations (2) and (3) imply that hardening takes place due to both slip activity on a system and by slip activity on others, i.e., both self and latent hardening occur, which allows slip systems to harden at different rates.

As mentioned above, the results from the quasi-static cyclic loading experiments along $[001]_{G\_A}$ were used to start the calibration process for the material parameters, using a Taylor model, i.e., assuming the same total strain for each variant, along with the crystal plasticity model described in equations (1) through (5), without using a grain boundary phase. The Taylor simulations took less than a minute and provided an initial estimate of the single crystal parameters. It was noticed quickly that many of the parameters from the experimental curves that were selected for matching could not be replicated by pure kinematic hardening alone using the Taylor assumption.

A microstructurally explicit model was then used, and although it produced better matches than the Taylor model, it could not reproduce the loading-unloading hysteresis seen in the experiments. Finally, a grain boundary phase was introduced in the model that led to considerable improvement in the matching with the experimental data, including the hysteresis. Furthermore, through a systematic variation of the parameters it was found that lowering the values of k_1 and k_2 led to better agreement with the experiments. Given that the literature suggests that macroscopic kinematic hardening effects, including hysteresis, can arise due to interactions between phases/grains with different properties in both polycrystalline (Goh, McDowell, and Neu 2006) and NC materials [7], the kinematic hardening portion of the model was completely suppressed ($k_1 = k_2 = 0$), and the matching was done purely by changing the parameters used in equations (1) though (3) as well as the properties of the grain boundary phase.

Table 2: Material parameters used in simulations.

Crystal Plasticity	Value
Reference Slip Rate, $\dot{\gamma}_0^\alpha$ [1/s]	0.001
Strain Rate Sensitivity, m [-]	0.02
Initial Hardening Rate, h_0 [MPa]	8.0e3
Initial Critical Resolved Shear Stress, τ_0 [MPa]	150.0
Stage I shear strength, τ_s [MPa]	250.0
Latent hardening ratio, q	1.0
C11, [GPa]	108.2
C12, [GPa]	61.3
C44, [GPa]	28.5
Grain Boundary Region	
Sy [MPa]	70.0
Young's Modulus [GPa]	70.0
Poisson's ratio	0.35

Table 2 lists the parameters that led to the best match obtained with the microstructurally explicit model including a grain boundary phase. Note that the anisotropic elastic constants for the Al grains C11, C12 and C44 were obtained from the literature (Thomas 1968).

Figure 36 shows the results of the microstructurally explicit model (with self and latent hardening) that included a grain boundary phase and a one element Taylor model (no grain boundaries) without intrinsic backstress for comparison along with the experimental data. Both models used the same crystal plasticity material parameters for the bulk. As evident from the figure, the Taylor model did not provide a good match with the experiments and could not reproduce the loading-unloading hysteresis. The microstructurally explicit crystal plasticity model (with grain boundary phase) led to excellent quantitative agreement between the experimental data and the simulation results. This shows that the backstresses in this material are indeed the result of heterogeneity in properties of the grain interiors and grain boundaries, which rendered explicit incorporation of kinematic hardening models unnecessary.

The calibrated model resulting from the procedures described above needed to be validated against experimental data not used for the calibration process. In this case, the model was used to predict stress-strain curves obtained under monotonic loading with a known strain rate for the two loading directions. One issue with this approach is that the films used for the quasi-static cyclic loading experiments, which provided the calibration data, were thinner than those used for monotonic tensile testing, and it is a well-known fact that the yield strength of thin films depends on both film thickness and the grain size (Nix 1998; Freund and Nix 1996; Zhou and LeSar 2012). Given that both films had a similar

bicrystalline microstructure, a thickness correction needed to be applied before using the model on the thicker films. In particular, the yield strength of thin films has been shown to scale with the inverse of the film thickness (Nix 1998; Freund and Nix 1996; Zhou and LeSar 2012), so the values of t_0 and t_s were multiplied by $1/(240/180) = 0.75$, for the thicker samples. No other corrections were made. The model predictions for the stress-strain curves after these modifications are shown in Figure 37, along with the corresponding experimental data.

The simulations predict a higher stiffness at low values of stress and strain, which is related to elastic compliance issues associated with sample buckling (see [27]). However, the agreement improves considerably at higher loads, with good matching for the $[1\bar{1}2]_{G\_A}$ loading and excellent agreement for $[001]_{G\_A}$ loading, which is not unexpected given the data used for calibration.

The results from the microstructurally explicit model were used to examine the behavior of each variant. In this regard, volume averages of the stresses and strains in each of them were obtained from the numerical solution and then used to obtain stress-strain curves for each variant along the loading direction. The resulting stress-strain curves for loading along $[001]_{G\_A}$ is shown in Figure 38, along with contour plots of von Mises stress at 1.5% macroscopic strain. Note that the individual stress-strain curves in terms of the applied strain for the two variants are quite close, with the stress for variant B, which has a loading axis parallel to [110] in this case, being slightly higher. The von Mises stress exhibits some variability, with values approximately equal to the applied stress across grains from both variants (green contours at about 350 MPa), but also with values both lower and higher.
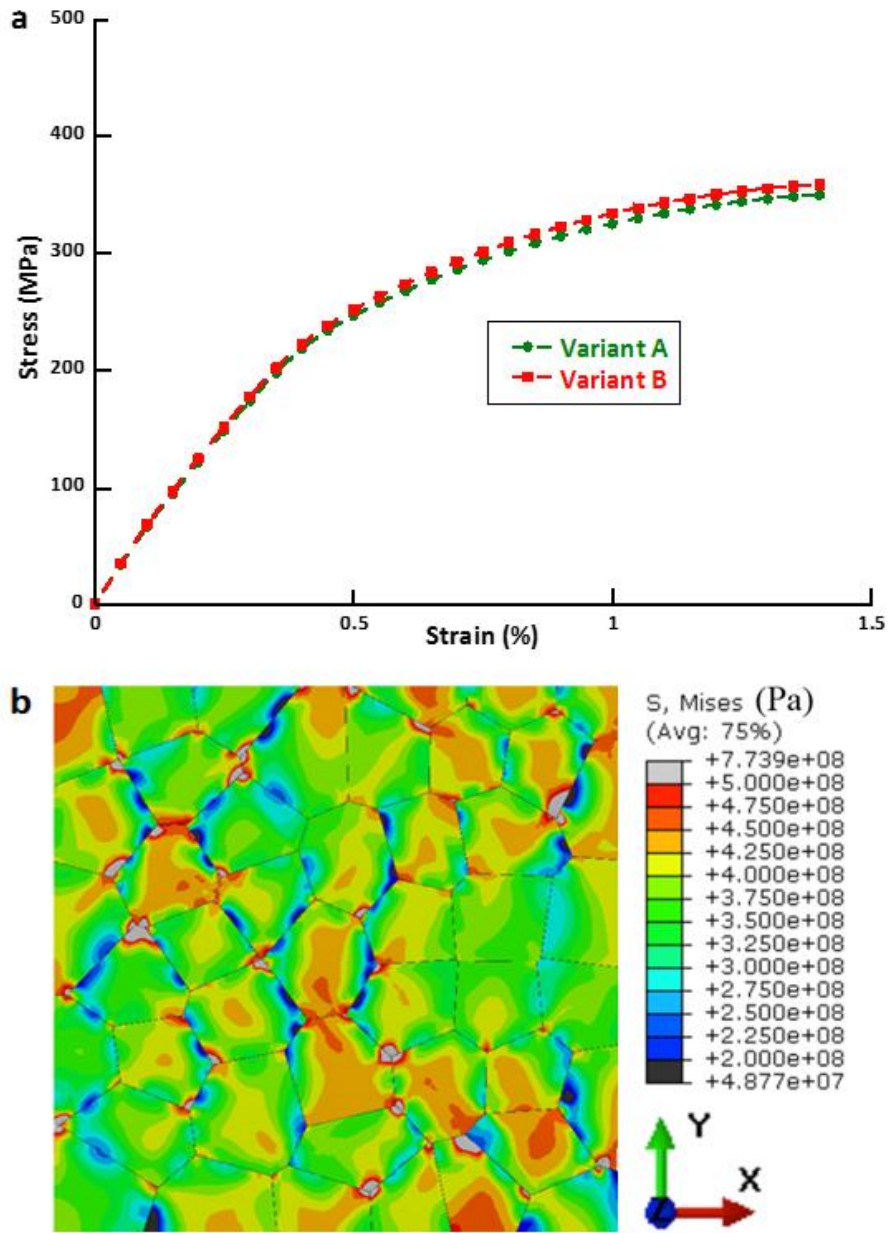
Figure 38: Local mechanical response from the simulation of monotonic loading along $[001]_{G\_A}$. (a) Volume averaged stress (σ_{yy}) in each variant versus macro strain (ε_{yy}). (b) von Mises stress distribution at 1.5% macro strain.
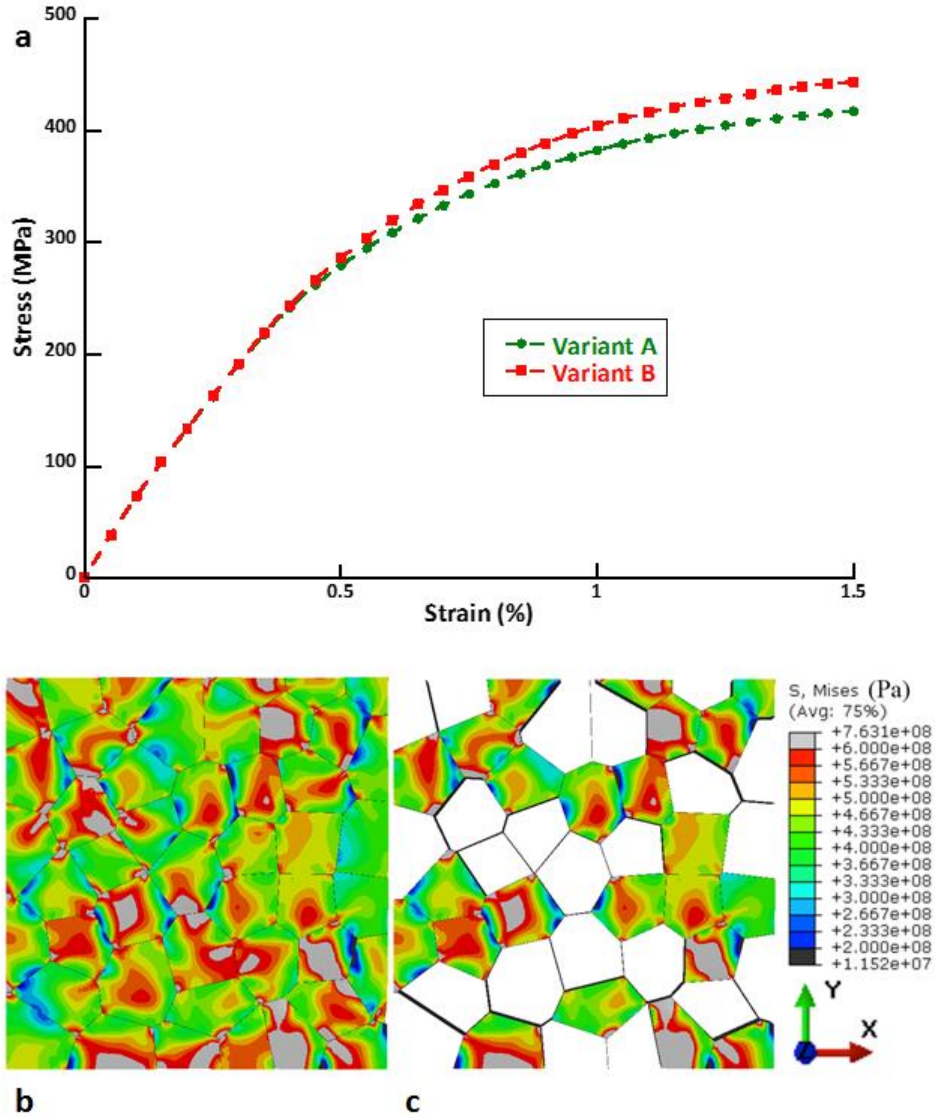
Figure 39: Local mechanical response from the simulation of monotonic loading along $[1\bar{1}2]_{G\_A}$. (a) Volume averaged stress (σ_{yy}) in each variant versus macro strain (ε_{yy}) (b) von Mises stress at 1.5% macro strain (c) von Mises stress in Variant B at 1.5% macro strain. The color bar applies to both (b) and (c).

Note that low values of von Mises stress occur always close to grain boundaries that are highly inclined with respect to the horizontal axis (x-axis, in this case), whereas high values of von Mises stress occur at triple junctions and also at several locations where grain boundaries are almost perpendicular to the loading axis (y-axis). The low values are

75

likely indication of local stress relaxation due to sliding along the softer grain boundaries, which helps maintain the average stresses in both variants about the same.

The results for loading along $[1\bar{1}2]_{G\_A}$ were different from those for loading along $[001]_{G\_A}$, as shown in Figure 39. The stress-strain curves obtained for the two variants (Figure 39a) showed that their responses to applied load had larger differences between one another and the macroscopic stress-strain response than for the $[100]_{G\_A}$ loading. Stress partitioning between the two variants for this case is illustrated in Figure 39b and Figure 39c, which show the von Mises stress distribution for a 1.5% macroscopic applied strain. Although the stress could be high in either variant, the stress in variant B was found to be higher more often than for variant A. Furthermore, note that the heterogeneity in the stress distribution is much more pronounced than for the $[001]_{G\_A}$ case.

The average strain response of each variant for the $[1\bar{1}2]_{G\_A}$ case, shown in Figure 40, indicates that, while strains in both variants are about the same up to a macroscopic strain of 0.2%, their response starts to differ above that value. The plot shows clearly that variant A carried a larger strain than variant B and the way the strain is portioned also indicates that the grain boundary region produces displacements along the load direction that are responsible for a meaningful fraction (~25%) of the macroscopic strain. Simulations suggest that these displacements are mostly due to shear at the grain boundary phase, in a way quite similar to grain boundary sliding. The stresses and strains at the grain boundaries also play a key role on the development of backstresses leading to loading-unloading hysteresis, as described next.

Normal stress along the loading direction in each variant and the grain boundaries as a function of macroscopic strain is shown in Figure 41 for both loading directions. The plots show trends that agree with those obtained from monotonic loading simulations in terms of how stresses are distributed among variants, i.e., variant B taking more stress than variant A, in both cases, with results for loading along $[001]_{G\_A}$ (Figure 41a) being a lot more homogenous than for loading along $[1\bar{1}2]_{G\_A}$. The plots show that the grain boundary phase plays a key role on the development of hysteresis during loading-unloading of the samples for both loading directions, as the hysteresis for the grain boundary phase is much more pronounced than for the individual variants. Furthermore, note that the normal stress in the grain boundary phase becomes negative while the stresses in the variants are still positive. The value of the compressive stress actually increases in absolute value with strain, which means larger backstresses. This, in turn, correlates well with an increase in the hysteresis strain ε_h.

In the bicrystalline Al films explored here, the initial stage of deformation is relatively homogeneous because elastic moduli for grain variants A and B along both loading directions are quite similar. The elastic modulus of variant A is 63.7 GPa and variant B is 72.5 GPa for loading along $[001]_{G\_A}$. The corresponding values for $[1\bar{1}2]_{G\_A}$ loading are 71.8 GPa and 75.6 GPa, respectively. Thus, the elastic strain mismatch between the grains is small regardless of the loading direction. However, the plastic behavior is significantly different for the two loading directions.
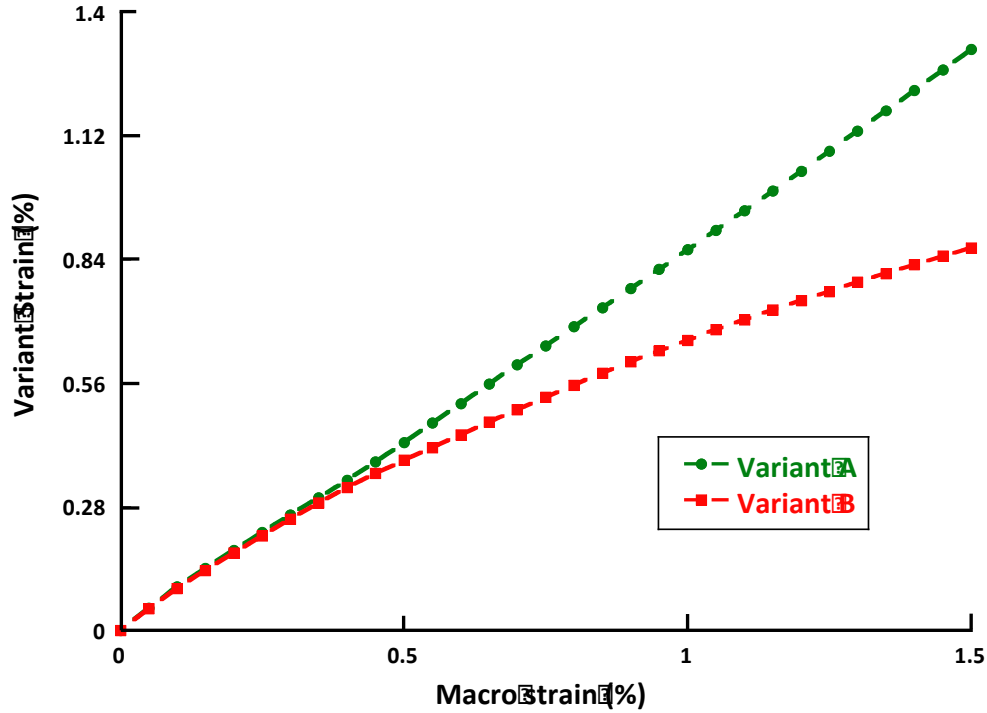
Figure 40: Volume average of variant strain (ε_{yy}^{var}) vs. macro strain (ε_{yy}) from simulations of monotonic loading along the $[1\bar{1}2]_{G\_A}$ direction.

For the $[001]_{G\_A}$ loading direction, heterogeneity in the plastic response due to anisotropy is very small and the local response remains relatively homogeneous even after the film starts to deform plastically, as corroborated by the simulations results shown in Figure 38. The small differences in stiffness between the two variants for loading along $[001]_{G\_A}$ actually correlate with the slightly higher stress in variant B revealed by the simulations (Figure 38a). In contrast, for $[1\bar{1}2]_{G\_A}$ loading, heterogeneity in the plastic response is higher as discussed in section 6.2. As a result, there is considerable plastic strain mismatch between adjoining grains, as shown in Figure 40, and the grains need to rotate with respect to each other to maintain strain compatibility. Such grain rotations have been

78

shown to be time dependent (Izadi, Darbal, et al. 2017; Izadi and Rajagopalan 2016), which leads to a higher strain rate sensitivity for loading along $[1\bar{1}2]_{G\_A}$ direction.

The strain and stress partitioning is likely a key component of the phenomenon discussed above. In this regard, it is interesting that the strain in each variant predicted by the simulations can be explained by a simple weighted average based on the Schmid factors. At 1.5% applied strain for loading along $[1\bar{1}2]_{G\_A}$, the strain carried by variant A is about 1.32% and for variant B it is 0.867%, which leads to $e_{yy}^{A}/e_{yy}^{B}=1.32/0.867 = 1.52$. Note that this is nearly identical to the ratio of the Schmid factors for these two variants (0.408/0.272 = 1.5.). The presence of curvature in these plots shows that the behavior changes as a function of applied strain. Specifically, the ratio of the strains in the two variants starts at less than 1.5 (close to 1 till ~0.2% strain and ~1.22 at 0.75% strain), which should be expected due to the presence of the more compliant grain boundary phase that leads to gradual development of strain and stress partitioning between the variants. Nonetheless, the ratio becomes closer to 1.5 for larger strains, which suggests that as plastic strain increases the Schmid factors control the behavior more closely, at least for the range of strains used in the simulations.

The curvature can be explained by the increased hardening in Variant B due to multiple slip along its [111] loading axis, and its higher rate of hardening compared to Variant A, which starts with symmetric double slip. The behavior beyond the 1.5% strain used in the simulations is likely to depend strongly on hardening behavior. If additional curvature develops as a result of further increases in hardening rate in variant B, then the

ratio of the strains carried by the two variants can exceed 1.5, i.e., Variant B carries even less strain. However, if the hardening saturates and the hardening rate becomes low for both variants, then the ratio of their strains is likely to stay the same. The overall stress-strain behavior shown in Figure 37 suggests that the hardening rate is approaching saturation as the slope of the curves is reaching low values at 1.5% strain.

The way the strain partitions indicates that neither the Taylor (isostrain) or Sachs (isostress) (Kocks 1970) assumptions apply in this case, so the variants are in a "compliant" loading state. Nonetheless, the strain portioning seems to be controlled by the Schmid factor, as pointed out above. Further simulations will be conducted to study these effects in more detail. It is also worth pointing out that the partitioning of strain *between* the grain variants (families) in our UFG Al films, as revealed by the simulations, is in stark contrast to the behavior of NC metals. In NC metals, stress/strain redistribution occurs primarily within grain families at small plastic strains (<2%) due to the presence of plastically "soft" and "hard" grains (Li et al. 2012). Capturing these stress redistributions in NC metals requires the use of quantized crystal plasticity models, where a wide, asymmetric distribution of critical resolved shear stresses is assumed for the grains (Li et al. 2012; Lin Li 2009).

The hysteresis in the stress-strain response of the bicrystalline films (Figure 34b and Figure 34c) is essentially a consequence of the inelastic stress-strain response during unloading, sometimes referred to as the early Bauschinger effect (BE). BE in UFG metals has been attributed to inhomogeneous stress distribution caused by microstructural heterogeneity (Rajagopalan and Saif 2011), which leads to reverse yielding of plastically

soft grains during unloading (Rajagopalan, Han, and Saif 2008). While there are many possible sources of heterogeneity, the distribution in size and orientation of grains is particularly important. The effect of grain size distribution manifests as a variation in yield strength (critical resolved shear stress) of different grains, whereas the orientation dictates the resolved shear stress acting on the grains through the Schmid factor for each variant. In simulations used in this work, a grain boundary region was used and found to be key to model the stress-strain response, particularly given that the almost bicontinuous distribution of the two variants (see Figure 31) makes it hard to quantify what the grain size variability really is for the samples tested here. However, note that the effects of the grain boundary region and local grain size are likely correlated, since smaller grains will have a larger fraction of grain boundary region. For the bicrystalline Al films explored in this study, loading along $[001]_{G\_A}$ minimizes the variation of the resolved shear stress (low plastic heterogeneity). As a result, the stress-strain hysteresis observed for $[001]_{G\_A}$ loading is likely to result mainly from the grain size and grain boundary effects. In contrast, for $[1\bar{1}2]_{G\_A}$ loading both the grain size variation and heterogeneity in plastic behavior due to anisotropy are likely contribute to the hysteresis. In particular, note that for cyclic loading along $[1\bar{1}2]_{G\_A}$ (Figure 41b) not only the stresses for the grain boundary phase become negative when unloading is complete, but also the stresses in variant B do so, which does not occur for loading along the $[001]_{G\_A}$. This is clear evidence that additional backstresses develop in this case, which strongly suggests that the difference in hysteresis between the two loading directions is also directly affected by the heterogeneity in the plastic behavior induced by anisotropy.

It is important to point that despite the useful insights provided by the model used here, it still had some limitations while trying to match quantitatively the quasi-static cyclic behavior for loading along $[1\bar{1}2]_{G\_A}$. In particular, the model overpredicted the overall flow stress measured during the experiment, by a slightly larger margin than that for the monotonic case shown in Figure 37, and also underestimated the values of the hysteresis strain ε_h as a function of applied strain. Some preliminary modifications to the model indicate that a higher compliance of the grain boundary region for loading along $[1\bar{1}2]_{G\_A}$. would correct for some of these effects. This suggests, given the good match obtained from loading along along $[001]_{G\_A}$, that the properties of the grain boundary region are likely to be anisotropic as well, as they need to change with loading direction. Furthermore, and perhaps more importantly, there are likely additional deformation mechanisms with higher strain rate sensitivity than those suggested by values of m shown in Figure 33c. In particular, note from Figure 34c that the unloading locations for the data obtained along $[1\bar{1}2]_{G\_A}$ show evidence of stress relaxation behavior (actuator displacement was held constant for 1-2 minutes before unloading began). The presence of viscoplasticity can introduce additional strains that can lead to increased compliance. The use of a viscoplastic model for the grain boundary region, as suggested in (Mishnaevsky and Levashov 2015) and references therein is a way to take this into account and likely to produce an even better quantitative matching of the observed behavior. This work is currently underway and will be reported elsewhere.
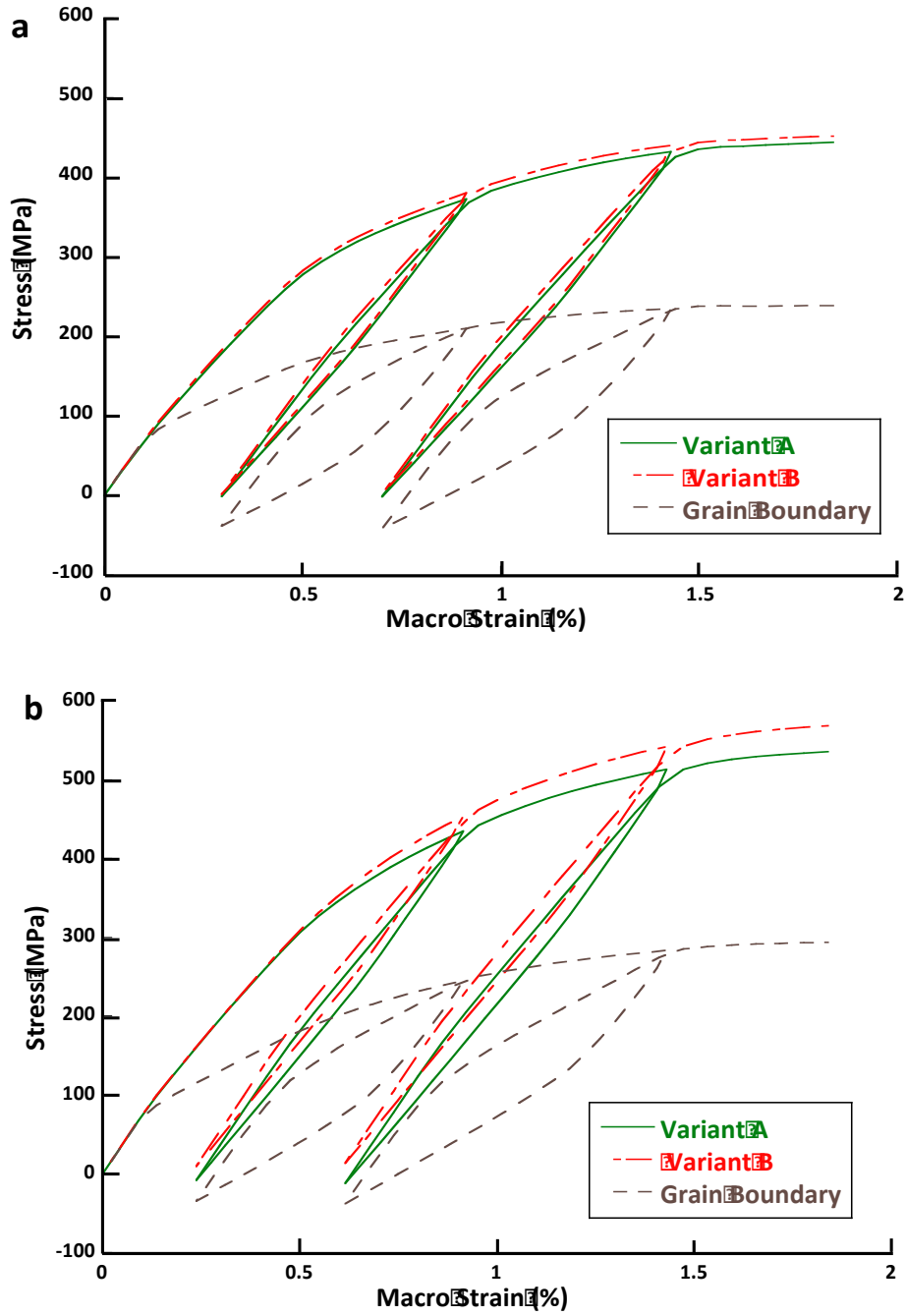
Figure 41:Volume average of variant (σ_{yy}^{var}) and grain boundary (σ_{yy}^{GB}) stresses vs. macro strain (ε_{yy}) from simulations of quasi-static cyclic loading parallel to (a) the [001] direction in Variant A and (b) the [1$\bar{1}$2] direction in Variant A.

83

As discussed in section 6.3.1, both the stress-strain response during the first loading and the residual strain hardening in the subsequent cycles was dependent on the loading direction. Since the $[001]_{G\_A}$ loading leads to a relatively high Schmid factor in all the grains, yielding occurs earlier compared to the $[1\bar{1}2]_{G\_A}$ loading direction and the stresses are lower. However, because many slip systems are simultaneously activated, there is a higher probability of dislocation entanglements. As a result, there is significant residual hardening in the subsequent cycles. Qualitative post-mortem TEM observations indeed reveal significant residual dislocation networks as shown in Figure 42a. The opposite case applies for the $[1\bar{1}2]_{G\_A}$ loading. The yield stress during the first cycle is high because of the low Schmid factor ($s = 0.272$) of one of the grain variants. But because only two slip systems are activated in the plastically soft grain variant ($s = 0.408$), dislocation entanglements are less likely (Figure 42b) and lead to smaller residual hardening. This also justifies the choice of hardening law for the crystal plasticity modeling of grain interiors, as Asaro's model is indeed based on the assumption that dislocations can be stored and interact to produce hardening.

6.4 Conclusions

In this study, we have explored the effect of plastic anisotropy on the deformation behavior of UFG aluminum films with a bicrystalline texture. By systematically choosing two loading directions that minimized/maximized the heterogeneity due to texture-induced plastic anisotropy, we have shown that plastic anisotropy influences the flow stress, strain rate sensitivity, Bauschinger effect and residual hardening of UFG films. Thus, these results strongly imply that apart from the mean grain size and distribution, crystallographic

texture needs to be taken into account for understanding and predicting the deformation behavior of UFG metals. In addition, using microstructurally explicit finite element simulations based on crystal plasticity we have shown that strain portioning in the grains follows the Schmid rule and neither isostress nor isostrain assumptions hold for the deformation of these films. The good correspondence between the simulations and experiments of the overall stress-strain behavior also indicates that conventional crystal plasticity, used in a composite model with a grain boundary phase to model the compliance of the interfaces, is adequate to describe the behavior of UFG metals. This observation contrasts with NC metals, for which quantized crystal plasticity models (Li et al. 2012; Li, Lee, and Anderson 2010) that incorporate discrete strain bursts and a distribution of grain-level yield stresses are required to replicate the stress-strain response.
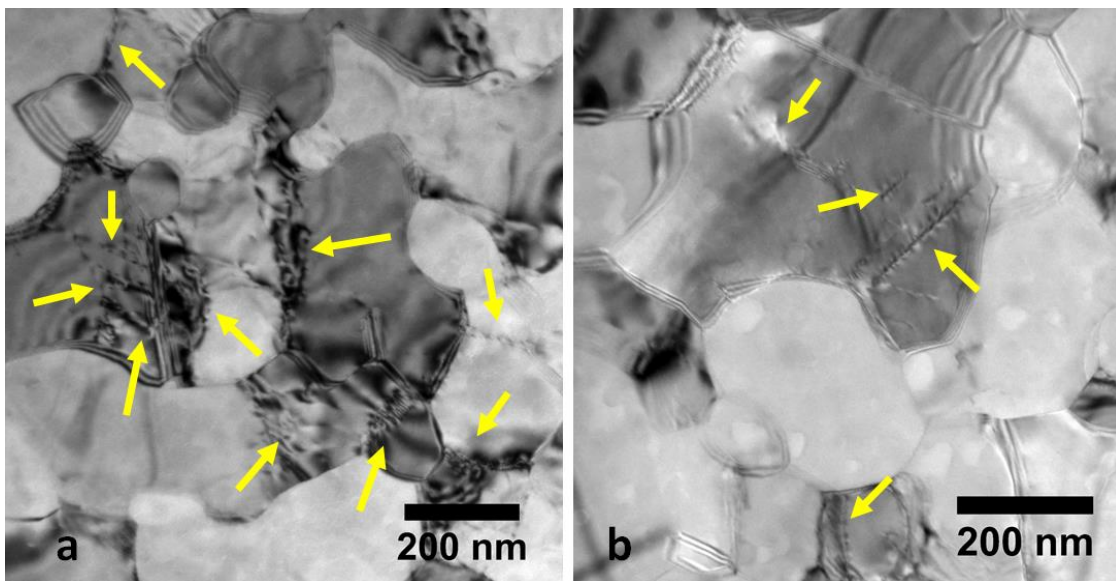
Figure 42: (a) Bright-field TEM image of numerous dislocation entanglements, indicated by yellow arrows, in the 180 nm film after loading along $[001]_{G\_A}$ direction. (b) Bright-field TEM image of dislocation entanglements in the 180 nm film after loading along $[1\bar{1}2]_{G\_A}$ direction. Fewer dislocation entanglements were seen in this case. Both samples were deformed to the same strain (~0.9%).

CHAPTER 7

GRAIN ROTATIONS IN ULTRAFINE-GRAINED BICRYSTALLINE ALUMINUM FILMS STUDIED USING IN-SITU TEM STRAINING WITH AUTOMATED CRYSTAL ORIENTATION MAPPING

7.1 Introduction

In chapter 6, we showed that the bicrystalline Al film (with a relatively more homogeneous microstructure than the non-textured film) showed characteristics of mechanical behavior similar to the non-textured film when loaded along $[1\bar{1}2]_{G\_A}$ direction. The more heterogeneous deformation of this film along $[1\bar{1}2]_{G\_A}$ direction led to higher strain rate sensitivity of flow stress and more significant Bauschinger effect than the $[001]_{G\_A}$ loading direction.

Therefore, the main objective of the study in this chapter is to address the following question: "Does bicrystalline Al film show similar grain rotations to the non-textured film during loading and unloading?". To answer this question, we used in-situ tensile straining with ACOM-TEM to monitor the changes in grain orientations during tensile load-unload deformation and to obtain quantitative information about the magnitude and nature of such rotations.

7.2 Materials and Experimental Procedure

A 180 nm bicrystalline Al film was deposited on (001) silicon wafer after the native silicon dioxide layer etched with hydroflouric acid, as explained in chapter 3. A statistical

analysis of bright field images of the Al film, obtained using a JEOL 2010F TEM, revealed a mean grain size of 220 nm (Figure 43).

Freestanding samples of the film were co-fabricated with a MEMS devices of design II (explained in chapter 2 - Figure 8). The MEMS devices allowed loading of the bicrystalline film along the $[1\bar{1}2]$ direction of the one of the grain variants (similar to the $[1\bar{1}2]_{G\_A}$ direction, explained in chapter 4). The macroscopic stress and strain on these films were measured with the uncertainties of less than 10 MPa and less than 0.003%, respectively, as explained in sections 2.3 and 3.2.
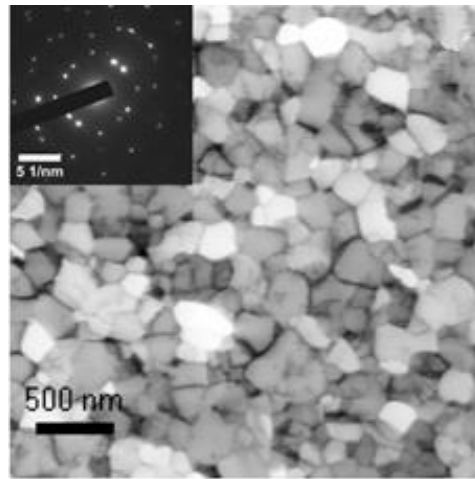
Figure 43: Bright-field TEM image of the 180 nm thick, bicrystalline Al film with a mean grain size of 220 nm. Selected area diffraction (SAD) of the film showing an (110) out-of-plane texture with two in-plane variants rotated 90° with respect to each other (inset).

A procedure identical to the in-situ TEM-ACOM straining of the non-textured Al film discussed in chapter 4 was followed and the mechanical behavior of the bicrystalline film was investigated through in-situ TEM-ACOM, quasi-static tensile load-unload experiments. The data was collected from the same $3~\mu m \times 3~\mu m$ area at three strain levels during loading and two strain levels during unloading with a step size of 10 nm.

While the ACOM maps provided information of the Euler angles of 300 grains in the scanned area of the film, only 225 grains, with a reliability index greater than 15 and a low spread in the point-to-point orientation (standard deviation > 0.1°), were considered for grain orientation analysis. For the remaining 225 grains, mean grain orientations that was calculated by averaging the orientations of all the points within a grain was used for all further analysis.

7.3 Results and Discussion

Figure 44a shows the stress-strain response of the 180 nm bicrystalline films during the in-situ TEM experiment. As indicated on the stress-strain curve, the orientation maps were obtained at 0.4%, 1.1% and 1.6% strain during loading (from here on referred to as 0.4% L, 1.1% L and 1.6% L), and at 1.5% and 1.2% strain during unloading (from here on referred to as 1.5% UL and 1.2% UL) of the film.

Using the mean orientation of each grain at different loading and unloading points, an analysis similar to that described in section 4.2 was performed to investigate their orientation changes. Taking the initial loading configuration (0.4%L) as the reference for the calculation, the total rotation of each grain (θ_i) about an arbitrary axis was quantified using Euler rotation theorem.
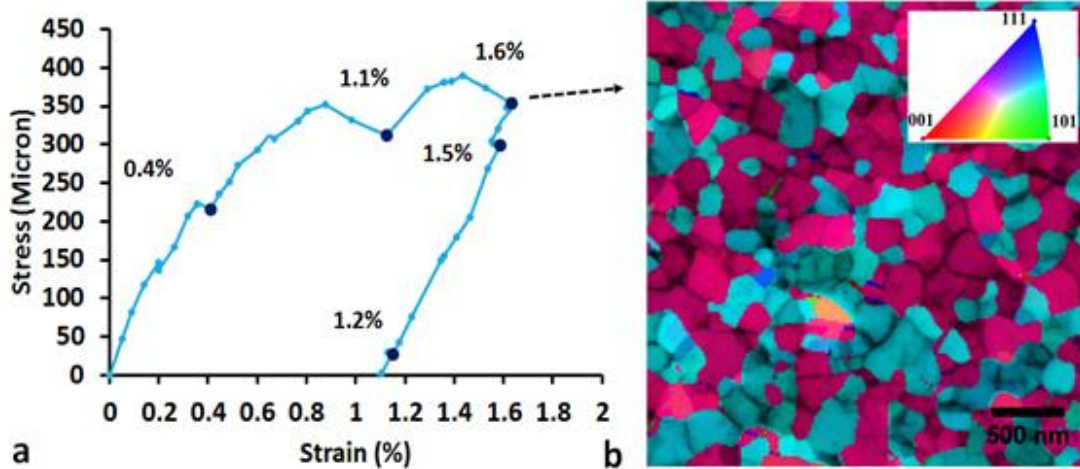
Figure 44: a) Stress-strain response of the 180 nm bicrystalline Al film during in-situ ACOM-TEM experiment. The orientation maps were acquired at three points during loading (0.4%, 1.1% and 1.6% strain) and two points during unloading (1.5% and 1.2% strain). b) An ACOM- map showing the color-coded out of plane orientation of the grains in the scanning area.

Figure 45 provides a histogram of grain orientation changes that occurred during loading and unloading of the bicrystalline film. As evident from the figure, the number of grains experiencing rotations increased from 152 to 171 as strain was increased from 1.1% to 1.6% during loading. In addition, the average θ_{avg}^{all} (including grains that did not undergo any rotation) was about 1.0° when the strain was increased from 0.4% to 1.1% and it increased to 1.2° when the strain was increased to 1.6%. A large fraction of grains experienced grain rotation during loading and unloading. However, compared to non-textured Al film (as shown in section 4.2), fewer grains started to experience rotations from the second loading configuration and the magnitude of the averaged total grain rotation (θ_{avg}^{all}) was also much smaller during loading and unloading of the bicrystalline Al film. The θ_{avg}^{all} was increased only by 0.2° during loading (from 1.0° to 1.2°) whereas it did not change during unloading (1.2°).

89
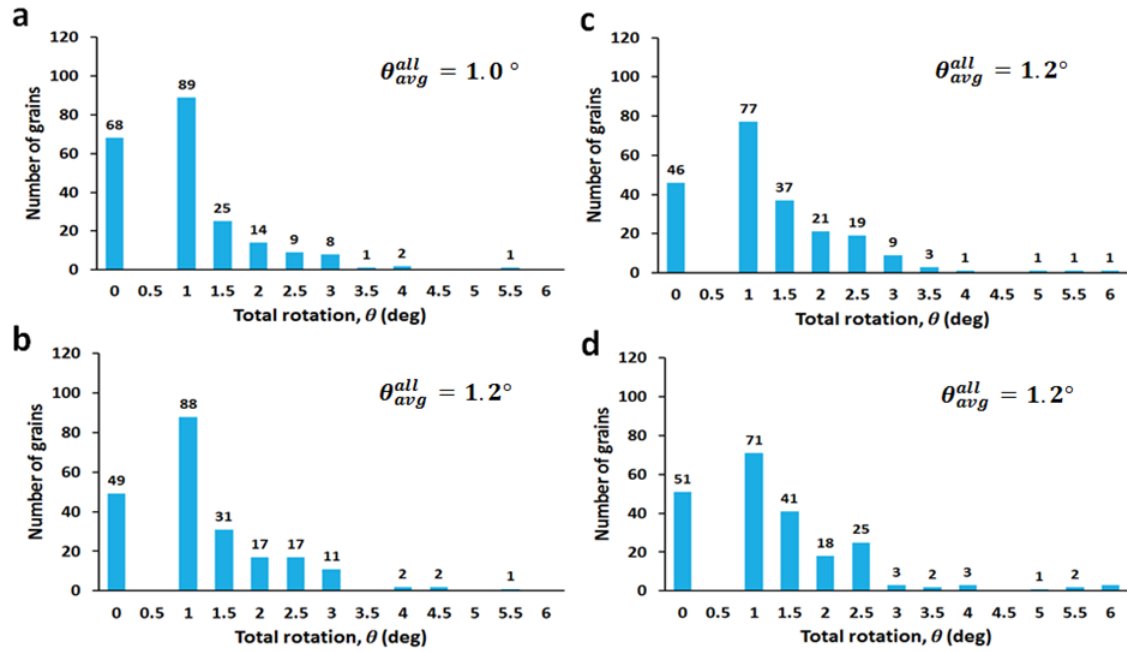
Figure 45: Histogram of the total rotation induced in approximately 220 grains during loading of the bicrystalline film from a) 0.4% strain to 1.1% strain and b) 0.4% strain to 1.6% strain. Histogram of grain rotations at the two unloading points, c) 1.5% strain and d) 1.2% strain. Note that the grain rotations for the unloading points are also calculated with respect to reference configuration at 0.4% strain during loading.

The initial deformation of the bicrystalline film is relatively more homogeneous than the non-textured Al film for which heterogeneous deformation led to high strain rate sensitivity and a large Bauschinger effect (as discussed extensively in chapters 3,4 and 5). This is because the difference in elastic modulus for the two grain variants along their loading directions (<112> and <111>) is quite small (71.8 GPa and 75.6 GPa, respectively). Additionally, the two grain variants in the film have a lower range of Schmid factors (s_1=0.408 and s_2=0.272) compared to grains in a non-textured film, where s can vary from 0.27 to 0.5. Therefore, the resultant plastic strain mismatch between the grains is smaller, which reduces the need for grain rotation to accommodate the deformation.

The results from ACOM-TEM experiment are consistent with the above arguments. As shown in Figure 45, the results of ACOM-TEM experiment revealed less pervasive grain rotation during loading of bicrystalline film than the non-textured Al film. More importantly, the amount of rotations did not change significantly during unloading and, in fact, the averaged total rotation of all the grains was constant at 1.6%L, 1.5%UL and 1.2%UL ($\theta_{avg}^{all} = 1.2°$). It is worth noting that, despite presence of only two grain variants in bicrystalline films, each variant consists of numerous grains with small misorientations. As loading continues, the grains of each variant are expected to bend/rotate in a manner that leads to the decrease of misorientation between them. Figure 46 shows an example of two grains whose misorientation continually decreased during loading and unloading (from ~1.2° at 0.4%L to ~0.5° at 1.2%UL). Consistent with this argument, the standard deviation (SD) of the in-plane misorientation (about the axis parallel to electron beam direction) between the grains of the same variant at each loading and unloading configuration decreases with deformation (Table 3). This suggests that elimination of low angle grain boundaries could be driving these rotations during loading and explains the less significant rotations of the grains during unloading.

Table 3: Standard deviation of the in-plane misorientation between the grains of the same variant at different loading and unloading configuration.

	0.4%L	1.1%L	1.6%L	1.5%UL	1.2%UL
Grains of the first variant	1.29	1.19	1.12	1.11	1.09
Grains of the second variant	1.57	1.47	1.44	1.40	1.33
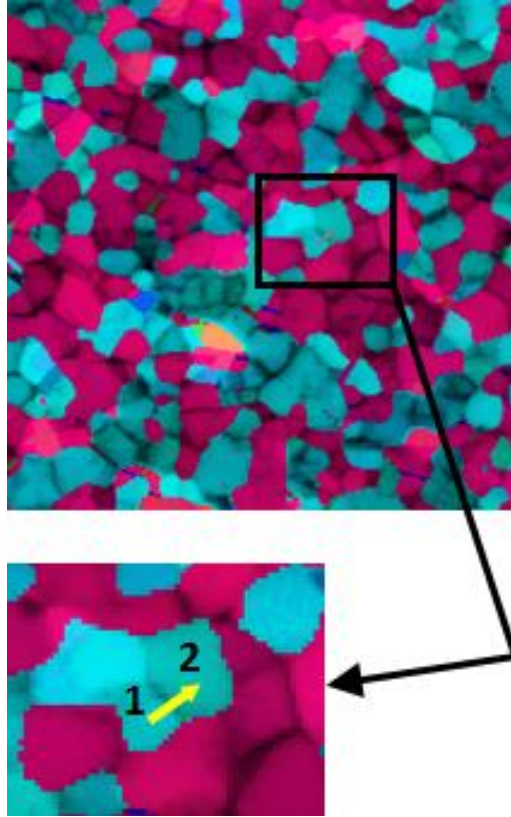
Figure 46: Two grains whose misorientation progressively decreased during loading and unloading of the bicrystalline film. The misorientation was measured across the grain boundary shown by the yellow arrow.

7.4 Conclusions

The relatively homogenous deformation behavior of bicrystalline UFG aluminum film was studied using in-situ ACOM-TEM load-unload experiments. An analysis of the ACOM data revealed grain orientation changes occurred during deformation of this film. However, unlike the non-textured Al film (discussed in chapter 4), the bicrystalline film exhibited less pervasive grain rotations during loading and no change in the averaged grain rotation during unloading. Furthermore, grain rotations in the bicrystalline film were accompanied by a reduction in misorientation between grains of the same variants, which suggests that elimination of low angle grain boundaries could be driving these rotations

during loading, leading to more homogenous deformation during unloading. These observations accordingly provide a possible explanation for the lower strain rate sensitivity of the film during loading and insignificant Bauschinger effect during unloading.

CHAPTER 8

CONCLUSIONS

8.1 Summary of Research Findings

The major objective of this study was to explore the mechanical behavior and the underlying deformation mechanisms of the ultrafine-grained thin films with different textures and under different loading conditions. Towards this end, macroscopic uniaxial tension experiments and in-situ TEM investigations were performed on Al thin films, the results of which were presented in the previous chapters. Here, we summarize the findings from this study before identifying some of the unresolved questions and making recommendations for future work.

The major findings derived from this study are:

1- Texture in metal thin films can significantly influence their mechanical behavior: Ultrafine-grained non-textured Al films show a larger Bauschinger effect during unloading than the bicrystalline film of similar thickness and grain size. In contrast to UFG bicrystalline film, non-textured Al films show a high strain rate sensitivity of flow stress and Bauschinger effect.

2- Changing the loading direction can lead to significantly different mechanical behavior of metal thin films due to change in the effect of plastic anisotropy: Ultrafine-grained bicrystalline Aluminum films show higher strain rate sensitivity of flow stress along the loading direction that maximizes the plastic anisotropy than the loading direction which minimizes it.

Ultrafine-grained bicrystalline Aluminum films show lower Bauschinger effect and higher residual strain hardening during cyclic load-unload experiments along the loading direction which maximizes the plastic anisotropy than the loading direction which minimizes it.

3- The differences in mechanical response of the Al thin films observed in this study was linked to the heterogeneity of deformation. Deformation heterogeneity lead to inhomogeneous stress distribution in the grains during loading and unloading of the film. To maintain strain compatibility, grains need to rotate with respect to each other. Strain rate sensitive mechanical response and Bauschinger effect in these films can be explained by these time dependent grain rotations.

4- Different type of grain rotations (forward, reverse and uncorrelated rotations) was identified during unloading of the non-textured Al film which was consistent with the nature of microstructural changes observed during deformation. The rotations and the microstructural observations point to a spatially inhomogeneous stress distribution in the film that constantly evolves during both loading and unloading.

8.2 Future Work

Although this dissertation has made contributions to the understanding of mechanical behavior of thin films and their underlying deformation mechanisms, there are many areas that still need to be explored. The future work can be broadly divided into the following areas.

8.2.1 Investigating Deformation of the UFG Bicrystalline Al Films along Different Loading Directions Using In-situ ACOM-TEM Technique

The deformation behavior of bicrystalline UFG Al films needs to be studied using the in-situ ACOM-TEM techniques. As discussed in chapter 4 and 6, the deformation behavior of the bicrystalline films is significantly different from the non-textured films. For example, fewer number of grains were observed to exhibit grain rotation in bicrystalline films compared to non-textured films. Additionally, it was observed that the mechanical response of the bicrystalline film is significantly varying with different loading directions. Therefore, carrying out in-situ ACOM-TEM cyclic load-unload experiments on bicrystalline films, loaded along the directions described to chapter 5, will enable us to perform a systematic investigation on grain rotation in these films and monitor the evolution of their microstructural changes during load-unload experiments. A comparative analysis on the observations of the in-situ ACOM-TEM experiments of the bicrystalline and the non-textured film, which was described in section 4.3.2, will lead us to a comprehensive picture of the effect of film texture and plastic anisotropy on deformation behavior of UFG metal films.

8.2.2 Investigating the Distribution of Local Lattice Strain in the UFG Al Films Using In-situ ACOM-TEM Technique

The different orientations of grains in polycrystalline metal films induce non-uniform stress distributions in them. Several approaches have been introduced to model these stress distributions. Examples include physically-based plasticity models (e.g. Sachs

(Sachs 1928), Taylor (Taylor 1938) or self-consistent models (Molinari, Ahzi, and Kouddane 1997)) where different assumptions are made about the deformation behavior of the grains . To facilitate the understanding of how stress and strain is partitioned between the grains during the deformation of metal films, the distribution of local lattice strain in UFG films needs to be investigated by performing in-situ ACOM-TEM experiments. This will also enable us to verify which model can predict the deformation behavior of the polycrystalline films more accurately.

REFERENCES

Abdolvand, Reza, and Farrokh Ayazi. 2008. "An Advanced Reactive Ion Etching Process for Very High Aspect-Ratio Sub-Micron Wide Trenches in Silicon." *Sensors and Actuators A: Physical* 144 (1): 109–16. doi:10.1016/j.sna.2007.12.026.

Asaro, Robert J. 1983. "Micromechanics of Crystals and Polycrystals." *Advances in Applied Mechanics* 23 (January): 1–115. doi:10.1016/S0065-2156(08)70242-4.

Böhner, Andreas, Verena Maier, Karsten Durst, Heinz Werner Höppel, and Mathias Göken. 2011. "Macro- and Nanomechanical Properties and Strain Rate Sensitivity of Accumulative Roll Bonded and Equal Channel Angular Pressed Ultrafine-Grained Materials." *Advanced Engineering Materials* 13 (4): 251–55. doi:10.1002/adem.201000270.

Borovikov, Valery, Mikhail I. Mendelev, Alexander H. King, and Richard LeSar. 2015. "Effects of Schmid Factor and Slip Nucleation on Deformation Mechanism in Columnar-Grained Nanotwinned Ag and Cu." *Journal of Applied Physics* 117 (8): 085302. doi:10.1063/1.4913381.

Buchheit, Thomas E., Jay D. Carroll, Blythe G. Clark, and Brad L. Boyce. 2015. "Evaluating Deformation-Induced Grain Orientation Change in a Polycrystal During In Situ Tensile Deformation Using EBSD." *Microscopy and Microanalysis* 21 (04): 969–84. doi:10.1017/S1431927615000677.

Chasiotis, I., C. Bateson, K. Timpano, A. S. McCarty, N. S. Barker, and J. R. Stanec. 2007. "Strain Rate Effects on the Mechanical Behavior of Nanocrystalline Au Films." *Thin Solid Films*, TMS 2005 - Mechanical Behaviour of Thin Films and Small Structures, 515 (6): 3183–89. doi:10.1016/j.tsf.2006.01.033.

Chen, C. J., J. C. Huang, H. S. Chou, Y. H. Lai, L. W. Chang, X. H. Du, J. P. Chu, and T. G. Nieh. 2009. "On the Amorphous and Nanocrystalline Zr–Cu and Zr–Ti Co-Sputtered Thin Films." *Journal of Alloys and Compounds*, 14th International Symposium on Metastable and Nano-Materials (ISMANAM-2007), 483 (1–2): 337–40. doi:10.1016/j.jallcom.2008.07.188.

Dalla Torre, F., P. Spätig, R. Schäublin, and M. Victoria. 2005. "Deformation Behaviour and Microstructure of Nanocrystalline Electrodeposited and High Pressure Torsioned Nickel." *Acta Materialia* 53 (8): 2337–49. doi:10.1016/j.actamat.2005.01.041.

Dalla Torre, F., H. Van Swygenhoven, and M. Victoria. 2002. "Nanocrystalline Electrodeposited Ni: Microstructure and Tensile Properties." *Acta Materialia* 50 (15): 3957–70. doi:10.1016/S1359-6454(02)00198-2.

Dao, M., L. Lu, R. J. Asaro, J. T. M. De Hosson, and E. Ma. 2007. "Toward a Quantitative Understanding of Mechanical Behavior of Nanocrystalline Metals." *Acta Materialia* 55 (12): 4041–65. doi:10.1016/j.actamat.2007.01.038.

Darbal, A. D., M. Gemmi, J. Portillo, E. Rauch, and S. Nicolopoulos. 2012. "Nanoscale Automated Phase and Orientation Mapping in the TEM." *Microscopy Today* 20 (06): 38–42. doi:10.1017/S1551929512000818.

Darbal, A.d., K.j. Ganesh, X. Liu, S.-B. Lee, J. Ledonne, T. Sun, B. Yao, et al. 2013. "Grain Boundary Character Distribution of Nanocrystalline Cu Thin Films Using Stereological Analysis of Transmission Electron Microscope Orientation Maps." *Microscopy and Microanalysis* 19 (01): 111–119. doi:10.1017/S1431927612014055.

Dingley, D. 2004. "Progressive Steps in the Development of Electron Backscatter Diffraction and Orientation Imaging Microscopy: EBSD AND OIM." *Journal of Microscopy* 213 (3): 214–24. doi:10.1111/j.0022-2720.2004.01321.x.

Emery, R. D., and G. L. Povirk. 2003a. "Tensile Behavior of Free-Standing Gold Films. Part I. Coarse-Grained Films." *Acta Materialia* 51 (7): 2067–78. doi:10.1016/S1359-6454(03)00006-5.

———. 2003b. "Tensile Behavior of Free-Standing Gold Films. Part II. Fine-Grained Films." *Acta Materialia* 51 (7): 2079–87. doi:10.1016/S1359-6454(03)00007-7.

Faurie, D., P. -O. Renault, E. Le Bourhis, and Ph. Goudeau. 2006. "Study of Texture Effect on Elastic Properties of Au Thin Films by X-Ray Diffraction and in Situ Tensile Testing." *Acta Materialia* 54 (17): 4503–13. doi:10.1016/j.actamat.2006.05.036.

Freund, L. B., and W. D. Nix. 1996. "A Critical Thickness Condition for a Strained Compliant Substrate/Epitaxial Film System." *Applied Physics Letters* 69 (2): 173–75. doi:10.1063/1.117362.

Gianola, D. S., S. Van Petegem, M. Legros, S. Brandstetter, H. Van Swygenhoven, and K. J. Hemker. 2006. "Stress-Assisted Discontinuous Grain Growth and Its Effect on the Deformation Behavior of Nanocrystalline Aluminum Thin Films." *Acta Materialia* 54 (8): 2253–63. doi:10.1016/j.actamat.2006.01.023.

Gianola, D.S., D.H. Warner, J.F. Molinari, and K.J. Hemker. 2006. "Increased Strain Rate Sensitivity due to Stress-Coupled Grain Growth in Nanocrystalline Al." *Scripta Materialia* 55 (7): 649–52. doi:10.1016/j.scriptamat.2006.06.002.

Goh, C. -H., D. L. McDowell, and R. W. Neu. 2006. "Plasticity in Polycrystalline Fretting Fatigue Contacts." *Journal of the Mechanics and Physics of Solids* 54 (2): 340–67. doi:10.1016/j.jmps.2005.06.009.

Hall, E. O. 1951. "The Deformation and Ageing of Mild Steel: III Discussion of Results." *Proceedings of the Physical Society. Section B* 64 (9): 747. doi:10.1088/0370-1301/64/9/303.

Han, Jong H., and M. Taher A. Saif. 2006. "In Situ Microtensile Stage for Electromechanical Characterization of Nanoscale Freestanding Films." *Review of Scientific Instruments* 77 (4): 045102. doi:10.1063/1.2188368.

Haouaoui, M., I. Karaman, and H. J. Maier. 2006. "Flow Stress Anisotropy and Bauschinger Effect in Ultrafine Grained Copper." *Acta Materialia* 54 (20): 5477–88.

Haque, M. A., and M. T. A. Saif. 2002. "In-Situ Tensile Testing of Nano-Scale Specimens in SEM and TEM." *Experimental Mechanics* 42 (1): 123–28. doi:10.1177/0018512002042001797.

Idrissi, Hosni, Aaron Kobler, Behnam Amin-Ahmadi, Michael Coulombier, Montserrat Galceran, Jean-Pierre Raskin, Stéphane Godet, Christian Kübel, Thomas Pardoen, and Dominique Schryvers. 2014. "Plasticity Mechanisms in Ultrafine Grained Freestanding Aluminum Thin Films Revealed by in-Situ Transmission Electron

Microscopy Nanomechanical Testing." *Applied Physics Letters* 104 (10): 101903. doi:10.1063/1.4868124.

Izadi, Ehsan, Amith Darbal, Pedro Peralta, and Jagannathan Rajagopalan. 2016. "In Situ TEM Straining of Ultrafine-Grained Aluminum Films of Different Textures Using Automated Crystal Orientation Mapping." *Microscopy and Microanalysis* 22 (S3): 1950–51. doi:10.1017/S143192761601059X.

Izadi, Ehsan, Amith Darbal, Rohit Sarkar, and Jagannathan Rajagopalan. 2017. "Grain Rotations in Ultrafine-Grained Aluminum Films Studied Using in Situ TEM Straining with Automated Crystal Orientation Mapping." *Materials & Design* 113 (January): 186–94. doi:10.1016/j.matdes.2016.10.015.

Izadi, Ehsan, Saul Opie, Harn Lim, Pedro Peralta, and Jagannathan Rajagopalan. 2017. "Effect of Plastic Anisotropy on the Deformation Behavior of Bicrystalline Aluminum Films – Experiments and Modeling." (Under Review)

Izadi, Ehsan, and Jagannathan Rajagopalan. 2016. "Texture Dependent Strain Rate Sensitivity of Ultrafine-Grained Aluminum Films." *Scripta Materialia* 114 (March): 65–69. doi:10.1016/j.scriptamat.2015.12.003.

Jiang, Zhonghao, Xianli Liu, Guangyu Li, Qing Jiang, and Jianshe Lian. 2006. "Strain Rate Sensitivity of a Nanocrystalline Cu Synthesized by Electric Brush Plating." *Applied Physics Letters* 88 (14): 143115. doi:10.1063/1.2193467.

Jin, M., A. M. Minor, E. A. Stach, and J. W. Morris. 2004. "Direct Observation of Deformation-Induced Grain Growth during the Nanoindentation of Ultrafine-Grained Al at Room Temperature." *Acta Materialia* 52 (18): 5381–87. doi:10.1016/j.actamat.2004.07.044.

Jonnalagadda, K., N. Karanjgaokar, I. Chasiotis, J. Chee, and D. Peroulis. 2010. "Strain Rate Sensitivity of Nanocrystalline Au Films at Room Temperature." *Acta Materialia* 58 (14): 4674–84. doi:10.1016/j.actamat.2010.04.048.

Karanjgaokar, N. J., C. -S. Oh, J. Lambros, and I. Chasiotis. 2012. "Inelastic Deformation of Nanocrystalline Au Thin Films as a Function of Temperature and Strain Rate." *Acta Materialia* 60 (13–14): 5352–61. doi:10.1016/j.actamat.2012.06.018.

Kim, Hyoung Seop, and Yuri Estrin. 2005. "Phase Mixture Modeling of the Strain Rate Dependent Mechanical Behavior of Nanostructured Materials." *Acta Materialia* 53 (3): 765–72. doi:10.1016/j.actamat.2004.10.028.

Kobler, A., A. Kashiwar, H. Hahn, and C. Kübel. 2013. "Combination of in Situ Straining and ACOM TEM: A Novel Method for Analysis of Plastic Deformation of Nanocrystalline Metals." *Ultramicroscopy* 128 (May): 68–81. doi:10.1016/j.ultramic.2012.12.019.

Koch, CC. 2003. "Top-Down Synthesis Of Nanostructured Materials: Mechanical And Thermal Processing Methods." *Reviews on Advanced Materials Science* 5: 91–99.

Kocks, U. F. 1970. "The Relation between Polycrystal Deformation and Single-Crystal Deformation." *Metallurgical and Materials Transactions* 1 (5): 1121–43. doi:10.1007/BF02900224.

Kumar, K. S., S. Suresh, M. F. Chisholm, J. A. Horton, and P. Wang. 2003. "Deformation of Electrodeposited Nanocrystalline Nickel." *Acta Materialia* 51 (2): 387–405. doi:10.1016/S1359-6454(02)00421-4.

Kumar, K. S, H Van Swygenhoven, and S Suresh. 2003. "Mechanical Behavior of Nanocrystalline Metals and alloys11The Golden Jubilee Issue—Selected Topics in Materials Science and Engineering: Past, Present and Future, Edited by S. Suresh." *Acta Materialia*, The Golden Jubilee Issue. Selected topics in Materials Science and Engineering: Past, Present and Future, 51 (19): 5743–74. doi:10.1016/j.actamat.2003.08.032.

Ledermann, Nicolas, Paul Muralt, Jacek Baborowski, Sandrine Gentil, Kapil Mukati, Marco Cantoni, Andreas Seifert, and Nava Setter. 2003. "{1 0 0}-Textured, Piezoelectric Pb(Zrx, Ti1−x)O3 Thin Films for MEMS: Integration, Deposition and Properties." *Sensors and Actuators A: Physical* 105 (2): 162–70. doi:10.1016/S0924-4247(03)00090-6.

Leff, A. C., and M. L. Taheri. 2016. "Quantitative Assessment of the Driving Force for Twin Formation Utilizing Nye Tensor Dislocation Density Mapping." *Scripta Materialia* 121 (August): 14–17. doi:10.1016/j.scriptamat.2016.04.035.

Leff, A. C., C. R. Weinberger, and M. L. Taheri. 2015. "Estimation of Dislocation Density from Precession Electron Diffraction Data Using the Nye Tensor." *Ultramicroscopy* 153 (June): 9–21. doi:10.1016/j.ultramic.2015.02.002.

Li, Lin, Myoung-Gyu Lee, and Peter M. Anderson. 2010. "Critical Strengths for Slip Events in Nanocrystalline Metals: Predictions of Quantized Crystal Plasticity Simulations." *Metallurgical and Materials Transactions A* 42 (13): 3875–82. doi:10.1007/s11661-010-0392-2.

Li, Lin, Steven Van Petegem, Helena Van Swygenhoven, and Peter M. Anderson. 2012. "Slip-Induced Intergranular Stress Redistribution in Nanocrystalline Ni." *Acta Materialia* 60 (20): 7001–10. doi:10.1016/j.actamat.2012.09.007.

Lin Li, Peter M. Anderson. 2009. "The Stress–strain Response of Nanocrystalline Metals: A Quantized Crystal Plasticity Approach." *Acta Materialia* 57 (3): 812–22. doi:10.1016/j.actamat.2008.10.035.

Maier, Verena, Karsten Durst, Johannes Mueller, Björn Backes, Heinz Werner Höppel, and Mathias Göken. 2011. "Nanoindentation Strain-Rate Jump Tests for Determining the Local Strain-Rate Sensitivity in Nanocrystalline Ni and Ultrafine-Grained Al." *Journal of Materials Research* 26 (11): 1421–30. doi:10.1557/jmr.2011.156.

Marin, Esteban B. 2006. "On the Formulation of a Crystal Plasticity Model." SAND2006-4170. Sandia National Laboratories. https://www.osti.gov/scitech/biblio/890604.

Masumura, R. A., P. M. Hazzledine, and C. S. Pande. 1998. "Yield Stress of Fine Grained Materials." *Acta Materialia* 46 (13): 4527–34. doi:10.1016/S1359-6454(98)00150-5.

May, J., H. W. Höppel, and M. Göken. 2005. "Strain Rate Sensitivity of Ultrafine-Grained Aluminium Processed by Severe Plastic Deformation." *Scripta Materialia* 53 (2): 189–94. doi:10.1016/j.scriptamat.2005.03.043.

Meyers, M.A., A. Mishra, and D.J. Benson. 2006. "Mechanical Properties of Nanocrystalline Materials." *Progress in Materials Science* 51 (4): 427–556. doi:10.1016/j.pmatsci.2005.08.003.

Mishnaevsky, Leon, and Evgeny Levashov. 2015. "Micromechanical Modelling of Nanocrystalline and Ultrafine Grained Metals: A Short Overview." *Computational Materials Science* 96: 365–73. doi:10.1016/j.commatsci.2014.09.024.

Mohanty, Gaurav, Jeffrey M. Wheeler, Rejin Raghavan, Juri Wehrs, Madoka Hasegawa, Stefano Mischler, Laetitia Philippe, and Johann Michler. 2014. "Elevated Temperature, Strain Rate Jump Microcompression of Nanocrystalline Nickel." *Philosophical Magazine* 0 (0): 1–18. doi:10.1080/14786435.2014.951709.

Mohebbi, Mohammad Sadegh, Abbas Akbarzadeh, Bong Hwan Kim, and Shae-Kwang Kim. 2014. "Analysis of Strain Rate Sensitivity of Ultrafine-Grained AA1050 by Stress Relaxation Test." *Metallurgical and Materials Transactions A* 45 (12): 5442–50. doi:10.1007/s11661-014-2534-4.

Molinari, A., S. Ahzi, and R. Kouddane. 1997. "On the Self-Consistent Modeling of Elastic-Plastic Behavior of Polycrystals." *Mechanics of Materials* 26 (1): 43–62. doi:10.1016/S0167-6636(97)00017-3.

Mompiou, F., and M. Legros. 2015. "Quantitative Grain Growth and Rotation Probed by in-Situ TEM Straining and Orientation Mapping in Small Grained Al Thin Films." *Scripta Materialia* 99 (April): 5–8. doi:10.1016/j.scriptamat.2014.11.004.

Mompiou, F., M. Legros, A. Boé, M. Coulombier, J. -P. Raskin, and T. Pardoen. 2013. "Inter- and Intragranular Plasticity Mechanisms in Ultrafine-Grained Al Thin Films: An in Situ TEM Study." *Acta Materialia* 61 (1): 205–16. doi:10.1016/j.actamat.2012.09.051.

Mompiou, Frédéric, Daniel Caillard, Marc Legros, and Haël Mughrabi. 2012. "In Situ TEM Observations of Reverse Dislocation Motion upon Unloading in Tensile-Deformed UFG Aluminium." *Acta Materialia* 60 (8): 3402–14. doi:10.1016/j.actamat.2012.02.049.

Niwa, H., and Masaharu Kato. 1991. "Epitaxial Growth of Al on Si(001) by Sputtering." *Applied Physics Letters* 59 (5): 543–45. doi:10.1063/1.105433.

Nix, William D. 1998. "YIELDING AND STRAIN HARDENING OF THIN METAL FILMS ON SUBSTRATES." *Scripta Materialia* 39.4 (4): 545–554.

Petch, N. J. 1953. "The Cleavage Strength of Polycrystals." *Journal of the Iron and Steel Institute* 174: 25–28.

Polcawich, Ronald G., Jeffrey S. Pulskamp, Daniel Judy, Prashant Ranade, Susan Trolier-McKinstry, and Madan Dubey. 2007. "Surface Micromachined Microelectromechancial Ohmic Series Switch Using Thin-Film Piezoelectric Actuators." *IEEE Transactions on Microwave Theory and Techniques* 55 (12): 2642–54. doi:10.1109/TMTT.2007.910072.

Portillo, Joaquim, Edgar F. Rauch, Stavros Nicolopoulos, Mauro Gemmi, and Daniel Bultreys. 2010. "Precession Electron Diffraction Assisted Orientation Mapping in the Transmission Electron Microscope." *Materials Science Forum* 644: 1–7. doi:10.4028/www.scientific.net/MSF.644.1.

Rajabzadeh, A., F. Mompiou, M. Legros, and N. Combe. 2013. "Elementary Mechanisms of Shear-Coupled Grain Boundary Migration." *Physical Review Letters* 110 (26): 265507. doi:10.1103/PhysRevLett.110.265507.

Rajagopalan, Jagannathan, Jong H. Han, and M. Taher A. Saif. 2008. "Bauschinger Effect in Unpassivated Freestanding Nanoscale Metal Films." *Scripta Materialia* 59 (7): 734–37. doi:10.1016/j.scriptamat.2008.06.010.

Rajagopalan, Jagannathan, Christian Rentenberger, H. Peter Karnthaler, Gerhard Dehm, and M. Taher A. Saif. 2010. "In Situ TEM Study of Microplasticity and Bauschinger Effect in Nanocrystalline Metals." *Acta Materialia* 58 (14): 4772–82. doi:10.1016/j.actamat.2010.05.013.

Rajagopalan, Jagannathan, Christian Rentenberger, H. Peter Karnthaler, Gerhard Dehm, and M. Taher A. Saif. 2010. "In Situ TEM Study of Microplasticity and Bauschinger Effect in Nanocrystalline Metals." *Acta Materialia* 58 (14): 4772–82. doi:10.1016/j.actamat.2010.05.013.

Rajagopalan, Jagannathan, and M. Taher A. Saif. 2011. "Effect of Microstructural Heterogeneity on the Mechanical Behavior of Nanocrystalline Metal Films." *Journal of Materials Research* 26 (22): 2826–32. doi:10.1557/jmr.2011.316.

Rauch, E. F., and M. Véron. 2014. "Automated Crystal Orientation and Phase Mapping in TEM." *Materials Characterization* 98 (December): 1–9. doi:10.1016/j.matchar.2014.08.010.

Rauch, Edgar, Joaquin Portillo, Stavros Nicolopoulos, Daniel Bultreys, Sergei Rouvimov, and Peter Moeck. 2010. "Automated Nanocrystal Orientation and Phase Mapping in the Transmission Electron Microscope on the Basis of Precession Electron Diffraction." *Zeitschrift Für Kristallographie - Crystalline Materials*, March. doi:10.1524/zkri.2010.1205.

Read, David T, Yi-Wen Cheng, Robert R Keller, and J. David McColskey. 2001. "Tensile Properties of Free-Standing Aluminum Thin Films." *Scripta Materialia* 45 (5): 583–89. doi:10.1016/S1359-6462(01)01067-3.

Rupert, T. J., D. S. Gianola, Y. Gan, and K. J. Hemker. 2009. "Experimental Observations of Stress-Driven Grain Boundary Migration." *Science* 326 (5960): 1686–90. doi:10.1126/science.1178226.

Sachs, G. 1928. "Plasticity Problems in Metals." *Transactions of the Faraday Society* 24 (0): 84–92. doi:10.1039/TF9282400084.

Sanders, P. G., J. A. Eastman, and J. R. Weertman. 1997. "Elastic and Tensile Behavior of Nanocrystalline Copper and Palladium." *Acta Materialia* 45 (10): 4019–25. doi:10.1016/S1359-6454(97)00092-X.

Sarkar, Rohit, Christian Rentenberger, and Jagannathan Rajagopalan. 2015. "Electron Beam Induced Artifacts During in Situ TEM Deformation of Nanostructured Metals." *Scientific Reports* 5 (November): 16345. doi:10.1038/srep16345.

Schwaiger, R, B Moser, M Dao, N Chollacoop, and S Suresh. 2003. "Some Critical Experiments on the Strain-Rate Sensitivity of Nanocrystalline Nickel." *Acta Materialia* 51 (17): 5159–72. doi:10.1016/S1359-6454(03)00365-3.

Simmons, Gene, and Herbert Wang. 1971. *Single Crystal Elastic Constants and Calculated Aggregate Properties: A Handbook*. M.I.T. Press.

Stéphane, L., and B. Stéphane. 2011. "Une Toolbox Abaqus Pour Le Calcul de Propriétés Effectives de Milieux Hétérogènes." In *Une Toolbox Abaqus Pour Le Calcul de Propriétés Effectives de Milieux Hétérogènes*. Giens, France. https://hal.archives-ouvertes.fr/hal-00592866/document.

Taylor, Sir Geoffrey Ingram. 1938. *Plastic Strain in Metals*.

Thomas, J. F. 1968. "Third-Order Elastic Constants of Aluminum." *Physical Review* 175 (3): 955–62. doi:10.1103/PhysRev.175.955.

Valiev, Ruslan Z., Yuri Estrin, Zenji Horita, Terence G. Langdon, Michael J. Zechetbauer, and Yuntian T. Zhu. 2006. "Producing Bulk Ultrafine-Grained Materials by Severe Plastic Deformation." *JOM* 58 (4): 33–39. doi:10.1007/s11837-006-0213-7.

Van Swygenhoven, H., P.M. Derlet, and A.G. Frøseth. 2006. "Nucleation and Propagation of Dislocations in Nanocrystalline Fcc Metals." *Acta Materialia* 54 (7): 1975–83. doi:10.1016/j.actamat.2005.12.026.

Van Swygenhoven, H., D. Farkas, and A. Caro. 2000. "Grain-Boundary Structures in Polycrystalline Metals at the Nanoscale." *Physical Review B* 62 (2): 831–38. doi:10.1103/PhysRevB.62.831.

Van Swygenhoven, Helena, and Steven Van Petegem. 2013. "In-Situ Mechanical Testing during X-Ray Diffraction." *Materials Characterization* 78 (April): 47–59. doi:10.1016/j.matchar.2012.12.010.

Wang, Y. M., A. V. Hamza, and E. Ma. 2005. "Activation Volume and Density of Mobile Dislocations in Plastically Deforming Nanocrystalline Ni." *Applied Physics Letters* 86 (24): 241917. doi:10.1063/1.1946899.

———. 2006. "Temperature-Dependent Strain Rate Sensitivity and Activation Volume of Nanocrystalline Ni." *Acta Materialia* 54 (10): 2715–26. doi:10.1016/j.actamat.2006.02.013.

Wang, Y. M., and E. Ma. 2004a. "Strain Hardening, Strain Rate Sensitivity, and Ductility of Nanostructured Metals." *Materials Science and Engineering: A* 375–377 (July): 46–52. doi:10.1016/j.msea.2003.10.214.

Wang, Y.M., and E. Ma. 2004b. "Strain Hardening, Strain Rate Sensitivity, and Ductility of Nanostructured Metals." *Materials Science and Engineering: A* 375–377 (July): 46–52. doi:10.1016/j.msea.2003.10.214.

Wheeler, J. M., V. Maier, K. Durst, M. Göken, and J. Michler. 2013. "Activation Parameters for Deformation of Ultrafine-Grained Aluminium as Determined by Indentation Strain Rate Jumps at Elevated Temperature." *Materials Science and Engineering: A* 585 (November): 108–13. doi:10.1016/j.msea.2013.07.033.

Zaefferer, S. 2011. "A Critical Review of Orientation Microscopy in SEM and TEM." *Crystal Research and Technology* 46 (6): 607–28. doi:10.1002/crat.201100125.

Zhou, Caizhi, and Richard LeSar. 2012. "Dislocation Dynamics Simulations of Plasticity in Polycrystalline Thin Films." *International Journal of Plasticity* 30–31 (March): 185–201. doi:10.1016/j.ijplas.2011.10.001.

Zhu, X., R. Birringer, U. Herr, and H. Gleiter. 1987. "X-Ray Diffraction Studies of the Structure of Nanometer-Sized Crystalline Materials." *Physical Review B* 35 (17): 9085–90. doi:10.1103/PhysRevB.35.9085.